NATIONAL AND KAPODISTRIAN UNIVERSITY OF ATHENS

SCHOOL OF SCIENCE
DEPARTMENT OF INFORMATICS AND TELECOMMUNICATIONS

MASTER'S PROGRAM IN
MICROELECTRONICS

MASTER'S THESIS

Simulation of atmospheric pressure plasma jets with a global model

Dimitrios N. Passaras

Supervisor : **George Kokkoris,** Research Fellow, NCSR "Demokritos"

ATHENS

OCTOBER 2016

ΕΘΝΙΚΟ ΚΑΙ ΚΑΠΟΔΙΣΤΡΙΑΚΟ ΠΑΝΕΠΙΣΤΗΜΙΟ ΑΘΗΝΩΝ

ΣΧΟΛΗ ΘΕΤΙΚΩΝ ΕΠΙΣΤΗΜΩΝ
ΤΜΗΜΑ ΠΛΗΡΟΦΟΡΙΚΗΣ ΚΑΙ ΤΗΛΕΠΙΚΟΙΝΩΝΙΩΝ

ΔΙΑΤΜΗΜΑΤΙΚΟ ΠΡΟΓΡΑΜΜΑ ΜΕΤΑΠΤΥΧΙΑΚΩΝ ΣΠΟΥΔΩΝ ΣΤΗ ΜΙΚΡΟΗΛΕΚΤΡΟΝΙΚΗ

ΔΙΠΛΩΜΑΤΙΚΗ ΕΡΓΑΣΙΑ

Προσομοίωση πλάσματος τύπου τζετ σε ατμοσφαιρική πίεση με μοντέλο μηδενικής διάστασης

Δημήτριος Ν. Πασσαράς

Επιβλέπων : **Γεώργιος Κόκκορης,** Συνεργαζόμενος ερευνητής, ΕΚΕΦΕ «Δημόκριτος»

ΑΘΗΝΑ

ΟΚΤΩΒΡΙΟΣ 2016

MASTER'S THESIS

Simulation of atmospheric pressure plasma jets with a global model

Dimitrios N. Passaras

A.M.: MM234

SUPERVISOR : **George Kokkoris ,** Research Fellow, NCSR "Demokritos"

EXAMINING COMMITTEE :

- **Angeliki Arapoyanni,** Professor, Department of Informatics and Telecommunications, N.K.U.A
- **Evangelos Gogolides,** Director of Research, N.C.S.R. "Demokritos"
- **Angeliki Tserepi,** Director of Research, N.C.S.R. "Demokritos"
- **Eleftherios Amanatides,** Assistant Professor, Department of Chemical Engineering, University of Patras
- **George Kokkoris,** Research fellow, N.C.S.R. "Demokritos"

October 2016

ΔΙΠΛΩΜΑΤΙΚΗ ΕΡΓΑΣΙΑ

Προσομοίωση πλάσματος τύπου τζετ σε ατμοσφαιρική πίεση με μοντέλο μηδενικής διάστασης

Δημήτριος Ν. Πασσαράς

Α.Μ.: ΜΜ234

ΕΠΙΒΛΕΠΩΝ : **Γεώργιος Κόκκορης,** Συνεργαζόμενος ερευνητής, ΕΚΕΦΕ «Δημόκριτος»

ΕΞΕΤΑΣΤΙΚΗ ΕΠΙΤΡΟΠΗ :

- **Αγγελική Αραπογιάννη,** Καθηγήτρια, Τμήμα Πληροφορικής και Τηλεπικοινωνιών, ΕΚΠΑ
- **Ευάγγελος Γογγολίδης,** Διευθυντής Ερευνών, ΕΚΕΦΕ "Δημόκριτος"
- **Αγγελική Τσερέπη,** Διευθύντρια Ερευνών, ΕΚΕΦΕ "Δημόκριτος'
- **Ελευθέριος Αμανατίδης,** Επίκουρος Καθηγητής, Τμήμα Χημικών Μηχανικών, Πανεπιστήμιο Πατρών
- **Γεώργιος Κόκκορης,** Συνεργαζόμενος Ερευνητής, ΕΚΕΦΕ "Δημόκριτος"

Οκτώβριος 2016

ABSTRACT

Cold atmospheric pressure plasma jets (APPJs) have a huge potential in a wide range of applications including surface activation and modification, deposition of thin films, as well as agriculture and biomedical applications, such as food decontamination, wound healing, and cancer treatment. Modeling and simulation of APPJs can contribute to a better understanding of the operation of pertinent devices and the design of new, more advanced ones. Multidimensional, detailed, models are widely used for plasma simulations and usually their solution entails a high computational cost (in time and memory). The number of unknown variables, and as a consequence the computational cost, further increases when the number of species being taken into account increases. This is the case with APPJ devices, which are not enclosed: A large number of species has to be taken into account in the reaction set due to the presence of air, containing O_2, N_2, and H_2O, in the gas mixture.

In this thesis, instead of using detailed models with a high computational cost, a global model is proposed for the simulation of APPJs; a global model is essentially a zero dimensional model, i.e., no spatial variations of variables can be resolved. Instead, spatially, volume, averaged quantities are used. In particular, a homemade code for global modeling in low pressure plasma reactors, namely πlasma-R, is extended to handle cases of APPJs. The model is formulated and solved at transient state; a fast solver is utilized. By transforming the transient solution to a spatial solution (1d) through the flow velocity, the extended model can calculate the active species densities and electron temperature along the distance from the device exit in a very short amount of time (several seconds).The model is not self-consistent: It requires several experimental measurements such as the flow velocity along the distance from the device exit.

The results of the extended model are verified by a comparison with a seminal simulation work for Ar APPJs from the literature; the reaction set consists of 846 reactions and the total number of species is 84.

Critical for the calculations of the extended model is the electron energy distribution function (EEDF) which is either considered as Maxwellian or is calculated by a Boltzmann equation solver, namely Bolsig+. The solver calculates the EEDF but only for a limited number of conditions; to minimize the use of the Boltzmann equation solver (which is external to the extended global model), the EEDF is considered constant in spatial spaces along the jet. It is found that the use of Maxwellian EEDF instead of the EEDF coming from the Boltzmann solver yields a significantly different electron temperature; however, the differences for the calculated species densities along the jet are less pronounced.

Finally, in an attempt to develop a self-consistent model for APPJs and eliminate the need for inputs from experimental measurements, two dimensional fluid simulations of the jet, decoupled from the plasma simulation, are made. The flow field and the species (Ar, N_2, O_2 and H_2O) densities are calculated with various turbulent models; the results show that there are slight discrepancies among the model results, mainly near the nozzle exit.

SUBJECTAREA: simulation of atmospheric pressure plasma jet

KEYWORDS: plasma jet, global model, atmospheric pressure plasma, turbulent flow, stiff differential equations

ΠΕΡΙΛΗΨΗ

Το ψυχρό Πλάσμα Τύπου Τζετ σε Ατμοσφαιρική Πίεση (ΠΤΤΑΠ) παρουσιάζει μεγάλη δυναμική σε ένα μεγάλο εύρος εφαρμογών, όπως η ενεργοποίηση και τροποποίηση επιφανειών, η απόθεση υμενίων, η απολύμανση τροφίμων, η επούλωση πληγών και η αντικαρκινική θεραπεία. Η προσομοίωση του ΠΤΤΑΠ μπορεί να συνεισφέρει στην καλύτερη κατανόηση της λειτουργίας των συσκευών που το παράγουν και στο σχεδιασμό νέων. Λεπτομερή μοντέλα πολλαπλών διαστάσεων έχουν χρησιμοποιηθεί ευρέως για προσομοιώσεις πλάσματος. Συνήθως συνοδεύονται από υψηλό υπολογιστικό κόστος (σε χρόνο και μνήμη). Το κόστος αυτό αυξάνεται στην περίπτωση ατμοσφαιρικού πλάσματος εξαιτίας της παρουσίας αέρα στο μίγμα αερίων: Το πλήθος των χημικών συστατικών και άρα το πλήθος των αγνώστων αυξάνεται εξαιτίας της διάσπασης των συστατικών του ατμοσφαιρικού αέρα [Ar, N_2, O_2, H_2O (υδρατμοί)] και των αντιδράσεων μεταξύ των διασπασμένων συστατικών.

Στα πλαίσια της παρούσας εργασίας, γίνεται χρήση μοντέλου μηδενικής διάστασης (0δ, global model), το οποίο μειώνει σημαντικά το υπολογιστικό κόστος των λεπτομερών μοντέλων, για την προσομοίωση ΠΤΤΑΠ. Συγκεκριμένα, κώδικας για την προσομοίωση πλάσματος σε αντιδραστήρες χαμηλής πίεσης με μοντέλο 0δ (πlasma-R) διευρύνεται ώστε να μπορεί να διαχειρίζεται και περιπτώσεις ΠΤΤΑΠ. Το διευρυμένο μοντέλο διατυπώνεται και επιλύεται σε μεταβατική κατάσταση με χρήση αποδοτικού επιλύτη. Μπορεί να δώσει αποτελέσματα σε πολύ μικρό χρόνο (μερικά δευτερόλεπτα) για τις συγκεντρώσεις των χημικών συστατικών και τη θερμοκρασία των ηλεκτρονίων κατά μήκος της απόστασης από την έξοδο της συσκευής. Αυτό είναι εφικτό για ένα μοντέλο 0δ με μετατροπή της χρονοεξαρτώμενης λύσης σε χωρική, 1δ, λύση μέσω της ταχύτητας ροής. Το διευρυμένο μοντέλο δεν είναι αυτόνομο (self-consistent), αφού για την επίλυσή του χρειάζονται πειραματικές μετρήσεις, όπως η ταχύτητα ροής του τζετ.

Τα αποτελέσματα του διευρυμένου μοντέλου επαληθεύονται μέσω της σύγκρισής τους με αυτά εργασίας όπου γίνεται προσομοίωση πλάσματος (Αργού) τύπου τζετ σε ατμοσφαιρική πίεση. Το συνολικό πλήθος των χημικών συστατικών είναι 84 και το πλήθος των αντιδράσεων 846. Μια πολύ σημαντική παράμετρος για τους υπολογισμούς του διευρυμένου μοντέλου είναι η κατανομή ενέργειας των ηλεκτρονίων (ΚΕΗ), η οποία είτε θεωρείται Maxwell είτε υπολογίζεται από επιλύτη της εξίσωσης Boltzmann (Bolsig+). Ο επιλύτης υπολογίζει την ΚΕΗ αλλά μόνο για έναν ορισμένο αριθμό διαφορετικών συνθηκών: Για να μειωθεί η χρήση του επιλύτη, ο οποίος είναι εξωτερικός του διευρυμένου μοντέλου, η ΚΕΗ θεωρείται σταθερή σε χωρικά διαστήματα κατά μήκος του τζετ. Τα αποτελέσματα δείχνουν ότι ενώ η θεώρηση ΚΕΗ Maxwell οδηγεί σε θερμοκρασία ηλεκτρονίων που διαφέρει σημαντικά από τη θερμοκρασία που υπολογίζεται όταν η ΚΕΗ προέρχεται από την επίλυση της εξίσωσης Boltzmann, οι διαφορές στις συγκεντρώσεις των συστατικών κατά μήκος του τζετ δεν είναι το ίδιο σημαντικές.

Τέλος, σε μια προσπάθεια να αναπτυχθεί αυτόνομο μοντέλο για ΠΤΤΑΠ, το οποίο δεν θα χρειάζεται πειραματικές μετρήσεις για την επίλυσή του, γίνονται 2δ προσομοιώσεις της ροής αποσυζευγμένες από το πλάσμα. Το πεδίο ροής και οι συγκεντρώσεις των Ar, N_2, O_2 και H_2O υπολογίζονται με διαφορετικά μοντέλα τυρβώδους ροής και τα αποτελέσματα δείχνουν μικρές αποκλίσεις μεταξύ των μοντέλων, κυρίως κοντά στην έξοδο της διάταξης.

ΘΕΜΑΤΙΚΗ ΠΕΡΙΟΧΗ: Προσομοίωση πλάσματος τύπου τζετ

ΛΕΞΕΙΣ ΚΛΕΙΔΙΑ: πλάσμα τύπου τζετ, μοντέλο μηδενικής διάστασης,πλάσμα ατμοσφαιρικής πίεσης, τυρβώδης ροή, δύσκαμπτες (stiff) διαφορικές εξισώσεις

CONTENTS

INDEX OF FIGURES

INDEX OF TABLES

PROLOGUE

This Thesis was held at the Institute of Nanoscience and Nanotechnology of the National Center for Scientific Research “Demokritos” as part of the joint Master’s program in “Microelectronics” of the National and Kapodistrian University of Athens with the NCSR “Demokritos”. I would like to thank my supervisor, Dr. George Kokkoris, for his continuous guidance and support, during this work. I would also like to thank Mr. Kontosis for his really valuable IT advice and his support with the code πlasma-R.

1. INTRODUCTION

1.1 What is plasma?

Plasmas are often called a fourth state of matter (Figure 1.1). A solid substance in thermal equilibrium generally passes into a liquid state as the temperature is increased at a fixed pressure. The liquid passes into a gas as the temperature is further increased. At a sufficiently high temperature, the molecules in the gas decompose to form a gas of atoms that move freely in random directions, except for infrequent collisions between atoms. If the temperature is further increased then the atoms decompose into freely moving charged particles (electrons and positive ions), and the substance enters the plasma state. Besides heating, the application of electromagnetic fields can produce plasmas; the latter is the origin of plasmas used for technological applications.

A plasma is a collection of free charged particles moving in random directions that is, on the average, electrically neutral (Figure 1.2a). The fractional ionization of a plasma is $x_{iz} = n_i/(n_i + n_g)$ where n_g is the neutral gas density and n_i is the ions density. x_{iz} is near unity for fully ionized plasmas, and $x_{iz} \ll 1$ for weakly ionized plasmas [1].

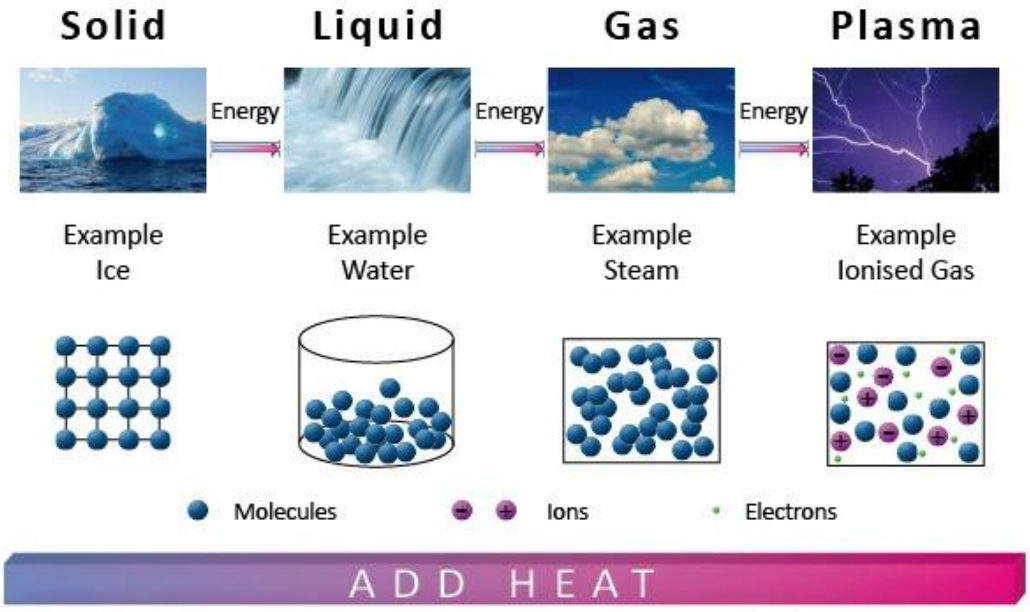

Figure 1.1: The four states of matter [2].

1.2 Types of plasmas

Much of the matter in the universe is in the plasma state. This is true because stars, as well as most interstellar matter, are plasmas. Although stars are plasmas in thermal equilibrium ($T_{electron} = T_{ion} = T_{gas}$), the light and heavy charged particles in many laboratory discharges are almost never in thermal equilibrium (non-equilibrium plasmas), either between themselves or with their surroundings. Because these discharges are electrically driven and are weakly ionized, the applied power preferentially heats the mobile electrons, while the heavy ions efficiently exchange energy by collisions with the background gas. Hence, $T_{electron} = T_e \gg T_{ion}$ for these plasmas [1].

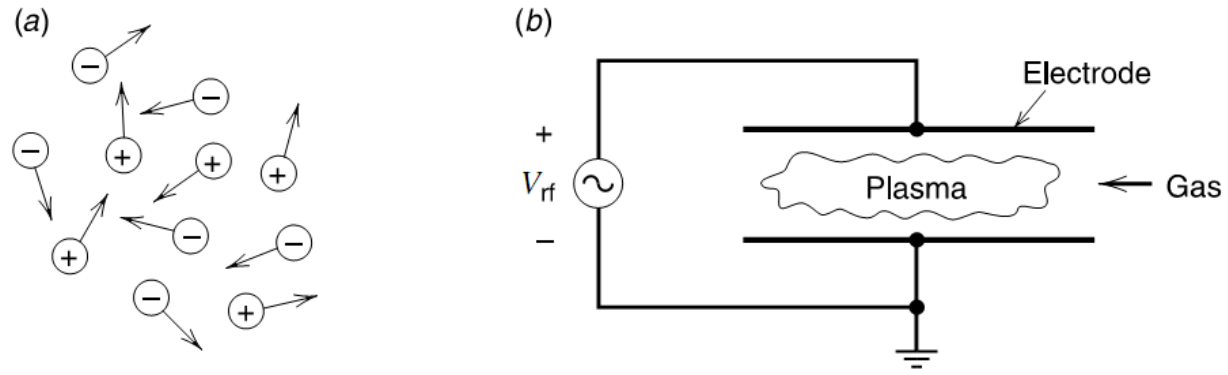

Figure 1.2: Schematic view of (a) a plasma and (b) an electrically driven discharge [1].

A simple discharge is shown schematically in Figure 1.2b. It consists of a voltage source that drives current through a low-pressure gas between two parallel conducting plates or electrodes. The gas “breaks down” to form a plasma, usually weakly ionized, that is, the plasma density (electron density) is only a small fraction of the neutral gas density.

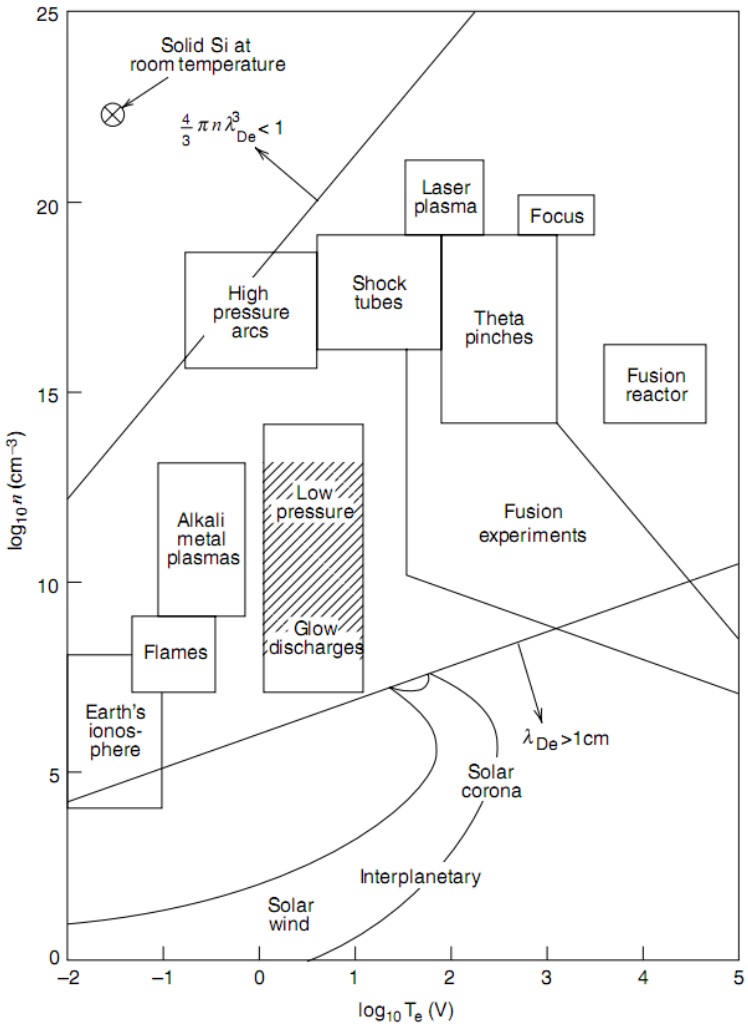

Figure 1.3: Space and laboratory plasmas [1].

Figure 1.3 identifies different kind of plasmas on a $\log(n)$ [$\log(n_e)$] versus $\log(T_e)$ diagram. There is an enormous range of densities and temperatures for both laboratory

and space plasmas. One important type of processing discharges is the low pressure type of discharges. Low pressure discharges are characterized by $T_e \approx 1-10$ eV, $T_{ion} \ll T_e$ and plasma (electron) densities, $n_e \approx 10^8 - 10^{13}$ cm^{-3}. These discharges are used as miniature chemical factories in which feedstock gases are broken into positive ions and chemically reactive etchants, deposition precursors and so on, which then flow to and physically or chemically react at the substrate surface. While energy is delivered to the substrate also, for example, in the form of bombarding ions, the energy flux is there to promote the chemistry at the substrate, and not to heat the substrate. The gas pressures for these discharges are low: $p \approx 10^{-3} - 1$Torr. High pressure arc discharges are also used for processing. These discharges have $T_e \approx 0.1 - 2$ eV and $n_e \approx 10^{14} - 10^{19}$ cm^{-3}, and the light and heavy particles are more nearly in thermal equilibrium, with $T_{ion} \leq T_e$. These discharges are used mainly to deliver heat to the substrate, for example, to increase surface reaction rates, to melt, sinter, or evaporate materials, or to weld or cut refractory materials. Operating pressures are typically near atmospheric pressure (760 Torr) [1]. Another very important type of high pressure discharges is the cold atmospheric pressure plasma jets described in the following section.

1.3 Cold atmospheric pressure plasma jets

Atmospheric pressure plasma jets (APPJs) have T_{ion} and T_{gas} in the range of 300-1000 K, which is at least one order of magnitude lower than T_e. APPJs operating in open air at moderate gas temperatures (cold plasma jets) but nevertheless with high plasma-chemical activity triggered a multiplicity of interesting applications. The capability of producing charged particles, neutral metastable species, radicals and (V)UV (vacuum ultraviolet) radiation at biologically tolerable gas temperatures, let those sources become important for biomedical applications, like the inactivation of bacteria on heat sensitive surfaces, wound healing or cancer treatment [3]. But also in the field of surface activation and modification, agriculture as well as deposition of thin films, cold APPJs have a huge potential [3].

Due to the high collision frequency between electrons and heavy particles (neutral species and ions) at atmospheric pressure conditions, the electrons lose their energy in a short period. If a molecular gas is present, the electrons could quickly transfer their energy to molecular rotational and vibrational states because the energy levels of the rotational and vibrational states of the molecules can be much lower than that of the electrons' excitation and ionization. This makes it a difficult task to obtain atmospheric-pressure non-equilibrium plasmas with high electron energy [4]. Thus, the ionization efficiency in such a case is low. Furthermore, when an electronegative gas, such as O_2 and SF_6, is present, the electrons could be absorbed by the gas on a time scale of tens of nanoseconds, or even shorter, which makes it even harder to obtain atmospheric pressure non-equilibrium plasmas with electronegative gases. Nevertheless, for traditional discharges, a plasma is generated as long as the applied electric field across the discharge gap is high enough to initiate a breakdown. However, at a pressure of 1 atm, the electric field required to initiate the discharge is quite high. For example, when air is used, the required electric field is about 30 kVcm^{-1} [4]. That is why the discharge gaps for most atmospheric pressure discharges are from mm to several cm. On the other hand, from the applications point of view, the short discharge gaps significantly limit the size of the objects to be treated if direct treatment (when the object is placed between the gaps) is desired. If indirect treatment (the object is placed next to the gaps and the active radicals of the plasma reach the object by flowing with the gas) is applied, active radicals with short lifetimes and charged particles may already disappear before reaching the sample to be treated. To overcome the shortcomings of the

traditional atmospheric pressure non-equilibrium plasmas, plasmas generated in open space rather than in a confined discharge gap are needed. However, when a plasma is to be launched in open space where the applied electric field is normally quite low, it is extremely difficult to sustain the existence of the plasma. Various methods were developed to overcome these challenges and several sources based on different designs were subsequently reported [4].

Most of the non-equilibrium or cold APPJs are working with a noble gas mixed with a small percentage of reactive gases, such as O_2. APPJs operating with noble gases can be classified into four categories, i.e. dielectric-free electrode (DFE) jets, dielectric barrier discharge (DBD) jets, DBD-like jets, and single electrode (SE) jets [4].

For DBD jets, as shown in Figure 1.4, there are many different configurations. As shown in Figure 1.4a [5] the jet consists of a dielectric tube with two metal ring electrodes on the outer side of the tube. When a working gas (He, Ar) flows through the dielectric tube and kHz high-voltage (HV) power supply is turned on, a cold plasma jet is generated in the surrounding air. The plasma jet only consumes a power of several watts. The gas temperature of the plasma is close to room temperature. The gas flow velocity is ~20 m/s. The plasma jet, which looks homogeneous to the naked eye, is actually a 'bullet'-like plasma volume with a propagation speed of more than 10 km/s [4]. It is believed that the applied electric field plays an important role in the propagation of the plasma bullet.

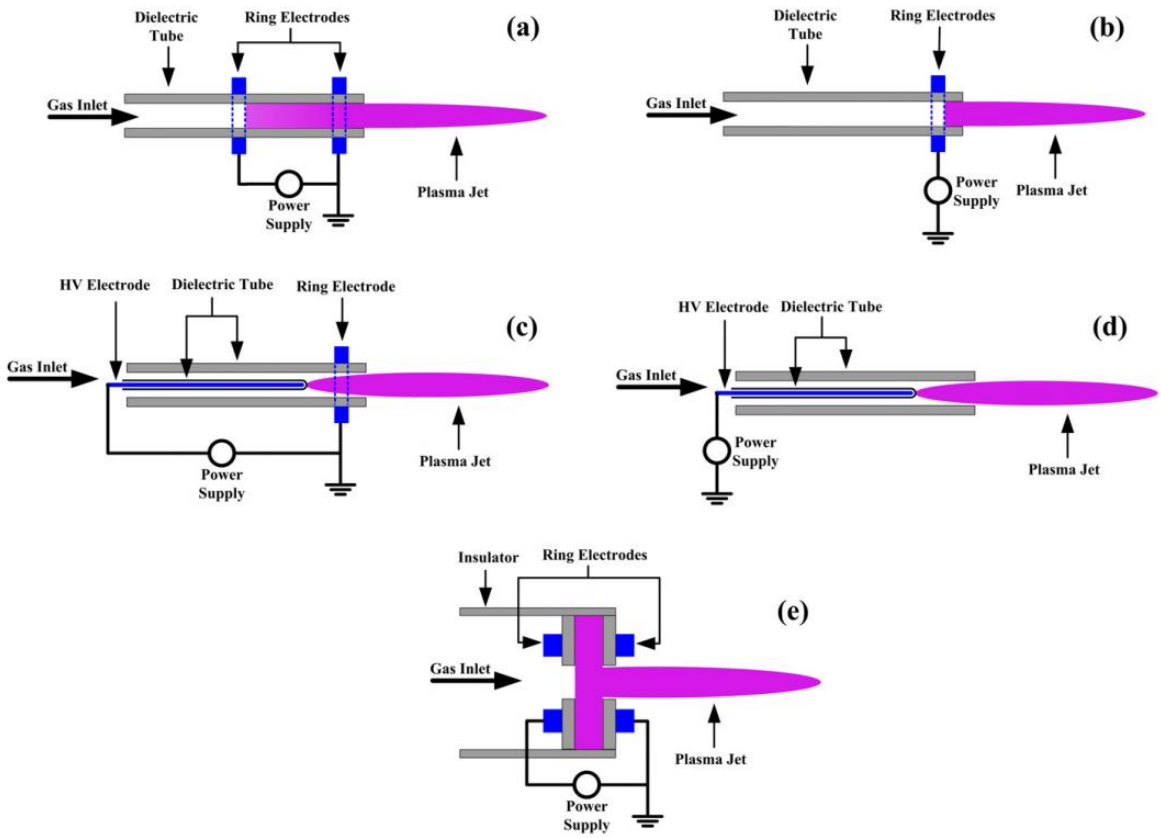

Figure 1.4: DBD plasma jets [4].

In Figure 1.4b [6] the one ring electrode is eliminated, so the discharge inside the dielectric tube is weakened. In Figure 1.4c [7] the HV ring electrode is replaced with a centered pin electrode, which is covered by a dielectric tube with one end closed. With this configuration, the electric field along the plasma plume is enhanced. A high electric

field along the plasma plume is favorable for generating long plasma plumes and more active plasma chemistry [8]. In Figure 1.4d [9] the ground ring electrode of Figure 1.4c is removed, so the discharge inside the tube is also weakened. On the other hand, a stronger discharge inside the discharge tube (as in the case of Figures 1.4a and 1.4c) helps the generation of more reactive species. With the gas flow, the reactive species with relatively long lifetimes may also play an important role in various applications. The configuration of Figure 1.4e [10] is different from the previous four DBD jet devices. The two ring electrodes are attached to the surface of two centrally perforated dielectric disks. The holes in the center of the disks are about 3mm in diameter. The distance between the two dielectric disks is about 5mm. With this device, a plasma plume of up to several centimeters in length can be obtained. All the DBD jet devices discussed above can be operated either by kHz ac power or by pulsed dc power. The length of the plasma jet can easily reach several centimeters or even longer than 10 cm. This capability makes the operation of these plasma jets easy and practical. There are several other advantages of the DBD jets. Firstly, due to the low power density delivered to the plasma, the gas temperature of the plasma remains close to the room temperature. Secondly, because of the use of the dielectric, there is no risk of arcing whether the object to be treated is placed far away or close to the nozzle. These two characteristics are very important for applications such as plasma medicine, where safety is a strict requirement [4].

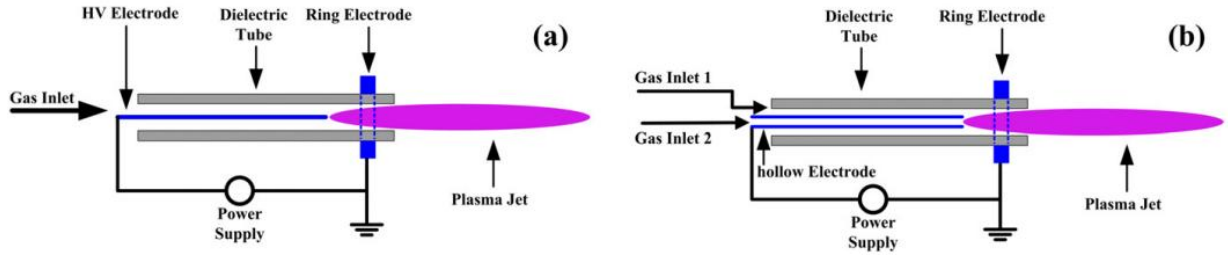

Figure 1.5: DBD-like plasma jets [4].

All the plasma jet devices shown in Figure 1.5 are named DBD-like jets. This is based on the following facts. When the plasma plume is not in contact with any object, the discharge is more or less like a DBD. However, when the plasma plume is in contact with an electrically conducting (a non-dielectric material) object, especially a ground conductor, the discharge is actually running between the HV electrode and the object to be treated (ground conductor). For such a circumstance, it no longer operates as a DBD. The devices shown in Figure 1.5 can be driven by kHz ac power, by RF power or by pulsed dc power. In Figure 1.5b the solid HV electrode of Figure 1.5a is replaced with a hollow electrode [11, 12]. The benefit of this kind of configuration is that two different gases can be mixed in the device. Normally, gas inlet 2 is used for a reactive gas such as O_2 flow, and gas inlet 1 is for a noble gas. It was found that the plasma plume is much longer with this kind of gas control than that using a pre-mix gas mixture with the same percentage. The role (and advantage) of the ring electrode in Figures 1.5a and 1.5b is the same as in the case of DBD jets. When the DBD-like plasma jets are used for plasma medicine applications, the object to be treated could be cells or whole tissue. In this case, these types of jet devices should be used carefully because of the risk of arcing. On the other hand, if it is used for treatment of conductive materials, since there is no dielectric, more power can easily be delivered to the plasma. So, as long as arcing is carefully avoided, the DBD-like jets have their own advantages [4].

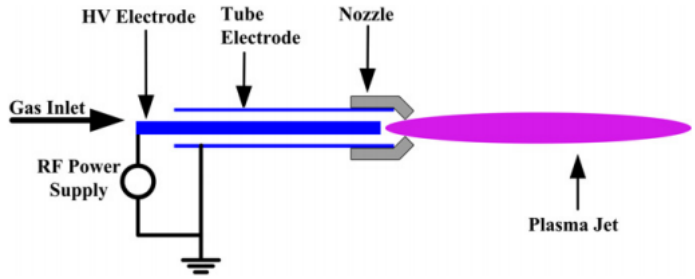

Figure 1.6: Schematic of a dielectric-free electrode (DFE) jet [4].

One of the early APPJs is a DFE jet, as shown in Figure 1.6 [13]. The jet is driven by a radio frequency (RF) power source at 13.56 MHz. It consists of an inner electrode, which is coupled to the power source, and a grounded outer electrode. A mixture of an inert gas with reactive gases is fed into the annular space between the two electrodes. Cooling water is needed to keep the jet from overheating and the gas temperature of the plasma jet varies from 50 to 300 ^{o}C, depending on the RF power [4]. Notable characteristics of the DFE jet (Figure 1.6) are, firstly, that arcing is unavoidable when the stable operation conditions are not met. Secondly, compared with DBD and DBD-like jets the power delivered to the plasma for the DFE jet is much higher. Thirdly, due to the high power delivered, the gas temperature of the plasma is quite high and out of the acceptable range for biomedical applications. Fourthly, for this DFE jet, which is driven by an RF power supply, the peak voltage is only a few hundred volts, so the electric field within the discharge gap is relatively low and its direction is radial (perpendicular to the gas flow direction). The electric field in the plasma plume region is even lower, especially along the plasma plume propagation direction (gas flow direction). Finally, since the electric field along the plasma plume propagation direction is very low, the generation of this plasma plume is probably gas flow driven rather than electrically driven. On the other hand, because a relatively high power can be delivered to the plasma and the gas temperature is relatively high, the plasma is very reactive. This kind of plasma jet is suitable for applications such as material treatment as long as the material to be treated is not very sensitive to high temperatures [4].

The schematics of single electrode (SE) jets are shown in Figures 1.7a–c. Figures 1.7a and 1.7b are similar to the DBD-like jets except there is no ring electrode on the outside of the dielectric tube. The dielectric tube only plays the role of guiding the gas flow.

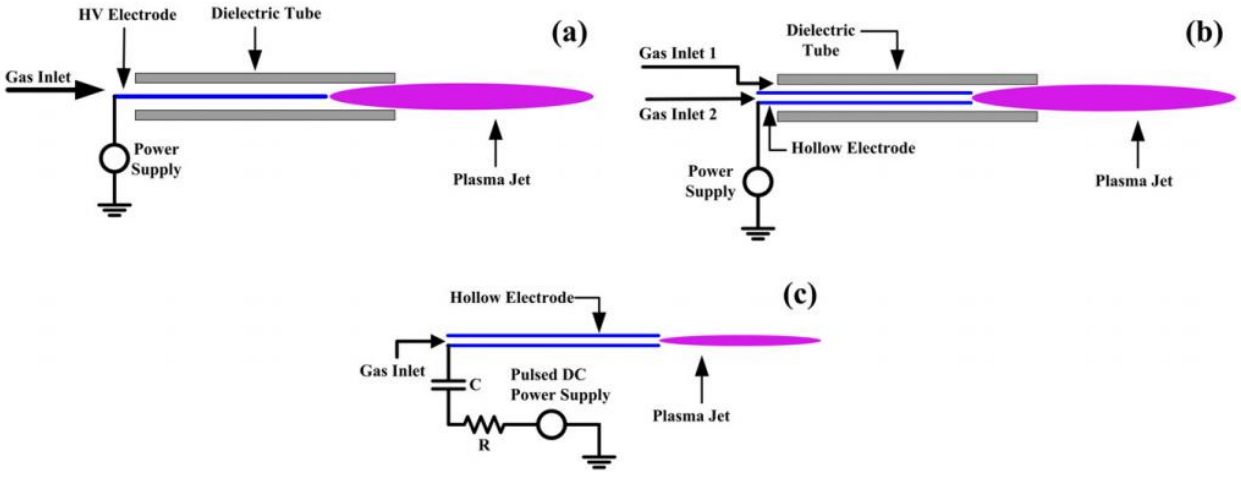

Figure 1.7: SE plasma jets [4].

These two jets (in Figures 1.7a and 1.7b) can be driven by dc, kHz ac, RF or pulsed dc power. Because of the risk of arcing, the plasma plumes generated by the jets in Figures 1.7a and 1.7b are not the best for biomedical applications due to safety issues [14]. In order to overcome this problem, a similar SE jet was developed, as shown in Figure 1.7c [15]; the capacitance C and resistance R are about 50 pF and 60 kΩ, respectively. The resistor and capacitor are used for controlling the discharge current and voltage on the hollow electrode (needle). This jet is driven by a pulsed dc power supply with a pulse width of 500 ns, repetition frequency of 10 kHz and amplitude of 8 kV. The advantage of this jet is that the plasma plume or even the hollow electrode can be touched without any risk of injury, making it suitable for plasma medicine applications. One of the potential applications is in dentistry, such as root canal treatment. Due to the narrow channel geometry of a root canal, which typically has a length of few centimeters and a diameter of one millimeter or less, the plasma generated by a plasma jet is not efficient to deliver reactive agents into the root canal for disinfection. Therefore, to have a better killing efficacy, a plasma needs to be generated inside the root canal, whereupon reactive agents, including the short-lifetime species, such as charged particles, could play some role in the killing of bacteria. Using the device of Figure 1.7c, a cold plasma could be generated inside a root canal [4].

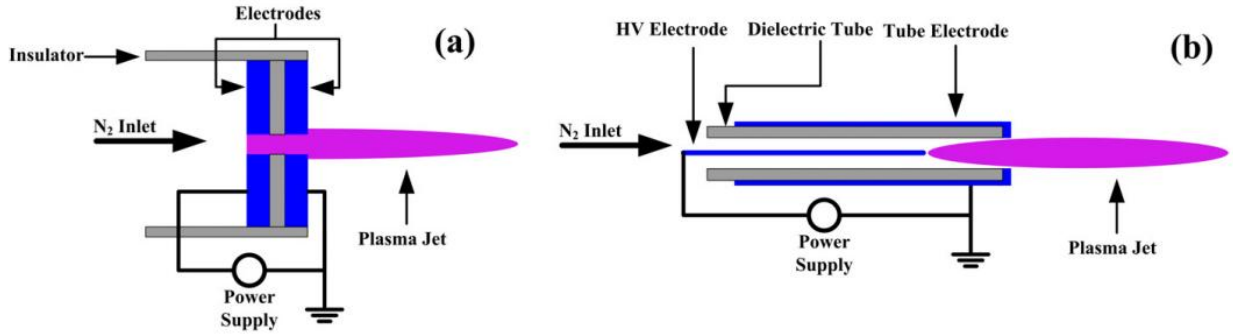

Figure 1.8: N_2 plasma jets [4].

All the devices described so far use a noble gas as feed. Due to its reactive nature and the importance of the chemical species that can generate, Nitrogen (N_2) can be very useful as feed gas. However, it is difficult to generate APPJs with N_2 as the feed gas. The reason for this, is the fact that despite having significantly lower ionization energy compared to He, with N_2, the electrons could quickly transfer their energy to molecular rotational and vibrational states because the energy levels of the rotational and vibrational states of the molecules can be much lower than that of the electrons' excitation and ionization. So the electrons in He discharges have larger energy than they have in N_2 discharges under similar conditions and the difference in this mean energy overcomes the difference in their ionization energy [4]. Figure 1.8 shows the schematic of two N_2 plasma jets. In Figure 1.8a [16], a 20 kHz ac power supply is connected to two electrodes of thickness 3mm and a center hole of diameter 500μm. The two electrodes are separated by a dielectric disk with a center hole of the same diameter. With this configuration, a N_2 plasma up to 6.5 cm long can be generated. When the N_2 gas flow rate is 6.3 slm (standard liters per minute), the gas is ejected out from the hole at a speed of about 535 m/s. The gas temperature of the plasma plume at 2 cm from the nozzle is below 300K. Figure 1.8b [17] shows a slightly different N_2 plasma jet device, which replaces the inner perforated HV electrode of Figure 1.8a by a pin electrode. The inner electrode can also be replaced by a tube [4].

Due to the presence of electronegative oxygen, O_2, in air it is difficult to sustain an APPJ without a different feed gas. Nevertheless, several different air plasma jets have

been reported [4]. In Figure 1.9a [18], a discharge channel through an insulator with a thickness of about 0.2–0.5mm and a diameter of 0.2-0.8mm separates the anode and the cathode, which have a center hole of the same diameter. The ballast resistor is 51 kΩ. When air flows through the hole and a dc voltage of a few hundred volts (up to a kV) is applied between the anode and cathode (depending on the thickness of the insulator separating the electrodes), a relatively low temperature air plasma is generated in the surrounding air with length up to 1 cm, depending on the gas flow rate and discharge current. However, the gas temperature of the plasma can still be quite high. The gas temperature within the micro-gap is about 1000K. However, it drops quickly as it propagates in the surrounding air. It is about 323 K at 5mm away from the nozzle for an air flow rate of 200 ml/min and discharge current of 19 mA. In Figure 1.9b [19], a porous alumina dielectric is used to separate the HV stainless steel (typical injection needle) electrode and the outer ground electrode [4].

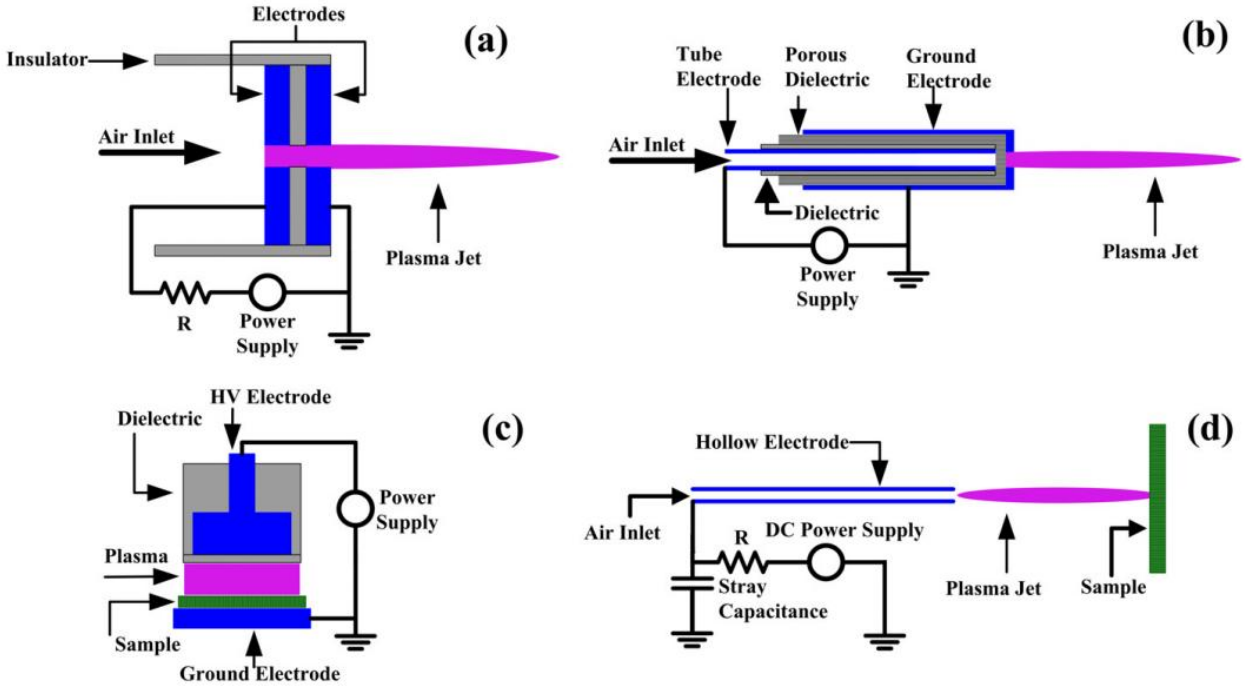

Figure 1.9: Air plasma jets [4].

The alumina used in this device has approximately 30 vol% porosity and has an average pore diameter of 100μm. The ground electrode is fabricated from stainless steel and has a centrally perforated hole of 1mm diameter through which the plasma jet is ejected to the surrounding ambient air. When 60Hz HV power supply is applied and the flow rate of air is at several slm, an APPJ up to about 2 cm is generated in the surrounding air. During one voltage cycle, there are multiple discharges. The increase in the input power results in more current pulses. The shortcoming of this device is that the gas temperature of the plasma is quite high. It is about 60^{o}C at 10mm away from the nozzle for an air flow rate of 5 slm. For lower flow rates, the gas temperature is even higher. Figures 1.9c and 1.9d [20, 21] are the schematics of two 'floating' electrode air plasma jets. Strictly, they are not plasma jets since the plasmas are generated within a gap. However, because the secondary electrode (ground electrode) can be a human body, they are categorized as plasma jets. Both jets could generate room temperature air plasmas. They are completely safe from the electrical perspective and non-damaging to animals or human beings. For Figure 1.9c, kHz ac or pulsed dc voltage with an amplitude of 10–30 kV is used to drive the device. The discharge ignites when the powered electrode approaches the surface to be treated at a distance (discharge

gap) of less than about 3mm, depending on the form, duration and polarity of the driving voltage. This jet is suitable for large smooth surface treatment. In contrast, the jet shown in Figure 1.9d is more suitable for localized three-dimensional treatments. The output voltage of the power supply can be adjusted up to 20 kV. The output of the power supply is connected to a stainless steel needle (typical injection needle) electrode through a resistor R of 120MΩ, which is several orders of magnitude higher than those reported. When a counter-electrode, such as a finger, is placed close to the needle, a plasma is generated. The plasma is similar to the positive corona discharge. However, this jet can be touched by the human body directly, which is not the case for the traditional corona discharge. The jet has no risk of glow–arc transition. The maximum length of the plasma is about 2 cm. The gas temperature of the plasma is kept at room temperature. It is interesting to point out that the discharge is actually pulsed. It appears periodically with a pulse frequency of tens of kHz, depending on the applied voltage and distance between the tip of the needle and the object to be treated. It should be pointed out that all these air plasma jets (Figures 1.9a-d) can also be operated with N_2 gas. On the other hand, the device shown in Figure 1.8a can be operated with air too. But the maximum length of the air plasma plume operated with the jet shown in Figure 1.8a is about 2 cm. In addition, the jet shown in Figure 1.7c can be operated with air as a working gas [22]. But the length of the plasma is only several millimeters [4].

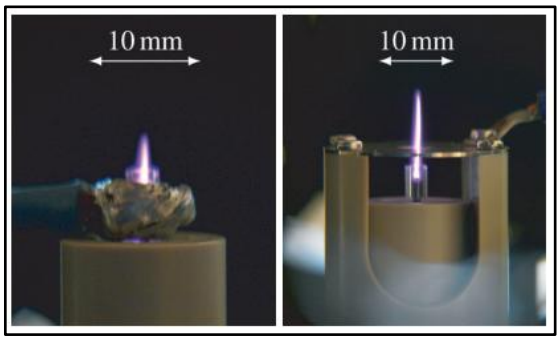

(a) ring electrode (b) plate electrode

Figure 1.10: Plasma jets used by van Gessel et al [24].

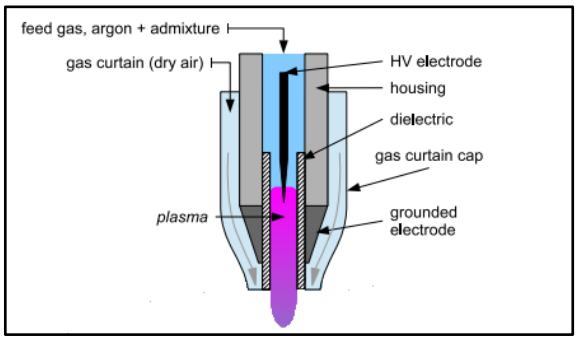

Figure 1.11: Kinpen jet [23].

The device used by van Gessel et al [24] (Figure 1.10) are DBD plasma jets with (a) being the type of Figure 1.4c and (b) the type of Figure 1.5a. The Kinpen jet (Figure 1.11) belongs to the plasma jets category of Figure 1.4c and the device of Figure 1.12 resembles the device of Figure 1.5a but with a different geometry of the HV electrode.

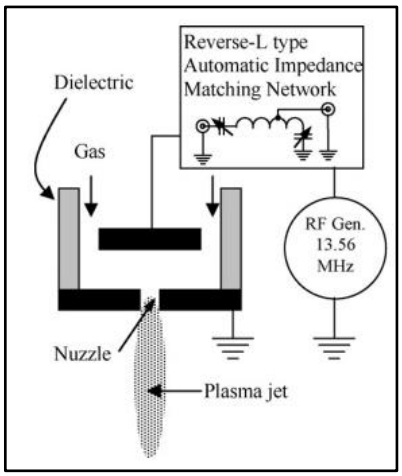

Figure 1.12: Device used by Ionita et al. [25].

1.4 Simulation of atmospheric pressure plasma jets

Nowadays, with the increase of the computational power of modern computer systems, it is possible to simulate plasma reactors and devices with detailed models (thermal, electromagnetic, convective and reaction chemistry/kinetics phenomena solved self-consistently). This is very common in practice, especially with low pressure plasma reactors which are used widely for micro- and nano-manufacturing.

Atmospheric plasma jet devices operate in open atmosphere (no enclosure, in contrast with low pressure plasma devices) where atmospheric air can enter the device and the jet. The presence of atmospheric air leads to large reaction sets that it can be computationally very costly to be simulated using detailed 3d or 2d models, even with the aid of advanced computer systems. The models for atmospheric plasma jet devices typically include kinetics for hundreds of species and thousands of reactions [26-31].The number of species and reactions is much higher compared to low pressure plasma reactors. Reduced chemistry set atmospheric plasma jet models could be used for simulation but they may lack the accuracy required for certain applications.

For the description of spatial distributions of the generated reactive species, 2d or 1d models are used. 2d models give information on the distributions of the produced reactive species both along and across planar or cylindrical plasma jets. In [26], 2d simulations were performed with the fluid dynamics code nonPDPSIM which has been originally designed and realized by Kushner and co-workers [32]. The feed gas (He) flows between two closely spaced stainless steel electrodes driven at 13.56MHz radio-frequency in a parallel plate configuration. Electrodes, plasma volume and effluent are enclosed by quartz windows, giving direct optical access to the plasma itself and the effluent volume behind the electrodes. The presented jet configuration features a dielectric extension of the gas channel to assure controlled gas flow in the effluent behind the plasma. Typical gas velocities are around 100 m/s and 160 reactions are included in the model. The device resembles the DFE jet shown in Figure 1.6.

In [27], 2d simulations were performed with the commercial code Comsol. The micro-plasma jet consists of two parallel stainless steel electrodes (30mm long, 1mm thick) separated by a gap of 1mm. One electrode is powered by an RF power supply (13.56 MHz, absorbed power <1W), while the other one is grounded. The gas flow is 1.4 slm He with a small admixture of O_2 (<1.6%) with 10 reactions included in the model. The device resembles the DFE jet shown in Figure 1.6.

In [31], 1d simulations were performed with Comsol and Matlab. The setup of the investigated μAPPJ consists of two planar stainless steel electrodes of tens of millimeters in length, 1mm thickness and 1mm distance. One electrode is grounded and the other one is driven at 13.56MHz. The discharge channel of 1x1 mm^2 cross section is guided by the electrodes. Both front and back of the entire channel are covered by quartz windows. The gas velocity is 10 m/s with a gas composition of helium/oxygen (1000:5) and a reaction set of 116 reactions. The device resembles the DFE jet shown in Figure 1.6.

In [29], 1d simulations were performed with Comsol. The setup consists of two plane parallel stainless steel electrodes. Quartz windows enclose the discharge region along the sides. The core plasma channel has a cross-section of 1mm × 1mm over a length of 30mm. Typical operational parameters are a helium feed gas flow up to 2 slm (mean gas velocity of about 17m/s) with a molecular oxygen admixture of 0.5%. One electrode is driven at 13.56MHz while the other one is grounded. 184 reactions are included in the model. The device resembles the DFE jet shown in Figure 1.6. In [30], 0d simulations were performed with the Global_Kin code developed by Dorai and Kushner [33]. The

plasma source consists of an RF-driven tungsten needle with a diameter of 1mm and a sharpened tip surrounded by a glass tube with a 3mm outer and a 1.5mm inner diameter. A gas flow of Ar is applied through the tube. The gas flow is kept constant at 2 slm. The setup is not in a vacuum vessel and thus open to air. A grounded copper electrode is positioned at a distance of 5mm from the needle. It has a hole with a diameter of 5mm through which the plasma can penetrate. The RF frequency is 11.7 MHz. The electrical field and the gas flow have the same direction. 1880 reactions are included in the model. The device resembles the DBD jet shown in Figure 1.4c.

In [28], 0d simulations were also performed simulating a device consisting of two circular electrodes with radius of 1 cm, separated by a gap of 500 μm. The gas flow ($He+H_2O$) is 100 sccm and 577 reactions are included in the model. The device resembles the DFE jet shown in Figure 1.6.

1.5 Aim and structure of this work

πlasma-R [34] is a code used for the simulation of low pressure plasma reactors: Global modeling is implemented by a user-friendly graphical user interface (Figure 1.13). The user can define the sets for reactions in the bulk plasma and on the reactor walls, as well as the operating parameters in a text file and πlasma-R formulates the balances and solves the system of equations. The model computes the density of the species and the temperature of the electrons.

The aim of this work is to extend πlasma-R in order to simulate APPJs. In particular, the model is formulated at transient state, and a fast solver for stiff problems, namely LSODA, is integrated for the numerical solution. By transforming the transient solution to a spatial solution (1d) through the flow velocity, the extended model will calculate the active species densities and electron temperature along the distance from the device exit. The extended model is not self-consistent: It requires several experimental measurements such as the flow velocity along the distance from the device exit for the numerical solution.

The work of Gaens&Bogaerts [30] which a simulation of an APPJ device (used for biomedical applications with Ar as the feed gas) [35], is used as a benchmark in order to verify the results of the extended model. In order to investigate the effect of the electron energy distribution function (EEDF) on the results the calculations are performed by both a Maxwellian EEDF and an EEDF coming from a Boltzmann equation solver, namely Bolsig+ [36]; the solver calculates the EEDF but only for a limited number of conditions. To minimize the use of the Boltzmann equation solver (which is external to the extended global model), the EEDF is considered constant in spatial spaces along the jet.

Finally, in an attempt to develop a self-consistent model for APPJs and eliminate the need for inputs from experimental measurements, 2d fluid simulations of the jet, decoupled from the plasma simulation, are made with Comsol by using both laminar and several turbulent models.

The structure of this thesis follows: In Chapter 2, the mathematical formulation of the global model is described (for low pressure plasma discharges and for plasma jets) and various methods of solving ordinary differential equations are presented with focus on the LSODA solver. In Chapter 3, the results of the simulation of a plasma jet device [35] using a global model are presented along with the effects of various EEDFs on the results. In Chapter 4, a short description of turbulence (and turbulence modeling) is presented and the results of a 2d fluid flow simulation with Comsol are discussed. The conclusions are described in Chapter 5.

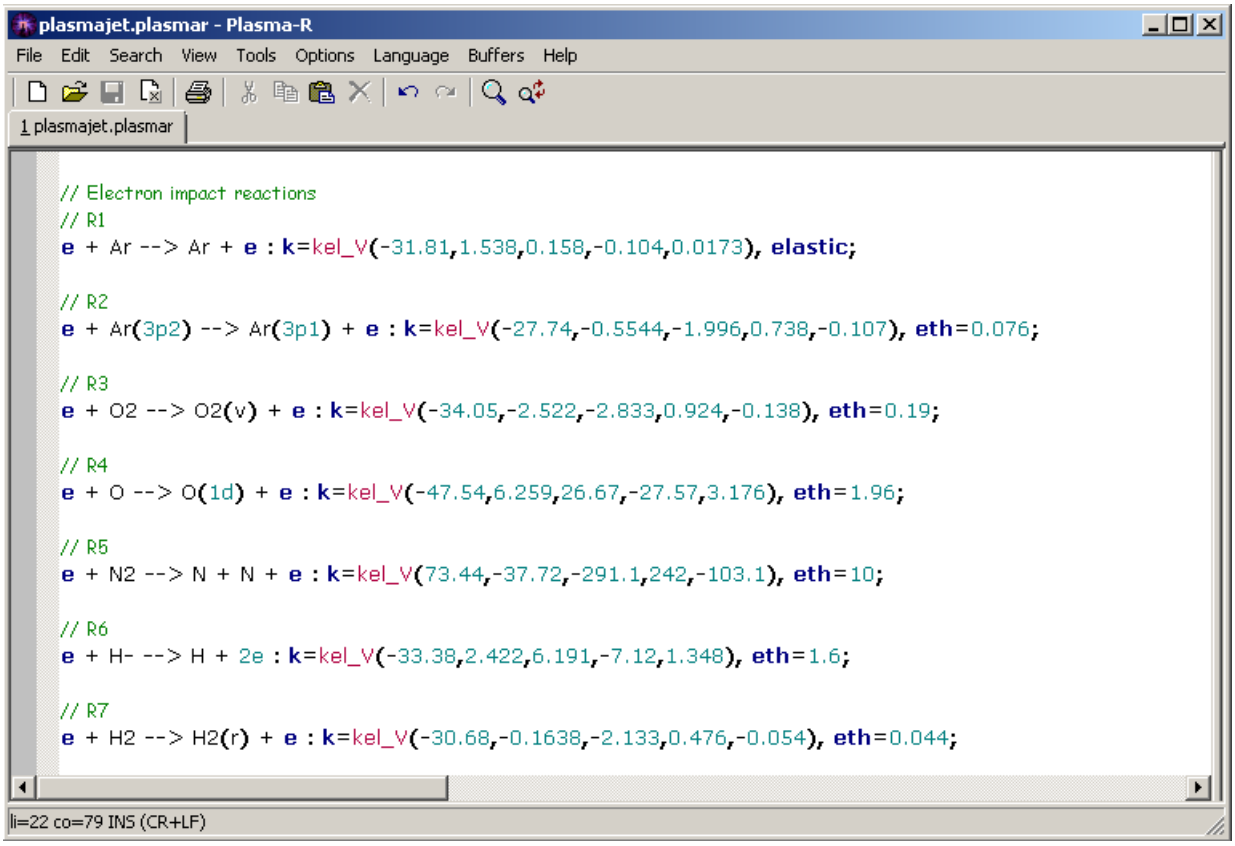

Figure 1.13: A snapshot of the πlasma-R editor, used to define the reaction set and the operating parameters.

2. MODEL

2.1 Introduction

Multidimensional detailed models are widely used for plasma simulations and usually their solution entails a high computational cost (in time and memory). The number of unknown variables, and as a consequence the computational cost, further increases when the number of species being taken into account increases. This is the case with atmospheric plasma jet devices, which are not enclosed: A large number of species have to be taken into account in the reaction set due to the presence of air containing O_2, N_2, and H_2O. Instead of using computationally costly detailed models, a global model is proposed for the simulation of such systems. In particular, a homemade code for global modeling in low pressure plasma reactors, namely πlasma-R [34], is extended to handle cases of atmospheric pressure plasma jets.

2.2 Global model for low pressure plasma reactors [34]

A global model is essentially a zero dimensional model (0d model), i.e. no spatial variations of variables can be resolved. Instead, spatially, volume averaged quantities are used. Global models can be solved at steady or transient state. They can give results in a very short amount of time and consist of species mass equations and an electron energy balance in 0d (volume averaged balances).

The generic mass balance for species i in the gas phase (neutral or charged except for electrons) in a low pressure plasma reactor is formulated as:

$$\frac{dn_i}{dt} = \frac{Q_{f,i}}{V k_B T_0} - \frac{S_p}{V} n_i + \sum_{j=1}^{N_{r,bulk}} R_{i,j}^{bulk} + \frac{1}{V} \sum_{m=1}^{N_A} A_m \sum_{k=1}^{N_{r,surf,m}} R_{i,k}^{surf,m} \quad (Eq. 2.1)$$

where n_i and $Q_{f,i}$ is the number density (m^{-3}) and the feed (m^3Pa/s) of species i. V is the volume of the reactor (m^3) and S_p is the volumetric flow (m^3/s) at the outlet. k_B is the Boltzmann constant and T_0 is a reference temperature (293 K). N_A is the number of surfaces in the reactor and A_m is the area of surface m. $N_{r,bulk}$ is the number of the gas phase reactions. $N_{r,surf,m}$ is the number of surface reactions on a surface m of the reactor. $R_{i,j}^{bulk}$ is the production rate of species i by reaction j in the gas phase and $R_{i,k}^{surf,m}$ is the production rate of species i by reaction k on surface m. The reactions in the gas phase and on the surface are considered as elementary; thus, the reaction rates, and as a consequence $R_{i,j}^{bulk}$ and $R_{i,k}^{surf,m}$, come from the law of mass action. The generic surface site balance for a species i on the surface reads:

$$\sigma_m \frac{d\theta_{i,m}}{dt} = \sum_{k=1}^{N_{r,surf,m}} R_{i,k}^{surf,m} \quad (Eq. 2.2)$$

where A_m is the area (m^2) of the inner surface m and σ_m is the surface density of sites (m^{-2}) on surface m. $\theta_{i,m}$ is the surface coverage of surface m by species i.

The generic energy balance for electrons reads:

$$\frac{d}{dt}(n_e \varepsilon_e) = \frac{P_{ads}}{V} - \sum_{j=1}^{N_{r,bulk}} R_{e,j}^{bulk}\, \varepsilon_{th,j} - \frac{1}{V}\sum_{m=1}^{N_A} A_m \sum_{k=1}^{N_{r,surf}} R_{+,k}^{surf,m}\left(\varepsilon_{e,surf} + \varepsilon_{+,surf}\right) - \frac{S_p}{V}\left(n_e \varepsilon_e + \sum_{l=1}^{N_+} n_{l,+}\varepsilon_+\right) \quad (Eq.\,2.3)$$

where n_e is the electron density (m^{-3}). N_+ is the number of positive ions, P_{ads} is the adsorbed power by the plasma (Watts) and $e_{th,j}$ is the energy loss of the electrons by (electron impact, see the index "e") reaction j (eV). In the case of an elastic collision:

$$\varepsilon_{th} = 2\frac{m_e}{m_i}\varepsilon_e \quad (Eq.\,2.4)$$

where m_e and m_i are the masses of the electron and the neutral species i joining the elastic collision. ε_e is the electron energy (eV) which is related to the electron temperature, T_e(eV),

$$\varepsilon_e = \frac{3}{2}T_e \quad (Eq.\,2.5)$$

e_+ is the ion energy (eV) which is related to the ion temperature T_+ (eV)

$$\varepsilon_+ = \frac{3}{2}T_+ \quad (Eq.\,2.6)$$

T_+ is calculated by the equation proposed by Lee and Liebermann [34]

$$T_+ = \begin{Bmatrix} 0.5 - \frac{T_{gas}}{11605} \\ p \end{Bmatrix} + \frac{T_{gas}}{11605}, \begin{matrix} p > 1\ mTorr \\ else \end{matrix} \quad (Eq.\,2.7)$$

where p is the pressure in the reactor in mTorr and T_{gas} is the gas temperature (K). $\varepsilon_{e,surf}$ is the energy lost (eV) per electron lost to the inner surfaces of the reactor and reads [37]

$$\varepsilon_{e,surf} = 2T_e \quad (Eq.\,2.8)$$

$\varepsilon_{+,surf}$ is the energy lost (eV) per ion lost to the inner surfaces of the reactor and is typically between 5 and 8 eV in high density sources [37]. We choose

$$\varepsilon_{+,surf} = 6.5T_e \quad (Eq.\,2.9)$$

Finally, the electron density is calculated by the charge neutrality of the plasma.

Regarding the reaction rate coefficients, for electron impact reactions the coefficients are coming from integration of the pertinent cross sections over the electron energy distribution function; they are usually fitted to the following formulas. The first is

$$k_{G,el} = exp\left(A + BlnT_e + \frac{C}{T_e} + \frac{D}{T_e^2} + \frac{E}{T_e^3}\right) \quad (Eq.\,2.10)$$

and the second formula is

$$k_{G,el} = AT_e^B exp\left(-\frac{C}{T_e}\right) \ (Eq. 2.11)$$

Regarding the gas phase reactions between neutral species, the reaction rate coefficients are expressed by the Arrhenius formula, i.e.

$$k_{G,n} = AT_{gas}^B exp\left(-\frac{C}{T_{gas}}\right) \ (Eq. 2.12)$$

The general form of a rate coefficient of a reaction on surface m which a neutral species i joins is:

$$k_{S,m,n} = \left(s_{i,m} or k_{rec,i,m}\right)\frac{u_{th,i}}{4}\frac{A_m}{V} \ (Eq. 2.13)$$

where $s_{i,m}$ is the sticking probability on surface m, given that surface m is clean. $k_{rec,i,m}$ is the recombination probability of i on surface m, given that it is fully covered by the "parter"-species of i in the recombination. $u_{th,i}$ is the thermal velocity of i.

The general form of a rate coefficient of a rate coefficient of a reaction on surface m which an ion i joins is:

$$k_{S,m,+} = \frac{U_{b,i}}{V}\sum_{m=1}^{n_A} h_{m,i}A_m \ (Eq. 2.14)$$

where $U_{b,i}$ is the Bohm velocity of ion i. $h_{m,i}$ is the ratio of the sheath (formed before surface A_m) edge density to the average bulk density of ion i. $h_{m,i}$ depends on several quantities such as the ratio of negative ion density to electron density, ratio of ion temperature to electron temperature, the dimensions of the reactor, and is approximated by the equations described in the work of Lee and Lieberman [34]:

$$h_{m,i} = \begin{cases} \dfrac{1+\frac{3a_{avg}}{\gamma}}{1+\alpha_{avg}} \dfrac{0.86}{\left(3+\frac{L}{2\lambda}+\left(\frac{0.86LU_{b,i}}{\pi D_a}\right)^2\right)^{0.5}}, & (A_m notcylindrical) \\ \dfrac{1+\frac{3a_{avg}}{\gamma}}{1+\alpha_{avg}} \dfrac{0.8}{\left(4+\frac{R}{\lambda}+\left(\frac{0.8RU_{b,i}}{2.405(J_1(2.405))D_a}\right)^2\right)^{0.5}}, & (A_m cylindrical) \end{cases} \quad (Eq. 2.15)$$

where a_{avg} is the ratio of the density of negative ions to the density of electrons, i.e.

$$a_{avg} = \frac{\sum_{i=1}^{N_-} n_{i,-}}{n_e} \ (Eq. 2.16)$$

γ is the ratio of electron temperature over the ion temperature, i.e.

$$\gamma = \frac{T_+}{T_e} \ (Eq. 2.17)$$

λ is the mean free path (m) of ion-neutral collisions, i.e.

$$\lambda = \frac{1}{\sigma_\lambda \sum_{i=1}^{N_n} n_{i,n}} \ (Eq.2.18)$$

where N_n is the number of neutral species and σ_λ is the cross section for ion-neutral collisions (m^2). D_a is the ambipolar diffusion coefficient (m^2/s)

$$D_a = \frac{\mu_+ D_e + \mu_e D_+}{\mu_+ + \mu_e} \ (Eq.2.19)$$

where T_+ is in K. μ_e is the mobility of electrons which is calculated as

$$\mu_e = \frac{|q|}{m_e \nu_{m,e}} \ (Eq.2.20)$$

where m_e is the electron mass. $\nu_{m,e}$ is the frequency of electron-neutral collisions which is calculated as

$$\nu_{m,e} = \frac{1}{n_e} \sum_{j=1}^{N_{r,bulk}} \frac{1}{\nu_{e,j}} R_{e,j}^{bulk} \ (Eq.2.21)$$

where $\nu_{e,j}$ is the stoichiometric coefficient of electrons in reaction j.

Getting back to Eq.2.15, J_1 is the Bessel function of the first order, R and L are the radius and the length of the source tube or the main chamber depending on the cylindrical chamber which A_m belongs to. The Eq. 2.15 was the result of a heuristic matching of equations for the loss of ions at walls in electronegative and electropositive discharges, and can be used for transitions from low to high pressure and electropositive to electronegative regimes. It was originally proposed for an inductively coupled reactor with one chamber and its derivation was based on the assumption that there was only one positive ion.

The inputs of the model are the adsorbed power (P_{ads}), the pressure in the reactor before the discharge (p_{off}), the feed of the reactor (Q_f) and the gas temperature (T_{gas}). Additionally, the cross section for ion-neutral collisions (σ_λ) is required as well as the temperature of the gas before the discharge (T_{off}). It is assumed that $T_{off} = T_{gas}$. T_{off} and p_{off} are required for the calculation of the volumetric flow rate at the outlet:

$$S_p = \frac{Q_f}{p_{off}} \frac{T_{off}}{T_0} \ (Eq.2.22)$$

The set of inputs includes also the reactions sets and the reactor dimensions. The outputs of the model are the densities of neutral and charged species and electrons, the surface coverage, and the temperature of electrons.

Applications of the first versions of πlasma-R in low pressure plasma reactors are included in references [38-40].

2.3 Global (0d) model for plasma jets

The focus of this work is on plasma jet devices and in particular, needle tip jet devices where a metallic needle with a sharpened tip becomes the high voltage electrode and the other electrode (ground) is a metallic surface with a hole to allow the passage of the jet stream. Such a device is shown in Figure 2.1.

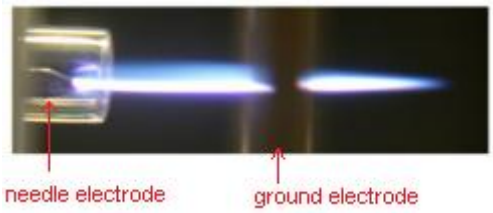

Figure 2.1: Needle tip plasma jet device [35].

When developing plasma jet models, a very important aspect, as far as the results are concerned, is the densities of the various species as a function of the distance from the device. Since global models solve for spatially averaged quantities (uniformity), it is impossible to calculate differences in the quantities along a dimension with such a model. In order to include such information in the solution of a global model an approximation called the 'pseudo-1D plug flow' is used. In this way, it is possible to represent the time dependent evolution of species densities (as is typically the case in a 0d model) as a spatial dependence and the transient solution (vs time) of the global model is transformed into a solution vs distance [30].

First of all, it is assumed that the tube of the plasma jet device, the plasma jet itself and the afterglow region in the far effluent can be represented by a long cylinder (Figure 2.2), where constant atmospheric conditions rule. The magnitude of the flow velocity determines the position of a volume averaged (0d) plug element, i.e. a cylindrical segment, along the jet stream (Figure 2.2).

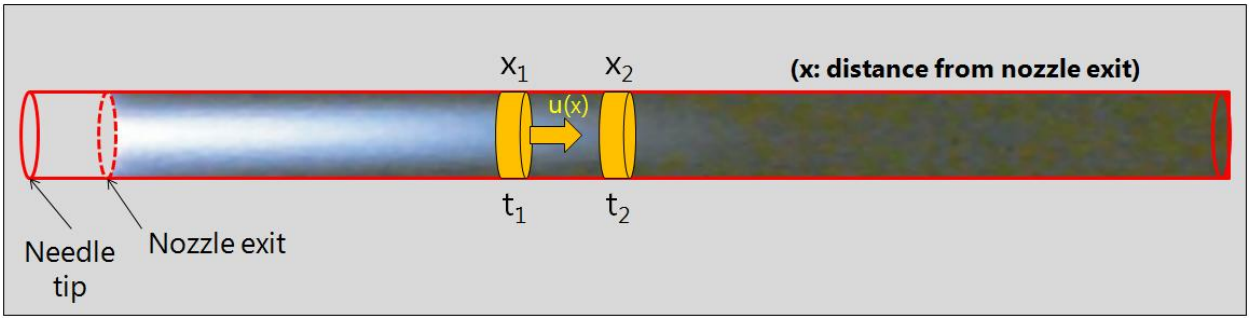

Figure 2.2: Cylinder representing the three regions of interest and the motion of the plug element.

The velocity along the cylinder is not a linear function of distance from the device. The velocity relation is

$$u = \frac{dx}{dt} \Rightarrow dt = \frac{1}{u(x)}dx \Rightarrow \int_{t1}^{t2} dt = \int_{x1}^{x2} \frac{1}{u(x)}dx \qquad (Eq.2.23)$$

Eq. 2.23 allows the transformation of time into distance and vice versa. The 'pseudo-1D plug flow' approximation is valid when some assumptions are made. First of all, it is assumed that axial diffusion of mass and energy is negligible in comparison with axial transport by convection. This means that the conditions in a cylindrical segment do not affect the cylindrical segments before it. Furthermore, no species transport in the radial

direction is considered in this approach. Again, this seems acceptable for the first few centimeters after the nozzle exit due to the very high axial flow speed compared with the radial flow speed. Transport in the radial direction is indirectly included and only for the species Ar, N_2, O_2, H_2O (these species are inputs) [41].

In order to describe the problem of a plasma jet using the global model, some modifications of the equations used for the global model of plasma reactors need to take place. The main difference is the absence of wall surfaces for a plasma jet and as a result, every term of the equations for plasma reactors that includes surfaces is not present in the formulation of the global model for plasma jets. In addition, there are no gas feed terms (although there is an equivalent) or outlet. The model needs to be solved at transient state (as a function of time) since the transient solution is transformed into the solution vs distance (plug flow approximation).

The mass balance for a heavy species i in the gas phase (neutral or charged species) becomes

$$\frac{dn_i}{dt} = \sum_{j=1}^{N_r} R_{i,j} \quad (Eq.\,2.24)$$

$$i \neq feedgas, N_2, O_2 or H_2O$$

where n_i is the density of species i, N_r is the number of gas phase reactions and $R_{i,j}$ is the production rate of species i in reaction j. No losses of mass are considered for the walls of the cylindrical segment.

The electron energy balance becomes:

$$\frac{d}{dt}\left(\frac{3}{2} n_e T_e\right) = \frac{P_{ads}}{V} - \sum_{j=1}^{N_r} R_{e,j}\, \varepsilon_{th,j} \quad (Eq.\,2.25)$$

where n_e is the electron density, T_e is the electron temperature, P_{ads}/V is the adsorbed power density, $\varepsilon_{th,j}$ is the threshold energy of reaction j and $R_{e,j}$ are the electron impact reaction rates (elastic and inelastic). No losses of energy are considered for the walls of the cylindrical segment.

Finally, the electron density is calculated by the charge neutrality of the plasma.

The inputs of the model are the densities of the feed gas, N_2, O_2 and H_2O, the gas temperature, the power density and the flow velocity versus the distance from the nozzle. The outputs are the species densities and the electron temperature versus the distance from the nozzle (Figure 2.3). The plug flow velocity is used to convert the input functions of *x* (distance) to functions of *t* (time) as well as to convert the densities' and electron temperature profiles versus *t* to profiles versus *x*. The model's equations are solved inside the cylindrical segment (time domain). The inputs (average values) inside the segment are used to produce the outputs for different time instances. The time instances can then be transformed to distances by using the flow velocity (Eq. 2.23). Eq. 2.23 produces a relation $t = f(x)$. If $u(x)$ is selected carefully (e.g. Ae^{-Bx}), the relation $t = f(x)$ can be easily solved for x ($x = g(t)$).

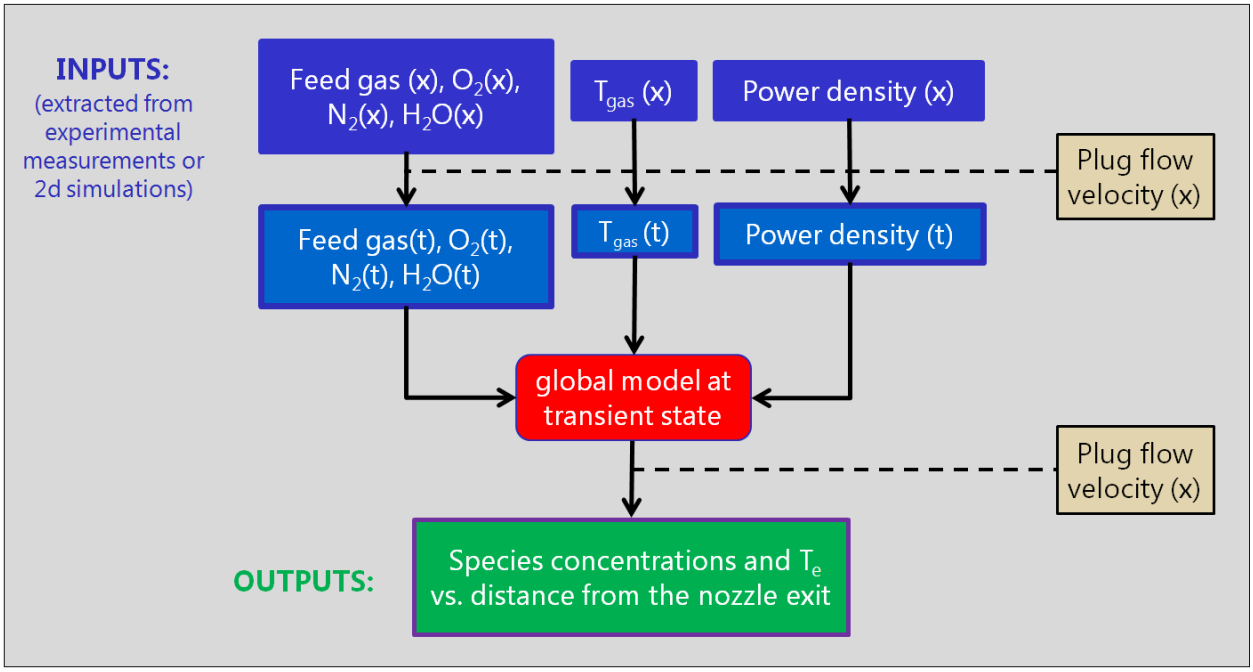

Figure 2.3: Inputs and outputs of the plasma jet global model.

In an experimental setup, the value of the electric field throughout the plasma jet is significantly dependent on the applied electrode voltage, the electrode configuration, etc. Moreover, it fluctuates in time. Unfortunately, this complexity cannot be captured by a 0d kinetics model. Therefore, the Joule heating term is determined by an estimated power deposition density (Wm^{-3}) profile used as input in the model. This profile entails a maximum power density at the needle electrode tip and a linear decrease of power density along the plasma jet flow [30, 41]. To measure the power deposition profile further from the needle tip is highly non-trivial. It is known, however, from the literature that plasma jets typically show UV–vis light emission over a distance in the order of maximum a few centimeters. Processes that can generate extra electrons, for example secondary electron emission at the needle electrode tip, cannot be included in this simple model. Finally, propagating ionization wave fronts, created by electron avalanches due to photo-ionization processes, cannot be taken into account either, but might result in a higher electron density as well.

The gas temperature is very important for the formation of biomedically important species from humid air species. In a needle type plasma jet the gas temperature typically varies largely, both in the radial and axial direction. In fact, the gas temperature can be—in terms of biomedical applications—quite high close to the needle tip. Nevertheless, it will also drop quickly in the next few millimeters. The gas temperature is also an input to the problem (from experiment or 2d simulations) [30].

The model adjusts the gas species densities for gas temperature changes while maintaining constant pressure, assuming ideal gas law. Since the focus of interest is on the biomedically active components, often present at ppm levels or even lower, a very large chemistry set has to be taken into account. However, at some point a decision has to be made about which species should be included and which will be neglected [30].

2.4 Numerical solution of global models– LSODA

The solution of the global model at transient state entails the numerical solution of a system of ordinary differential equations (ODEs). The total number of the equations is the number of mass balances (or the number of species joining the reaction set) plus

one which is the energy balance. The necessity of efficient numerical methods for differential equations arises. In this work, an efficient solver for stiff problems, namely LSODA (Livermore Solver for Ordinary Differential equations Automatic) [42], is utilized for the numerical solution of the system of ODEs coming from the global model equations.

Before discussing the capabilities of the LSODA solver, a short description of the different numerical methods for the solution of ODEs can be very useful, from the simplest to the more advanced. This analysis makes the comparison among the different methods more obvious, and their advantages and disadvantages become clear.

The methods described in this section solve numerically the initial value problem:

$$y'(t) = f\big(t, y(t)\big) \quad , \quad y(t_0) = y_0 \ (Eq. 2.26)$$

Despite the fact that this is only a first order ordinary differential equation, any ODE of order N can be represented as a system of first-order ODEs (see Appendix A). In the following paragraphs, a series of methods is presented, their stability is discussed, and finally LSODA is described and applied in test problems.

2.4.1 Euler method [43]

The simplest method for the solution of ODEs is the Euler method. A value for the step size h is chosen for every step and $t_n = t_0 + nh$ is set. The method assumes that $y'(t_n) = (y_{n+1} - y_n)/h$ and the method proceeds with $y_{n+1} = y_n + hf(t_n, y_n)$. The value of y_n is an approximation of the solution to the ODE at time t_n: $y_n \approx y(t_n)$ [44].

There are two categories of numerical methods for ODEs, the explicit and the implicit methods. Explicit methods calculate the state of a system at a later time from the state of the system at the current time, while implicit methods find a solution by solving an equation involving both the current state of the system and the later one. An implicit version of the Euler method is $y_{n+1} = y_n + hf\big(t_{n+1}, y(t_{n+1})\big)$. Implicit methods require an extra computation (solving the equation), and they can be much harder to implement. An important characteristic of a numerical method is the error in respect of the exact solution. The local truncation error of the Euler method is the error made in a single step. It is the difference between the numerical solution after one step, y_1, and the exact solution at time $t_1 = t_0 + h$. The local truncation error of the Euler method is approximately proportional to h^2 (for small h). The global truncation error is the error at a fixed time t, after however many steps the methods needs to take to reach that time from the initial time. The global truncation error is the cumulative effect of the local truncation errors committed in each step. The global truncation error of the Euler method is (approximately) proportional to h (this is why it is said to be a first order method). As a result, the Euler method is not an accurate method when compared with other methods of higher order, where the global truncation error is proportional to a higher power of the time step, h [45]. There are two main reasons why Euler method is not generally used in scientific computing. Firstly, the truncation error per step associated with this method is far larger than those associated with other, more advanced methods (for a given value of h). Secondly, Euler method is too prone to numerical instabilities (see section 2.4.4).

2.4.2 Runge-Kutta methods [46, 47]

The main reason that Euler method has such a large truncation error per step is that in evolving the solution from t_n to t_{n+1} the method only evaluates derivatives at the beginning of the interval, i.e. at t_n. The method is, therefore, very asymmetric with respect to the beginning and the end of the interval. A more symmetric integration method can be constructed by making an Euler-like trial step to the midpoint of the interval, and then using the values of both t and y at the midpoint to make the real step across the interval. To be more exact,

$$k_1 = hf\left(t_{n,}y_n\right) \ (Eq.\ 2.27)$$

$$k_2 = hf\left(t_n + \frac{h}{2}, y_n + \frac{k_1}{2}\right) \ (Eq.\ 2.28)$$

$$y_{n+1} = y_n + k_2 + O(h^3) \ (Eq.\ 2.29)$$

As indicated in the error term, this symmetrization cancels out the first-order error, making the method second-order. In fact, the above method is generally known as a second-order Runge-Kutta method. Euler method can be thought of as a first-order Runge-Kutta method. By using two trial steps per interval, it is possible to cancel out both the first and second-order error terms, and, thereby, construct a third-order Runge-Kutta method. Likewise, three trial steps per interval yield a fourth-order method, and so on. As the order of the method further increases there is a point where the accuracy benefits due to the large order are more than offset by the computational cost involved in the necessary additional evaluation of $f(t, y)$ per step. In most situations of interest a fourth-order Runge-Kutta integration method represents an appropriate compromise between the competing requirements of a low truncation error per step and a low computational cost per step [48, 49]. The standard fourth-order Runge-Kutta (RK4) method takes the form:

$$y_{n+1} = y_n + \frac{h}{6}(k_1 + 2k_2 + 2k_3 + k_4) \ (Eq.\ 2.30)$$

$$t_{n+1} = t_n + h \ (Eq.\ 2.31)$$

$$k_1 = f(t_n, y_n) \ (Eq.\ 2.32)$$

$$k_2 = f\left(t_n + \frac{h}{2}, y_n + \frac{h}{2}k_1\right) \ (Eq.\ 2.33)$$

$$k_3 = f\left(t_n + \frac{h}{2}, y_n + \frac{h}{2}k_2\right) \ (Eq.\ 2.34)$$

$$k_4 = f(t_n + h, y_n + hk_3) \ (Eq.\ 2.35)$$

Here, y_{n+1} is the RK4 approximation of $y(t_{n+1})$, and the next value (y_{n+1}) is determined by the present value (y_n) plus the weighted average of four increments, where each increment is the product of the size of the interval, h, and an estimated slope specified by function f on the right-hand side of the differential equation. k_1 is the increment based on the slope at the beginning of the interval using y (Euler), k_2 is the increment based on the slope at the midpoint of the interval, using $y + hk_1/2$, k_3 is again the increment based on the slope at the midpoint, but now using $y + hk_2/2$, k_4 is the increment based on the slope at the end of the interval, using $y + hk_3$. In averaging the four increments, greater weight is given to the increments at the midpoint. The RK4

method is a fourth-order method, meaning that the local truncation error is on the order of O(h^5), while the total accumulated error is order O(h^4) (see Appendix A).

2.4.3 Linear multistep methods [44]

As discussed, a numerical method starts from an initial point and then takes a short step forward in time to find the next solution point. The process continues with subsequent steps to map out the solution. Single-step methods (such as Euler's method) refer to only one previous point and its derivative to determine the current value. Methods such as Runge–Kutta take some intermediate steps (for example, a half-step) to obtain a higher order method, but then discard all previous information before taking a second step. Multistep methods attempt to gain efficiency by keeping and using the information from previous steps rather than discarding it. Consequently, multistep methods refer to several previous points and derivative values. In the case of linear multistep methods, a linear combination of the previous points and derivative values is used. In particular, a linear multistep method uses a linear combination of y_i and $f(t_i, y_i)$ to calculate the value of y for the desired current step. Thus, a linear multistep method is a method of the form:

$$y_{n+s} + a_{s-1}y_{n+s-1} + a_{s-2}y_{n+s-2} + \cdots + a_0 y_n = h\big(b_s f(t_{n+s}, y_{n+s}) + b_{s-1} f(t_{n+s-1}, y_{n+s-1}) + \cdots + b_0 f(t_n, y_n)\big) \quad (Eq. 2.36)$$

The coefficients a_0, ..., a_{s-1} and b_0, ..., b_s determine the method. The designer of the method chooses the coefficients, balancing the need to get a good approximation to the true solution against the desire to get a method that is easy to apply. Often, many coefficients are zero to simplify the method. If $b_s = 0$, then the method is explicit, since the formula can directly compute y_{n+s}. If $b_s \neq 0$, then the method is implicit, since the value of y_{n+s} depends on the value of $f(t_{n+s}, y_{n+s})$, and the equation must be solved for y_{n+s}. Iterative methods such as Newton's method are often used to solve the implicit formula. Three families of linear multistep methods are commonly used: Adams–Bashforth methods, Adams–Moulton methods, and the backward differentiation formulas (BDFs).

The Adams–Bashforth methods are explicit methods. The coefficients are $a_{s-1} = -1$ and $a_{s-2} = ... = a_0 = 0$, while the b_j are chosen such that the methods have order s (this determines the methods uniquely) [43].

The Adams–Bashforth methods with $s = 2$ is:

$$y_{n+2} = y_{n+1} + h\left(\frac{3}{2} f(t_{n+1}, y_{n+1}) - \frac{1}{2} f(t_n, y_n)\right) \quad (Eq. 2.37)$$

The coefficients b_j can be determined by using polynomial interpolation to find the polynomial p of degree $s-1$ such that $p(t_{n+i}) = f(t_{n+i}, y_{n+i})$ for $i = 0, \ldots, s-1$ (see Appendix A).

The Adams–Moulton methods are similar to the Adams–Bashforth methods in that they also have $a_{s-1} = -1$ and $a_{s-2} = ... = a_0 = 0$. Again the b coefficients are chosen to obtain the highest order possible. However, the Adams–Moulton methods are implicit methods. By removing the restriction that $b_s = 0$, an s-step Adams–Moulton method can reach order $s+1$, while an s-step Adams–Bashforth methods has only order s. The Adams–Moulton method with $s = 2$ is [50] (see Appendix A):

$$y_{n+2} = y_{n+1} + h\left(\frac{5}{12}f(t_{n+2}, y_{n+2}) + \frac{2}{3}f(t_{n+1}, y_{n+1}) - \frac{1}{12}f(t_n, y_n)\right) \ (Eq. 2.38)$$

The BDF methods are implicit methods with $b_{s-1} = ... = b = 0$ and the other coefficients chosen such that the method attains order s (the maximum possible). The general formula for a BDF can be written as [51]:

$$\sum_{k=0}^{s} a_k y_{n+k} = h\beta f(t_{n+s}, y_{n+s}) \ (Eq. 2.39)$$

and for $s = 2$ is given by:

$$y_{n+2} - \frac{4}{3}y_{n+1} + \frac{1}{3}y_n = \frac{2}{3}hf\left(t_{n+2}, y_{n+2}\right) \ (Eq. 2.40)$$

2.4.4 Stability – Stiffness [52]

The Euler method (section 2.4.1) can be numerically unstable, meaning that the numerical solution grows very large for equations where the exact solution does not. This "difficult behavior" in the equation (which may not necessarily be complex itself) is described as stiffness, and is often caused by the presence of different time scales in the underlying problem, i.e. the equation includes some terms that can lead to rapid variation in the solution. This problem can be solved by making the step size, h, extremely small. Such an example is shown below:

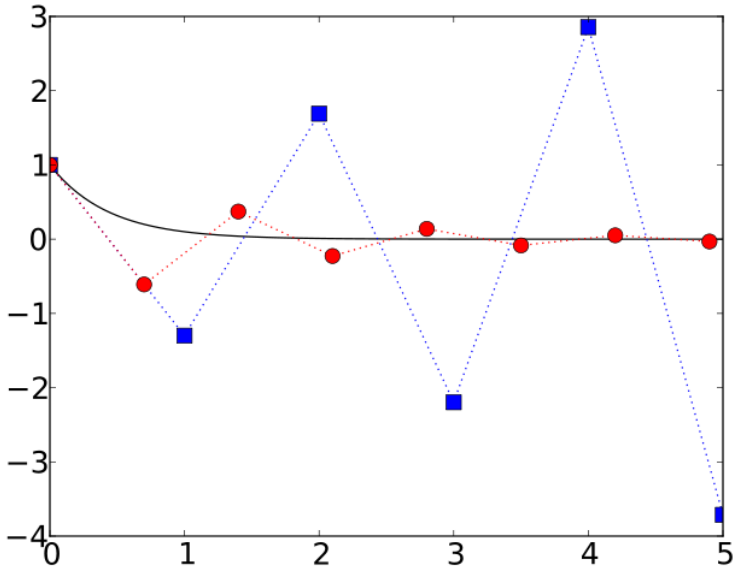

Figure 2.4: Solution of $y' = -2.3y$, $y(0) = 1$ with the Euler method, $h = 1$ (blue) and $h = 0.7$ (red). The black line is the exact solution [53].

As is evident in Figure 2.4, for some values of h ($h = 1$ in this example) the numerical solution oscillates and grows instead of decaying to zero, i.e. it is unstable. If a smaller step size is used, for instance $h = 0.7$, then the numerical solution does decay to zero. When integrating a differential equation numerically, one would expect the requisite step size to be relatively small in a region where the solution curve displays steep variation and to be relatively large where the solution curve straightens out to approach a line with slope nearly zero. For some problems this is not the case. Sometimes the

step size is forced down to an unacceptably small level in a region where the solution curve is very smooth. The phenomenon being exhibited here is known as stiffness. In some cases two different problems with the same solution may exist, yet problem one is not stiff and problem two is stiff. Clearly the phenomenon cannot be a property of the exact solution, since this is the same for both problems, and must be a property of the differential system itself. It is thus appropriate to speak of stiff systems (see Appendix A). It turns out not to be possible to give a strict definition of the stiffness phenomenon in a satisfactory manner, even for the restricted class of linear constant coefficient systems [52]. 'Phenomenon' is probably a more appropriate word than 'property', since the latter rather implies that stiffness can be defined in precise mathematical terms. Several qualitative statements that can be (and mostly have been) made in an attempt to encapsulate the notion of stiffness are [52]:

a) A linear constant coefficient system is stiff if all of its eigenvalues have negative real part and the stiffness ratio (Appendix A) is large.
b) Stiffness occurs when stability requirements, rather than those of accuracy, constrain the step length.
c) Stiffness occurs when some components of the solution decay much more rapidly than others.

The behavior of numerical methods on stiff problems can be analyzed by applying these methods to the test equation $y' = ky$ subject to the initial condition $y(0) = 1$ with $k\epsilon C$. The solution of this equation is $y(t) = e^{kt}$. This solution approaches zero as t approaches infinity when $Re(k) < 0$. If the numerical method also exhibits this behavior (for a fixed step size), then the method is said to be A-stable [54]. A-stable methods do not exhibit the instability problems. Runge–Kutta methods applied to the test equation $y' = ky$ take the form $y_{n+1} = \Phi(hk)y_n$, and, by induction, $y_n = \Phi^n(hk)y_0$. The function Φ is called the stability function. Thus, the condition that $y_n \to 0$ as $n \to \infty$ is equivalent to $|\Phi(hk)| < 1$. This motivates the definition of the region of absolute stability (sometimes referred to simply as stability region), which is the set $\{z\epsilon C|\ |\Phi(z)| < 1\}$. The method is A-stable if the region of absolute stability contains the set $\{z\epsilon C|\ Re(z) < 0\}$, that is, the left half plane. The Euler method has $\Phi(z) = 1 + z$ since $y_{n+1} = y_n + h(ky)$=> $y_{n+1} = (1 + hk)y_n$=> $y_n = (1 + hk)^n y_0$. The region of absolute stability for this method is thus $\{z\epsilon C|\ |1 + z| < 1\}$ which is the disk depicted in Figure 2.5. The Euler method is not A-stable.

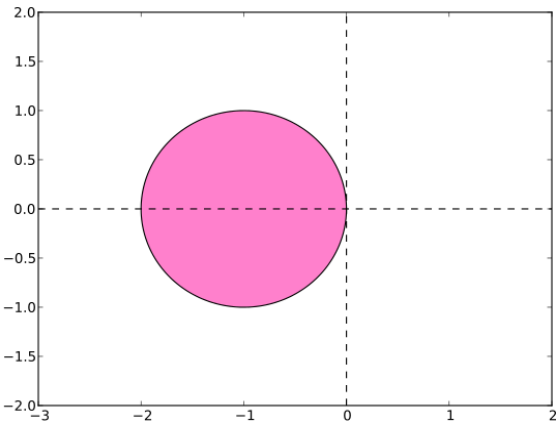

Figure 2.5: The pink disk shows the stability region for the Euler method [53].

In the example of Figure 2.4, $k = -2.3$, so if $h = 1$ then $hk = -2.3$, which is outside the stability region, and thus the numerical solution is unstable. If $h = 0.7$ then $z = -1.61$, which is inside the disk, and the numerical solution does decay to zero.

Regarding the Runge-Kutta methods, explicit Runge–Kutta methods are generally unsuitable for the solution of stiff equations because their region of absolute stability is small in contrast with the implicit Runge–Kutta methods. Explicit Runge–Kutta methods can never be A-stable [55] (see Appendix A).

Explicit multistep methods can never be A-stable, just like explicit Runge–Kutta methods (see Appendix A). The region of absolute stability for the two-step Adams–Bashforth method is shown in Figure 2.6. It does not include all the left half-plane (in fact it only includes the real axis between $z = -1$ and $z = 0$, so, it is not A-stable. Implicit multistep methods can only be A-stable if their order is at most two (second Dahlquist barrier) [54].

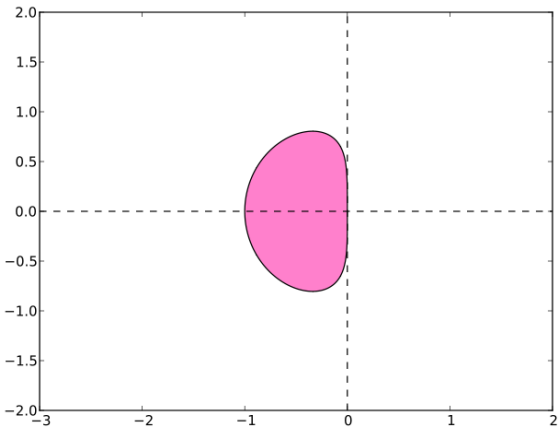

Figure 2.6: The pink region is the stability region for the second-order Adams–Bashforth method [53].

The BDF methods are the most efficient linear multistep methods and the stability region of the higher-order BDF methods contain a large part of the left half-plane and in particular the whole of the negative real axis [47]. In Figure 2.7, the absolute stability region of BDF methods with different orders is shown.

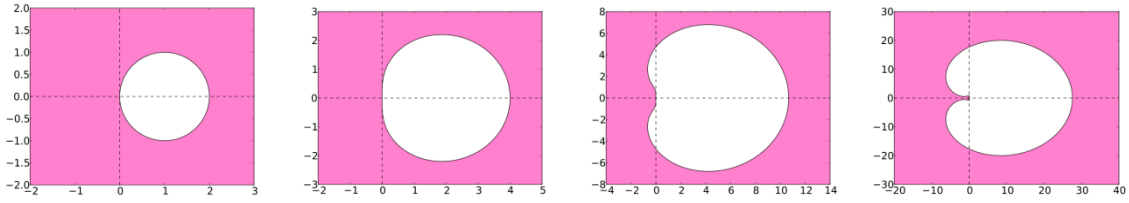

Figure 2.7: The absolute stability regions of BDF methods with order 1,2,4,6 (from left to right) [53].

2.4.5 LSODA solver

LSODA solves the initial value problem for stiff or non-stiff systems of first order ODEs and it is a variant of LSODE with the additional capability of recognizing if the system of equations is stiff or non-stiff. This means that the user does not have to determine whether the problem is stiff or not, and the solver will automatically choose the appropriate method. It always starts with the non-stiff method (less complexity-greater efficiency).

The non-stiff method used in LSODA is the Adams-Moulton linear multistep method up to twelfth order. For stiff problems it uses the BDF up to fifth order. During the integration it increases the order (and the step size) for maximum efficiency. If problems of instability arise, it changes the method to first order BDF while gradually increasing the order to the maximum value (five) or until instability occurs. When using the BDF method, LSODA makes tests in order to consider the switch back to Adams method (if

instability issues are resolved) for maximum efficiency. Periodically, LSODA evaluates the step size for the different methods and chooses the method with the best step size for the specified level of accuracy. All the methods in LSODA are implicit and as a result a modified Newton method is used to solve the nonlinear algebraic system of equations.

Apart from the absolute and relative tolerances defined by the user, LSODA provides many more options for the integrator and the solver. For example, the user can choose the type of the Jacobian matrix such as a user supplied full Jacobian (for better efficiency), an internally generated (difference quotient) full Jacobian, a user-supplied banded Jacobian and an internally generated banded Jacobian. The user can also define the step size to be attempted on the first step (the default value is determined by the solver), the maximum absolute step size allowed, the minimum absolute step size allowed, the maximum number of (internally defined) steps allowed during one call to the solver, the maximum order to be allowed for the non-stiff (Adams) method, the maximum order to be allowed for the stiff (BDF) method [42, 56].

LSODA was compiled and tested in stiff systems. An example of a stiff system is the following:

$$\frac{dy_1}{dt} = -0.04 * y_1 + 10^4 * y_2 * y_3 \ (Eq. 2.41)$$

$$\frac{dy_2}{dt} = -\left(\frac{dy_1}{dt} + \frac{dy_3}{dt}\right) \ (Eq. 2.42)$$

$$\frac{dy_3}{dt} = 3 * 10^7 * {y_2}^2 \ (Eq. 2.43)$$

$$y_1(0) = 1, y_2(0) = 0, y_3(0) = 0 \ (Eq. 2.44)$$

The functions required to run LSODA in this case are described below:

```
// definition of the system of equations
static void fex(double t, double *y, double *ydot, void *data)
{
	ydot[0] = 1.0E4 * y[1] * y[2] - .04E0 * y[0];
	ydot[2] = 3.0E7 * y[1] * y[1];
	ydot[1] = -1.0 * (ydot[0] + ydot[2]);
}

// driver to run the solver; define initial conditions, solver parameters and call solver
int main(void)
{
	double	rwork1, rwork5, rwork6, rwork7;
	double	atol[4], rtol[4], t, tout, y[4];
	int	iwork1, iwork2, iwork5, iwork6, iwork7, iwork8, iwork9;
	int	neq = 3;
	int	itol, itask, istate, iopt, jt, iout;

	iwork1 = iwork2 = iwork5 = iwork6 = iwork7 = iwork8 = iwork9 = 0;
	rwork1 = rwork5 = rwork6 = rwork7 = 0.0;
	y[1] = 1.0E0;
	y[2] = 0.0E0;
	y[3] = 0.0E0;
	t = 0.0E0;
	tout = 0.4E0;
	itol = 2;
```

```
        rtol[0] = 0.0;
        atol[0] = 0.0;
        rtol[1] = rtol[3] = 1.0E-8;
        rtol[2] = 1.0E-8;
        atol[1] = 1.0E-8;
        atol[2] = 1.0E-8;
        atol[3] = 1.0E-8;
        itask = 1;
        istate = 1;
        iopt = 0;
        jt = 2;

        for (iout = 1; iout<= 12; iout++) {
                lsoda(fex, neq, y, &t, tout, itol, rtol, atol, itask, &istate, iopt, jt,
                    iwork1, iwork2, iwork5, iwork6, iwork7, iwork8, iwork9,
                    rwork1, rwork5, rwork6, rwork7, 0);
                printf(" at t= %12.4e y= %14.6e %14.6e %14.6e\n", t, y[1], y[2], y[3]);
                if (istate<= 0) {
                        printf("error istate = %d\n", istate);
                        exit(0);
                }
                tout = tout * 10.0E0;
        }
        n_lsoda_terminate();

        return 0;
}
```

The same problem was solved with the Euler method. A simple program (in C) was written for this purpose and is shown below:

```
main()
{
double t,h,y1,y2,y3,y1d,y2d,y3d;
   h=0.0001;
   y1=1;
   y2=0;
   y3=0;
   t=0;
printf(" at t= %E y= %E %E %E\n", t, y1, y2, y3);

for (t=0.0001; t<=4e10; t=t+h)
{
      y1d=1.0E4*y2*y3-0.04*y1;
      y3d=3.0E7*y2*y2;
      y2d=-(y1d+y3d);
      y1=y1+h*y1d;
      y2=y2+h*y2d;
      y3=y3+h*y3d;
printf(" at t= %E y= %E %E %E\n", t-0.0001, y1, y2, y3);
}
```

The results returned from LSODA and from the Euler method ($h = 0.0001$) are shown in Figure 2.8. The solutions of both methods are very close. The execution time for the LSODA solver is 0.016 s, reaching $t = 4 * 10^{10}$ and for the Euler method ($h = 0.0001$) is

7052.6 s, reaching $t = 4 * 10^7$ (Pentium dual core E5200 @ 2.5 Ghz, RAM 4GB, 32 bit Win7).

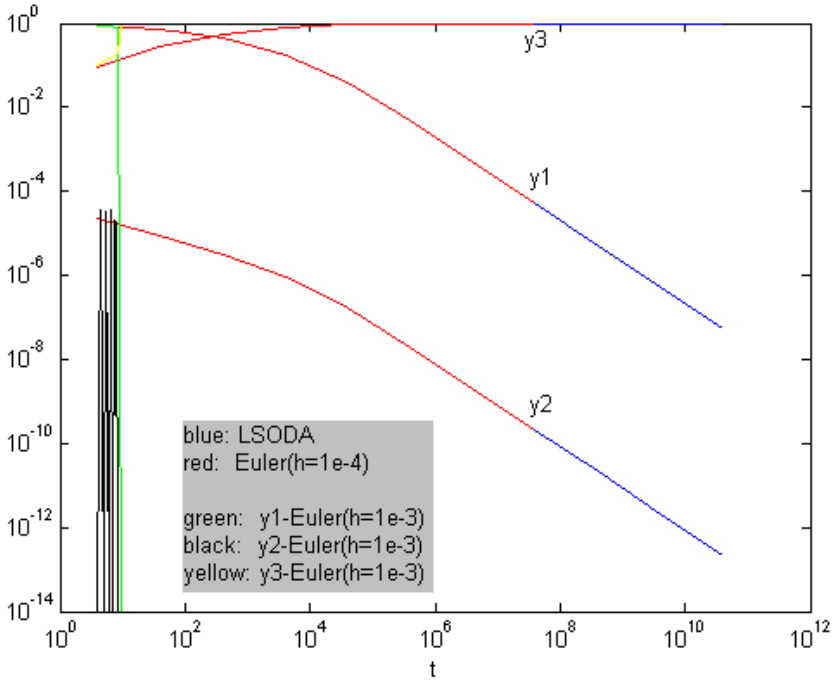

Figure 2.8: Results returned from LSODA (blue lines) and the Euler method (red lines) for the stiff system of Eqs.2.39-2.42. Results from the Euler method with $h = 0.001$ are also shown.

The solution obtained from the Euler method ($h = 0.0001$) reached only $t = 4 * 10^7$ because after this value the solution process became extremely slow.Even with a step size of $h = 0.001$, the Euler method led the solution to strong oscillations resulting in huge values and no convergence (typical stiff behavior) while trying to solve the stiff system (Figure 2.8). By making the step size $h = 0.0001$, the oscillations were almost eliminated and a solution was obtained. This example designates the efficiency of LSODA at solving stiff systems.

3. RESULTS

3.1 Introduction

The focus of this chapter is on the comparison of the results produced by the extended global model (πlasma-R) with the results from the work of Gaens&Bogaerts [30]. Firstly, the type and geometry of the device are described as well as the operating parameters of the simulation. Then, a very important aspect of the simulation, the electron energy distribution function, is discussed, and interesting conclusions are extracted. Finally, the simulation results are compared with the results of the work of Gaens&Bogaerts and the possible origin of the deviations is discussed.

3.2 Conditions and inputs

3.2.1 The device and the operating parameters

The plasma jet device simulated by the global model is shown in Figure 3.1 [24, 35].

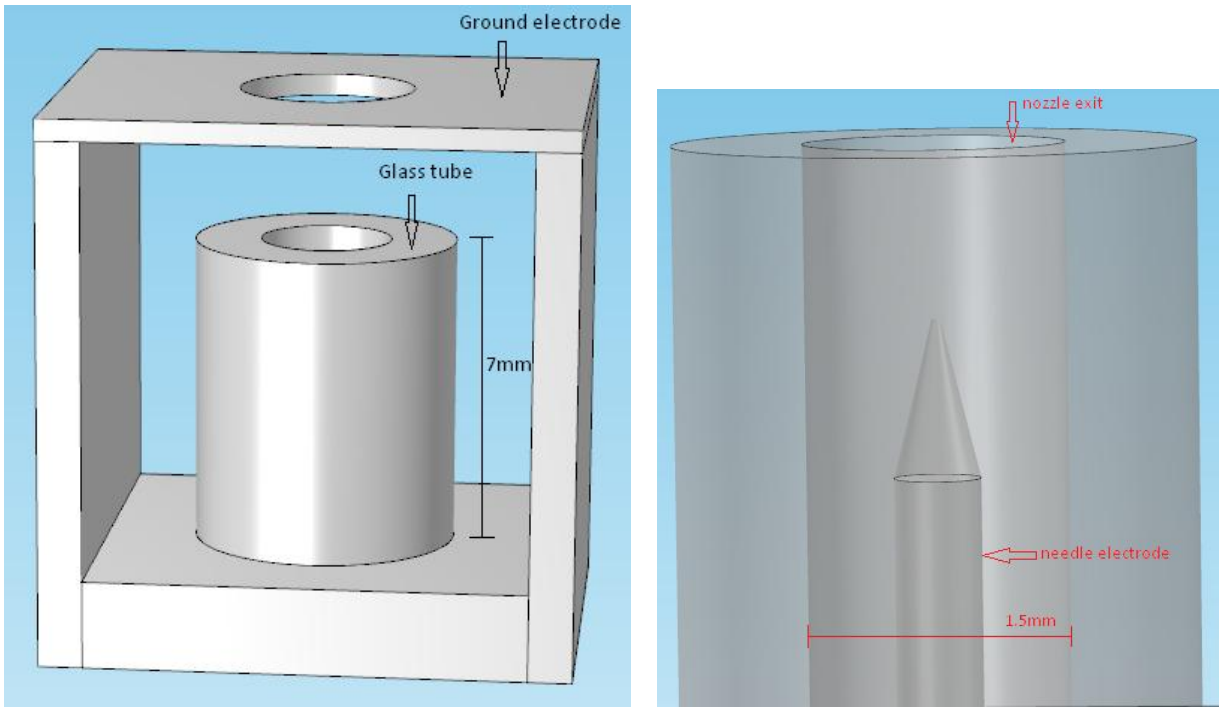

Figure 3.1: Geometry of the simulated plasma jet device (left: the whole device, right: zoom inside the glass tube).

The plasma source consists of an RF-driven tungsten needle with a diameter of 1mm and a sharpened tip surrounded by a glass tube with a 3mm outer and a 1.5mm inner diameter. A gas flow of Argon (Ar) is applied through the tube. The gas flow is kept constant at 2 slm. The air impurities in the gas feed are 10ppm for N_2/O_2 and 1 ppm for H_2O. The setup is not in a vacuum vessel and thus it is open to air. A grounded copper electrode is positioned at a distance of 5mm from the needle. It has a hole with a diameter of 5mm through which the plasma can pass. The plasma jet is a so-called linear field plasma jet [3], since the electrical field and the gas flow have the same direction.

The tube of the plasma jet device, the plasma jet itself and the afterglow region in the far effluent are assumed to be represented by a long cylinder (Figure 3.2), where

constant atmospheric pressure conditions rule. The diameter of this cylinder is 1.5 mm and within a segment of this cylinder only spatially averaged quantities (temperature, velocity, densities etc.) are considered.

Figure 3.2: The cylinder representation of the plasma jet device [30].

As in the work of Gaens&Bogaerts, inputs of the global model are (see Figure 2.3) the temperature, power density, and Ar, N_2, O_2, and H_2O densities, as a function of distance from the nozzle exit, as shown in Figure 3.3. All these data are coming from experimental measurements [30]. Analytic functions for Ar, N_2, O_2, and H_2O densities and gas temperature as a function of the distance from the nozzle exit were fitted to the pertinent experimental curves of Figure 3.3 (see Eqs. 3.1 – 3.6) to facilitate the numerical solution of the system of differential equations. The curves from both the analytic functions and the experimental measurements are shown in Figure 3.4.

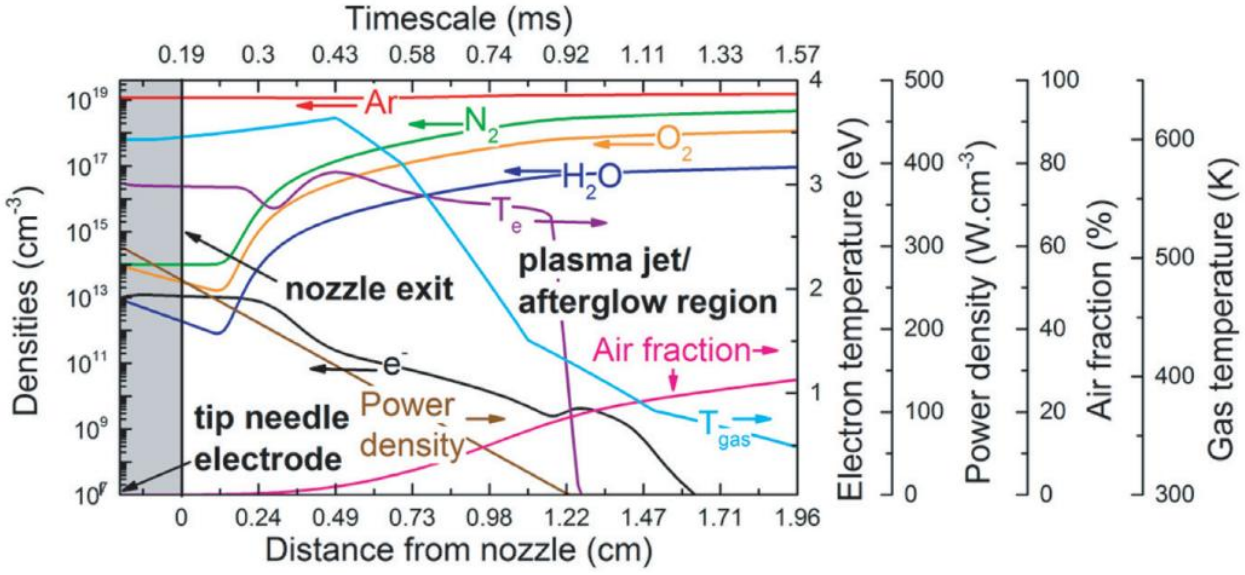

Figure 3.3: The inputs for the global model (Ar-N_2-O_2-H_2O densities, gas temperature and power density) [30]. The density and temperature of the electrons are calculated by the model.

$$[\mathrm{Ar}] = 10^{25}\ \mathrm{m}^{-3} \qquad (Eq.3.1)$$

$$\log([\mathrm{N_2}]) = 9.362\mathrm{e}^{\left(-\left(\frac{x-0.01351}{0.003243}\right)^2\right)} + 5.295\mathrm{e}^{\left(-\left(\frac{x-0.08249}{0.002664}\right)^2\right)} + 2.627\mathrm{e}^{\left(-\left(\frac{x-0.005193}{0.001847}\right)^2\right)} + 1.64\mathrm{e}^{\left(-\left(\frac{x-0.003474}{0.001234}\right)^2\right)} + 0.8351\mathrm{e}^{\left(-\left(\frac{x-0.002385}{0.0007885}\right)^2\right)} + 1.253\mathrm{e}^{\left(-\left(\frac{x-0.01059}{0.001565}\right)^2\right)} - 12.86\mathrm{e}^{\left(-\left(\frac{x-0.001472}{0.00000585}\right)^2\right)} + 20.02\mathrm{e}^{\left(-\left(\frac{x+0.0009563}{0.02589}\right)^2\right)}\ \mathrm{m}^{-3} \qquad (Eq.3.2)$$

$$\log([O_2]) = 23.670e^{\left(-\left(\frac{x-0.01388}{0.01308}\right)^2\right)} + 4.32e^{\left(-\left(\frac{x-0.00548}{0.004221}\right)^2\right)} + 1.232e^{\left(-\left(\frac{x-0.00434}{0.001922}\right)^2\right)} + 0.9318e^{\left(-\left(\frac{x-0.003325}{0.001139}\right)^2\right)} + 0.6566e^{\left(-\left(\frac{x-0.002054}{0.0006362}\right)^2\right)} + 15.13e^{\left(-\left(\frac{x+0.003678}{0.005583}\right)^2\right)} + 0.6742e^{\left(-\left(\frac{x-0.002658}{0.0007907}\right)^2\right)} + 0.6104e^{\left(-\left(\frac{x-0.0004676}{0.001339}\right)^2\right)} \text{ m}^{-3} \qquad (Eq.\ 3.3)$$

$(-0.193 \leq x < -0.000592 \text{ cm})$:

$$\log([H_2O]) = 21.71e^{\left(-\left(\frac{x+0.01167}{0.026}\right)^2\right)} + 0.4932e^{\left(-\left(\frac{x-0.00031}{0.001636}\right)^2\right)} \text{ m}^{-3} \qquad (Eq.\ 3.4)$$

$(-0.000592 \leq x < 0.013 \text{ cm})$:

$$\log([H_2O]) = 16.40e^{\left(-\left(\frac{x-0.01579}{0.002617}\right)^2\right)} + 20.23e^{\left(-\left(\frac{x-0.008339}{0.004316}\right)^2\right)} + 5.921e^{\left(-\left(\frac{x-0.004844}{0.002261}\right)^2\right)} + 1.82e^{\left(-\left(\frac{x-0.003867}{0.001132}\right)^2\right)} + 0.69e^{\left(-\left(\frac{x-0.003313}{0.00071}\right)^2\right)} + 2.873e^{\left(-\left(\frac{x-0.002376}{0.00098}\right)^2\right)} + 11.38e^{\left(-\left(\frac{x-0.01263}{0.002825}\right)^2\right)} + 17.98e^{\left(-\left(\frac{x+0.00048}{0.004371}\right)^2\right)} \text{ m}^{-3} \qquad (Eq.\ 3.5)$$

$$\log([T_g]) = 105.6e^{\left(-\left(\frac{x-0.005689}{0.003792}\right)^2\right)} - 6.276e^{\left(-\left(\frac{x-0.006031}{0.00067}\right)^2\right)} + 20.14e^{\left(-\left(\frac{x-0.00085}{0.002432}\right)^2\right)} - 11.24e^{\left(-\left(\frac{x-0.01107}{0.00085}\right)^2\right)} + 654.3e^{\left(-\left(\frac{x+0.01392}{0.03835}\right)^2\right)} \text{ K} \qquad (Eq.\ 3.6)$$

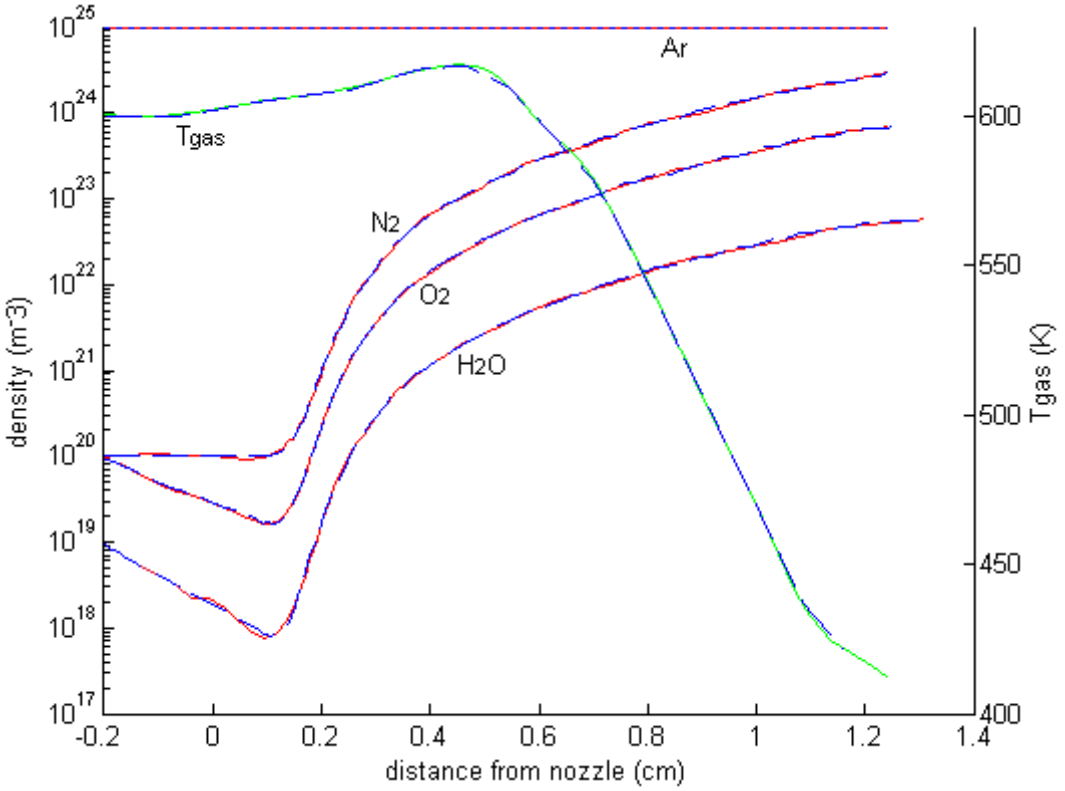

Figure 3.4: Densities of the species and gas temperature, which are used as input (red and green solid: data used in this work, blue dashed curved: experimental data used by Gaens&Bogaerts [30]).

The total deposited power is 6.5 W. The estimated power deposition density (Wm^{-3}) profile is assuming a maximum power density at the needle electrode tip at 2mm before

the nozzle exit, and the value decreases linearly along the plasma jet flow. To measure the power deposition profile further from the needle tip is highly non-trivial. We know, however, from the literature that plasma jets typically show UV–vis light emission over a distance in the order of maximum a few centimeters. In this case, light can be observed until 1.2 cm after the nozzle exit (Fig. 3.2). Since calculations predict that the electron density and excited state densities rapidly drop when the power deposition becomes small, a power density profile that linearly goes to zero at 1.2 cm is adopted [30].

The global model is solved at transient state, thus the inputs are required as a function of time elapsed. The velocity profile, needed for the conversion from the time domain to the space domain and vice versa, is shown in Figure 3.5 [41]. An analytic function is also utilized to approximate the velocity curve (Eq. 3.7) and is also included in Figure 3.5.

$$u = \begin{cases} 27.775e^{-237.8x} & 0 \le x < 7.242e-5 \text{ m} \\ 27.654e^{-173.6x} & 7.242e-5 \le x < 0.00108 \text{ m} \\ 25.806e^{-109.4x} & 0.00108 \le x < 0.00247 \text{ m} \\ 22.913e^{-61.22x} & 0.00247 \le x < 0.00475 \text{ m} \\ 21.23e^{-44.12x} & 0.00475 \le x < 0.00875 \text{ m} \\ 24.882e^{-61.95x} & 0.00875 \le x < 0.01248 \text{ m} \end{cases} \quad \text{m/s} \quad (Eq.\,3.7)$$

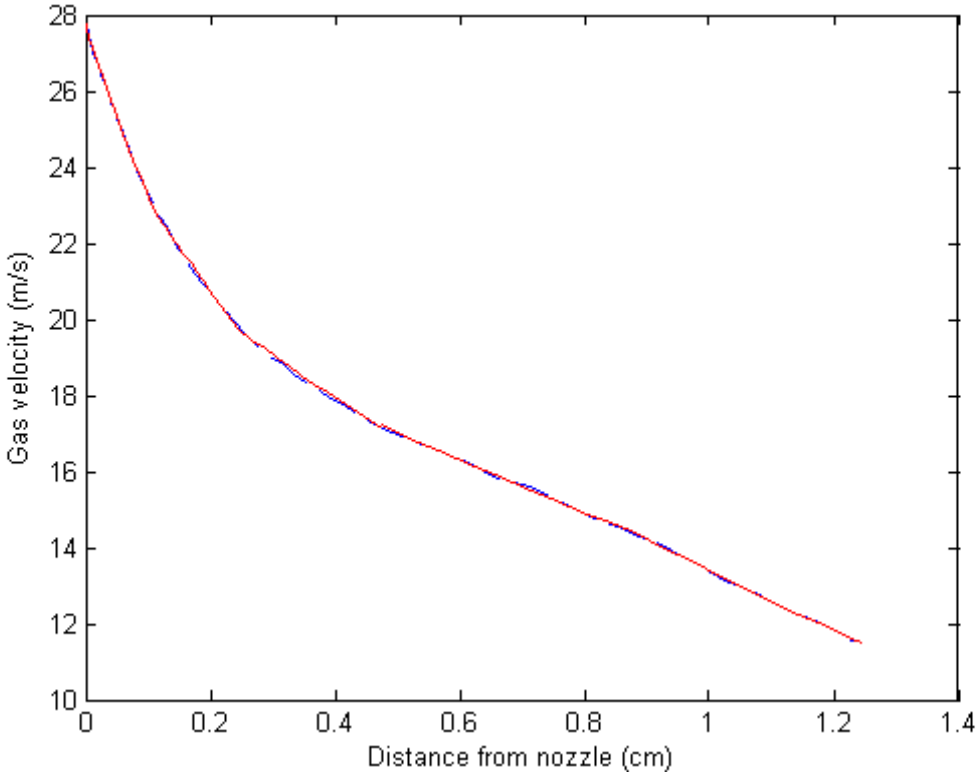

Figure 3.5: Gas velocity as a function of distance from nozzle (red solid: velocity in this work, blue dashed: velocity in the work of Gaens&Bogaerts [41]).

3.2.2 Reaction set

The reaction set consists of 846 reactions (reduced set from [30]) among 84 species. The species included in the model are: Ar, Ar($^4S^3P_2$), Ar($^4S^3P_1$), Ar($^4S^3P_0$), Ar($^4S^1P_1$), Ar(^4P), $Ar_2^*(\alpha^3\Sigma_u^+)$, Ar^+, Ar_2^+ ,ArH^+, N, N_2, N(^2D), $N_{2(rot)}$, $N_{2(vib1-8)}$, $N_2(A^3\Sigma_u^{\ 1})$, $N_2(\alpha'^1\Sigma_u^-)$, N^+, N_2^+, N_3^+, N_4^+, O, O_2, O_3, O(^1D), $O_{2(rot)}$, $O_{2(vib1-4)}$, $O_2(\alpha^1\Delta_g)$, $O_2(b^1\Sigma_g^+)$, O^+, O_2^+, O_4^+, O^-, O_2^-, O_3^-, NO, NO_2, N_2O, NO_3, N_2O_3, N_2O_4, N_2O_5, $N_2O_{(vib1-3)}$, NO^+, NO_2^+, NO_2^-, NO_3^-, H,

H_2, OH, H_2O, HO_2, H_2O_2, H^*, $H_{2(rot)}$, $H_{2(vib1\text{-}2)}$, H_2^*, $H2O_{(vib[100,010,001])}$, H^+, H_2^+, H_3^+, OH^+, H_2O^+, H_3O^+, NH, HNO, HNO_2, HNO_3, HNO_4, OH(A), H^-, OH^-, $H_4O_2^+$, $H_2O_3^+$, $H_5O_2^+$, $H_7O_3^+$,$H_9O_4^+$,$H_{11}O_5^+$,$H_{13}O_6^+$,$H_{15}O_7^+$, $H_2NO_2^+$, $H_4NO_3^+$, $H_6NO_4^+$.Species Ar(^{4}P) groups the electronically excited states ^{4}P, ^{5}D, ^{5}S and ^{5}P, species H^* groups the electronically excited states with n=2-4 and species H_2^* groups the electronically excited states ($b^3\Sigma_u^+$) and ($c^3\Pi_u$).

The reaction set is described in Table B1 of Appendix B. The rate coefficients of the reactions are taken from [30] except for the reactions (electron impact) for which it was not possible to find consistent information based on the references of [30]. The references for these reactions are also included in Table B1. M denotes third body.

3.2.3 The reaction coefficients and the electron energy distribution function

The calculation of the rate coefficients of the electron impact reactions (reactions from 1 to 163 in Table B1, Appendix B) requires the consideration of an electron energy distribution function. The rate coefficients for electron impact reactions read

$$k = \int_0^\infty \sqrt{\frac{2\varepsilon}{m_e}}\sigma(\varepsilon) f(\varepsilon, \bar{\varepsilon}) d\varepsilon \qquad (Eq. 3.8)$$

where m_e is the electron mass, ε is the electron energy, $\bar{\varepsilon}$ is the mean electron energy, $\sigma(\varepsilon)$ is the cross section for the specific reaction and $f(\varepsilon, \bar{\varepsilon})$ is the normalized electron energy distribution function (EEDF).

The options for the EEDF is to consider a predefined EEDF, such as Maxwellian or Druyvesteyn, or calculate the EEDF with a Boltzmann equation solver. Note that we need to calculate the EEDF and the pertinent rate coefficients at every time instance, given that the gas mixture composition and the gas temperature varies with time (see Figure 3.6). The latter requires a Boltzmann solver available for multiple successive calculations and entails a higher computational cost compared to considering a predefined EEDF. Gaens&Bogaerts use a look-up table of these coefficients as a function of a wide range of electron temperatures, constructed by an internal Boltzmann equation solver using electron collision cross sections. These look-up tables are regularly updated by running the Boltzmann code again (every 10μs with a modified Global_Kin code [33]), because of the drastic change in background gas composition due to humid air diffusion [30]. How important are the changes of the gas composition and temperature (see Figure 3.6) for the EEDF?

In order to study the impact of gas mixture composition and gas temperature on the EEDF, Bolsig+ [36] is used to solve the Boltzmann equation at specific time instances (t=0.19, 0.365, 0.58 and 0.74ms). The results are shown in Figure 3.7 and they also include comparison with the Maxwell and Druyvesteyn EEDFs of the same mean electron energy (4.5 eV). Each time instant corresponds to a different gas phase composition.

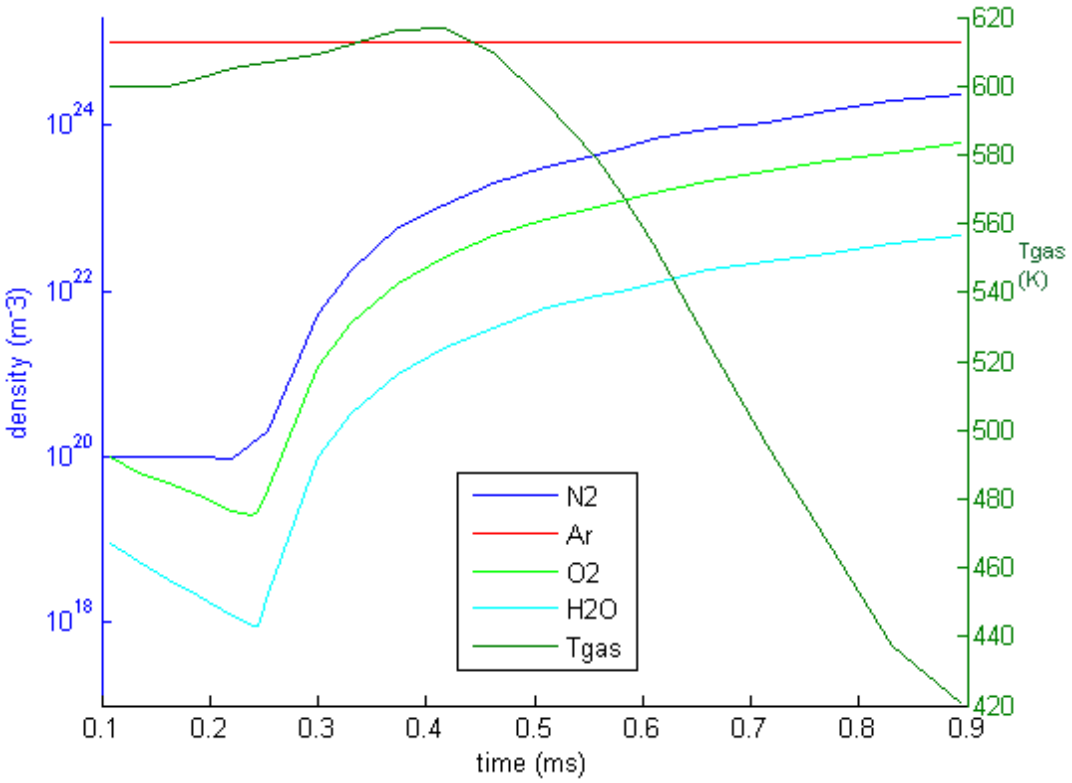

Figure 3.6: Gas temperature and densities of Argon and air as a function of time, coming from experimental measurements [30].

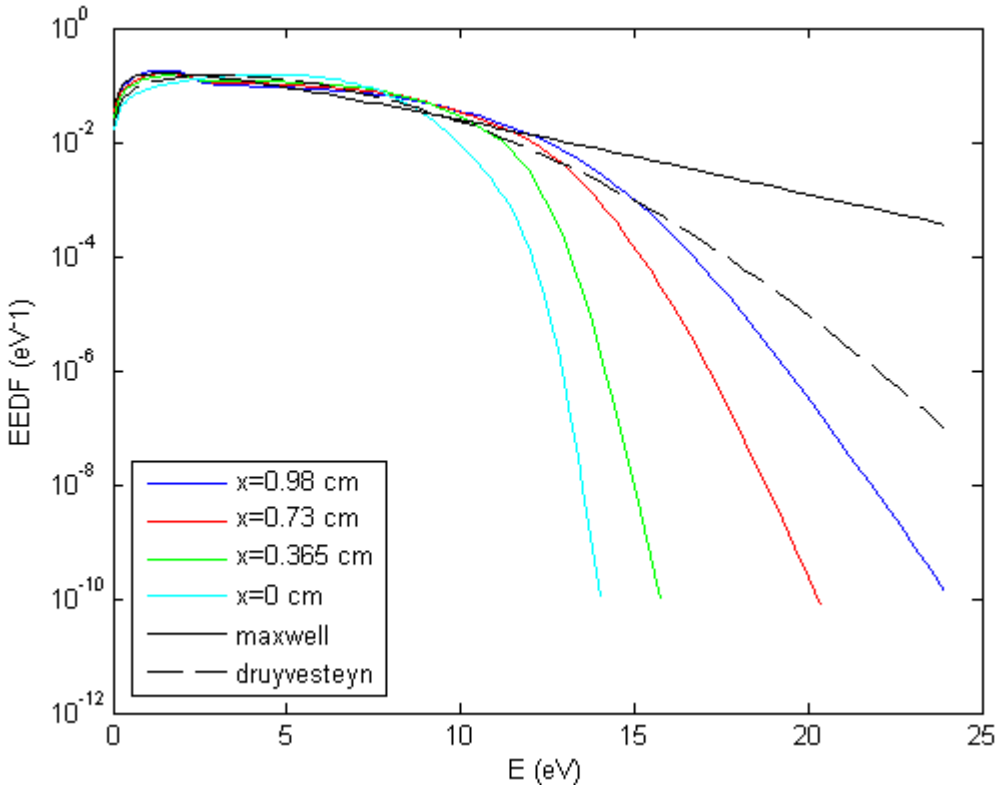

Figure 3.7: EEDFs for the gas mixture composition and gas temperature at
a) x=0 cm [mole fractions 0.9999(Ar),10^{-5}(N_2),$3x10^{-6}$(O_2),$2x10^{-7}$(H_2O),T_g=600K,E_m=4.5eV],
b) x=0.365 cm [0.9945(Ar),$4.47x10^{-3}$(N_2),$8.95x10^{-4}$(O_2),$7.96x10^{-5}$(H_2O),T_g=615K,E_m=4.5eV],
c) x=0.73cm [0.9399(Ar),4.710^{-2}(N_2),$1.22x10^{-2}$(O_2),$9.4x10^{-4}$(H_2O),T_g=567K,E_m=4.5eV],
d)x=0.98cm (0.8453(Ar),1.2710^{-1}(N_2),$2.54x10^{-2}$(O_2), $2.54x10^{-3}$(H_2O),T_g=478K,E_m=4.5eV],
as calculated by Bolsig+. Maxwell and Druyvesteyn EEDFs of the same mean electron energy (E_m = 4.5 eV) are also shown.

From Figure 3.7, it follows that the combined effect of the change of gas composition and gas temperature under the specific conditions of the simulation (Figure 3.6) is a drastic change of the calculated EEDF. The calculated EEDFs are consistent with the Maxwell and Druyvesteyn distributions for lower electron energies but there are discrepancies for higher values of the electron energy. The Druyvesteyn distribution is, generally, closer to the calculated EEDFs.

Apart from the specific conditions of the simulation, the EEDF was also calculated for different gas temperatures and mean electron energies. The mean energies of the electrons were selected in such a way that they cover a broad range of values commonly measured during plasma jet experiments. The two selected values of the gas temperature (400K and 600K) are also common in plasma jet experiments and are also distant enough so as to highlight the extent of the impact of the gas temperature on the EEDF. The results are shown in Figure 3.8.

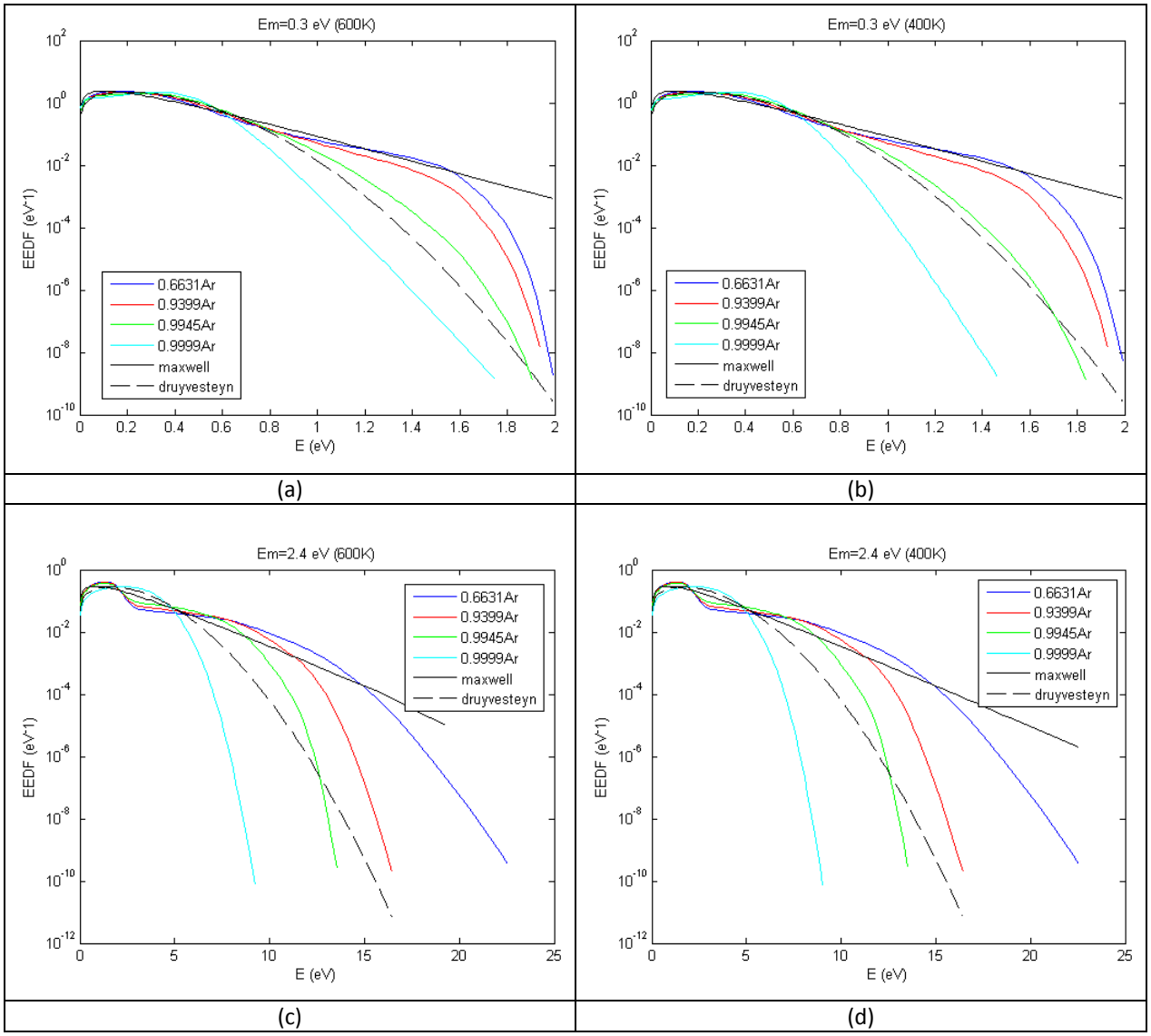

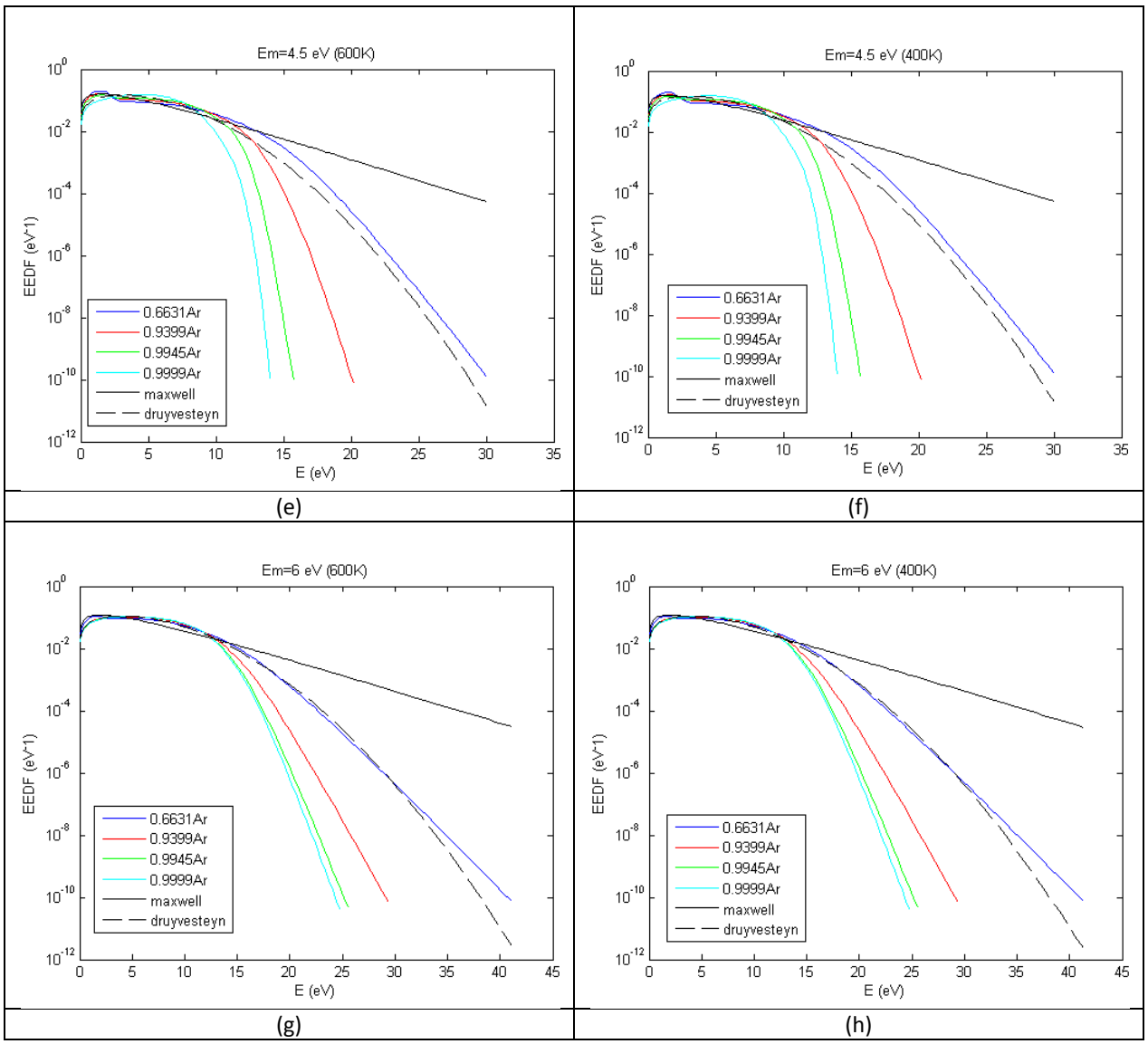

Figure 3.8: EEDFs for different values of the mean energy of the electrons (E_m).
The mole fractions of species are (blue curve) 0.663(Ar), 0.265(N_2), 0.066(O_2), 0.005(H_2O),
(red curve) 0.94(Ar), 0.047 (N_2), 0.012 (O_2), 0.00094 (H_2O),
(green curve) 0.995(Ar), 0.0045(N_2), 0.0009(O_2), 0.00008(H_2O),
(light blue curve) 0.999(Ar)/0.00001(N_2)/0.000003(O_2)/0.0000002(H_2O)

In an attempt to make more general conclusions by observing the graphs of Figure 3.8, which include EEDFs over a wider range of mean energy values and different gas temperatures (not only the ones employed for this simulation), one can say that (for Argon mixtures) generally, there are discrepancies between the calculated EEDFs and the Maxwell or Druyvesteyn distribution (for the same mean electron energies). The calculated EEDFs are more consistent with the Maxwell and Druyvesteyn distributions for lower electron energies. Furthermore, for higher mean electron energies, the EEDF becomes less sensitive to the gas composition and tends to move away from the Maxwell distribution. Finally, the gas temperature at the range of 400-600 K does not affect the calculated EEDFs except for very low mean electron energies with a higher Ar mole fraction. This is normal as the gas temperature is only important for very low E/N values (electric field/ gas density) where the electrons may gain energy in elastic collisions with gas particles [36].

Given that the gas mixture composition affects the EEDF and that the gas mixture composition varies with time (see Figure 3.6), the EEDF and the pertinent reaction rate coefficients (see Eq. 3.8) vary with time and should be updated frequently.

In this work, given that we cannot use Bolsig+ for the multiple (frequent) calculations of the EEDF (Bolsig+ comes with a GUI) at every time step, we consider two cases: In the first case we use a Maxwellian EEDF and in the second we calculate the EEDF by Bolsig+ at only three conditions (gas mixture composition and gas temperature corresponding to three distances from the nozzle or at three time instances) for practical reasons. In particular, EEDFs for different electron mean energies are calculated for the conditions at t=0.3, 0.42, and 0.74 ms (x=0.24, 0.47, and 0.98 cm); it is considered that the first set of EEDFs is representative of the time interval 0.11-0.3 ms, the second set of EEDFs is representative of the interval 0.3-0.58 ms, and the third set of EEDFs is representative of the time interval 0.58-0.90 ms. A gas mixture of the gases Ar, N_2, O_2 and H_2O is considered, with composition at distance *x* from the nozzle exit determined by the experimental data (Figure 3.4). The cross sections [30] of the reactions 1-163 of Table B1 and the electron energies (T_e) of Figure 3.3 are used for the calculations.

3.3 Simulation results and discussion

The results of the simulations are shown in Figures 3.9 and 3.10 which also include the results of Gaens&Bogaerts [30]. These graphs include the computed densities of the most important species (dashed curves represent the results of Gaens&Bogaerts) and the computed electron temperature. Two scenarios for the rate coefficients of electron impact reactions are considered: The first scenario is to use three equations (formulas) for the rate coefficients, each one corresponding to a different spatial region (-0.2-0.24cm, 0.24-0.73cm, 0.73-1.16cm) or a different time space (0.11-0.3ms, 0.3-0.58ms, 0.58-0.9ms). The rate coefficients at each region are coming from the integration of the pertinent cross section over the EEDF at the specific region, i.e. at the specific gas phase composition and gas temperature (see section 3.2). The second scenario is to use one equation for the rate coefficients coming from the integration of the pertinent cross section over a Maxwellian EEDF. The simulation results from the first scenario are shown in the left columns of Figures 3.9 and 3.10, while the simulation results from the second scenario are shown in the second columns.

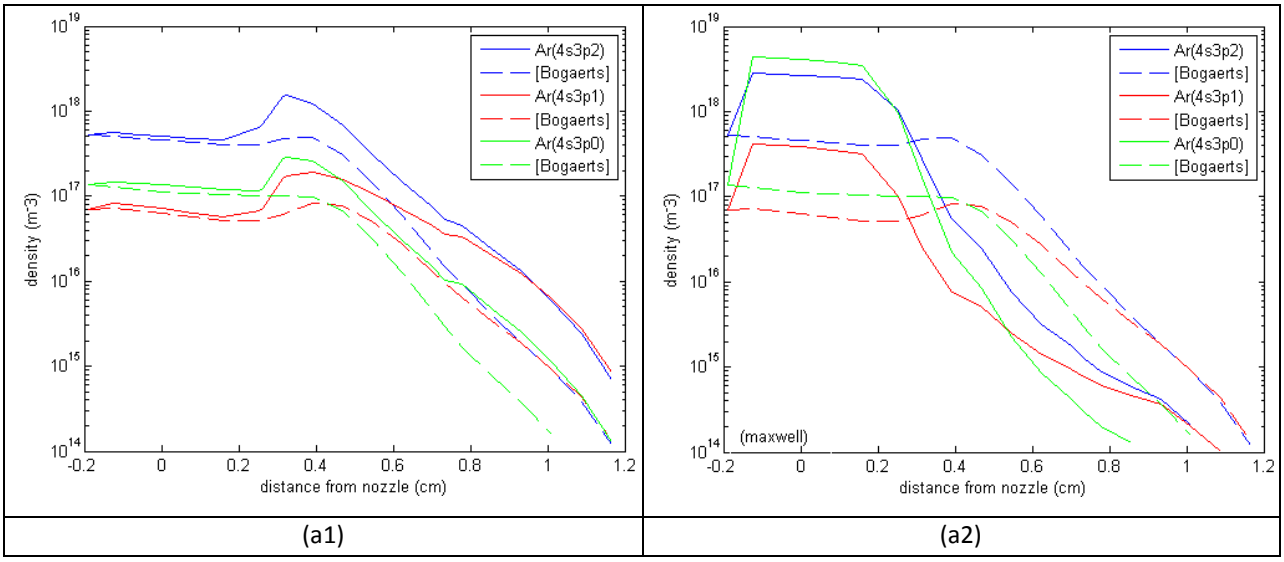

(a1) (a2)

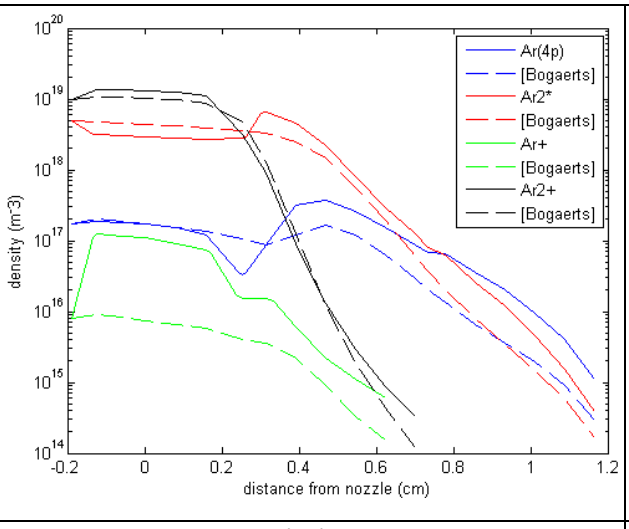

(b1)

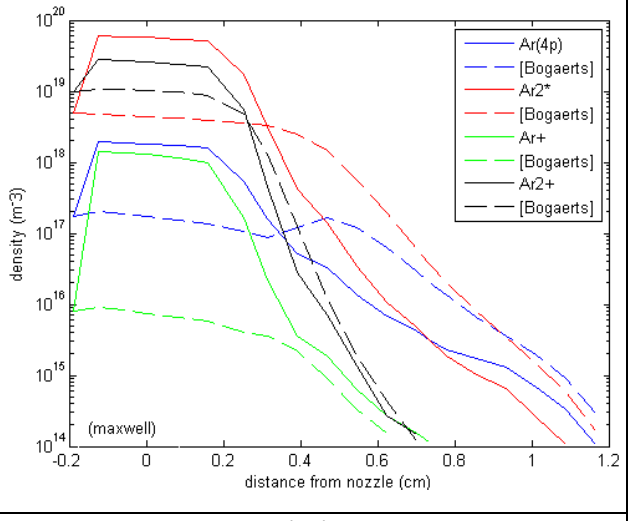

(b2)

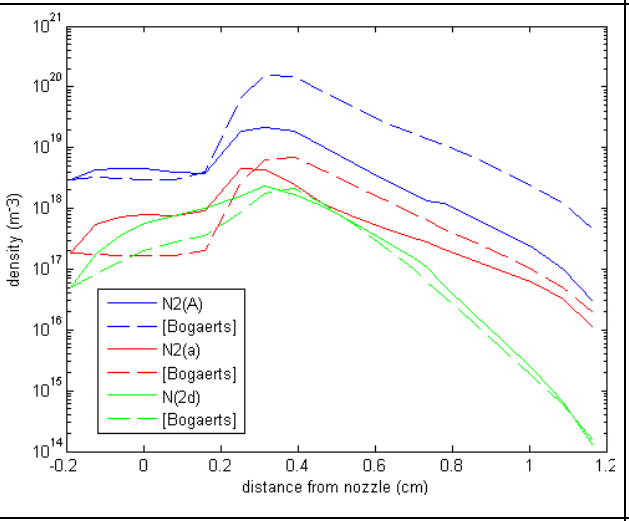

(c1)

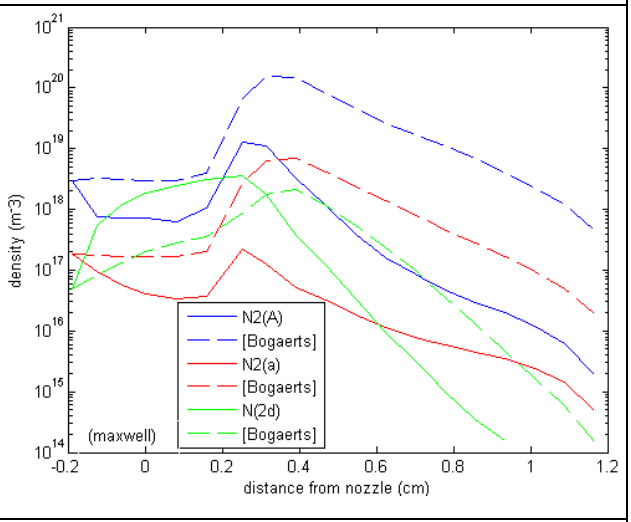

(c2)

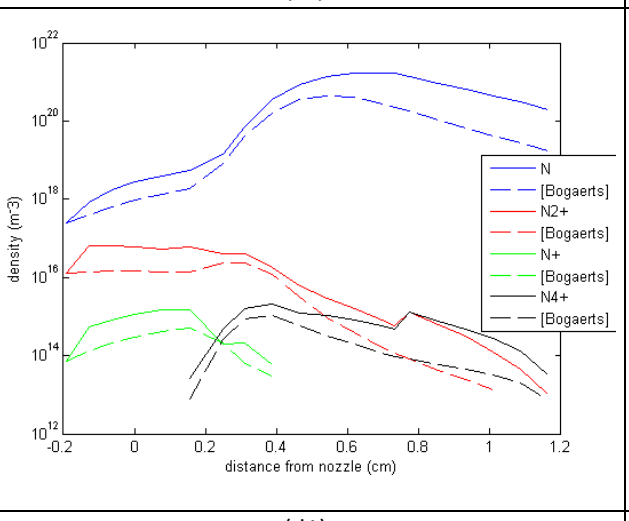

(d1)

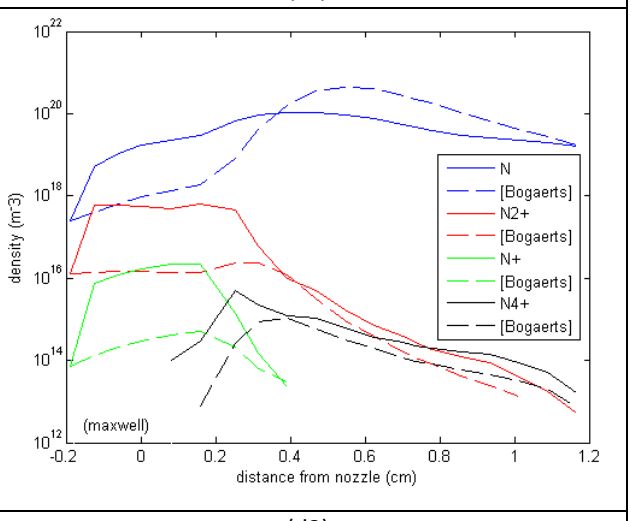

(d2)

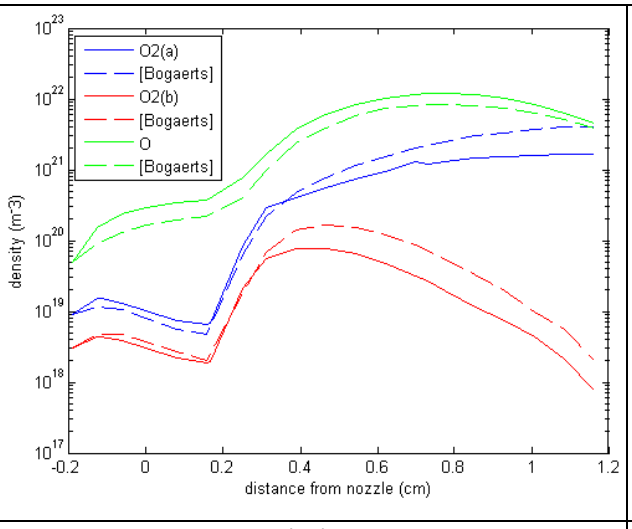

(e1)

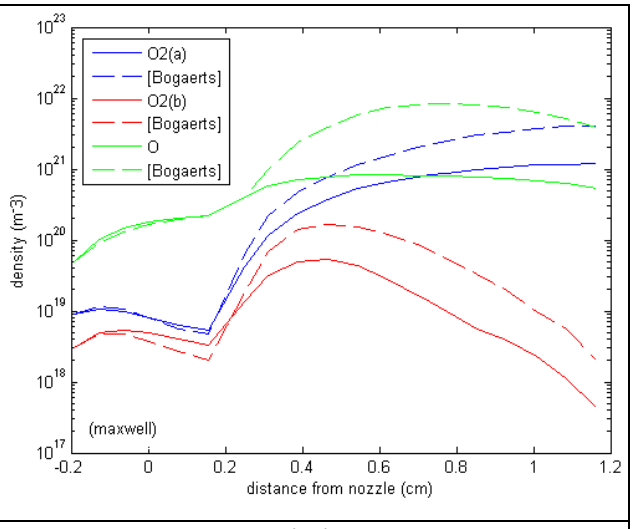

(e2)

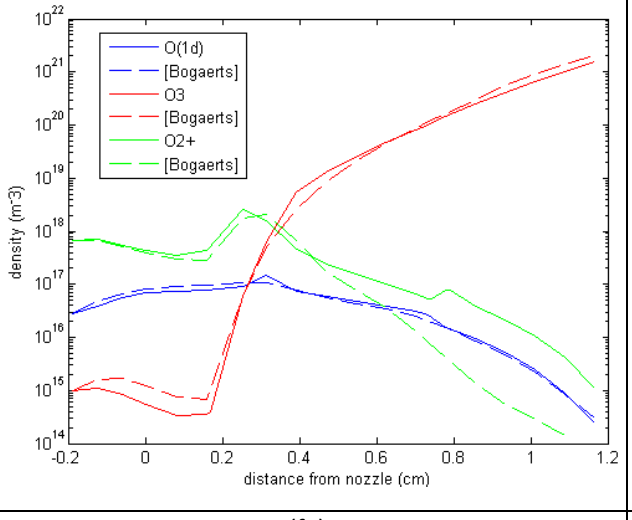

(f1)

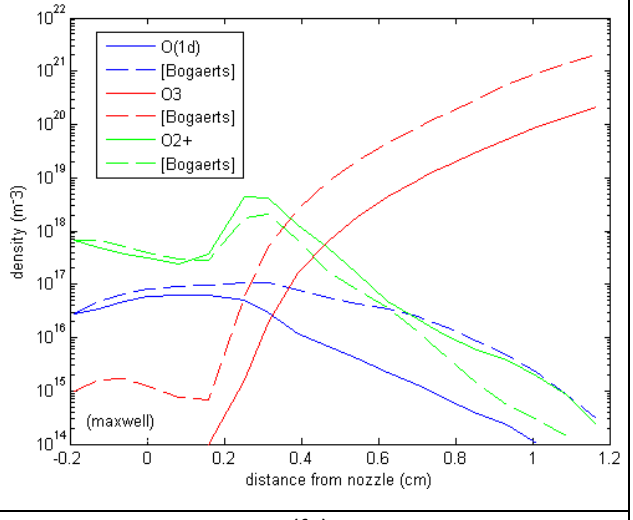

(f2)

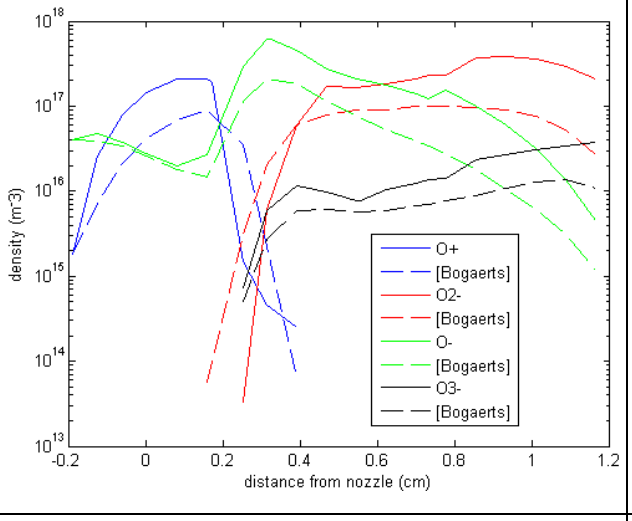

(g1)

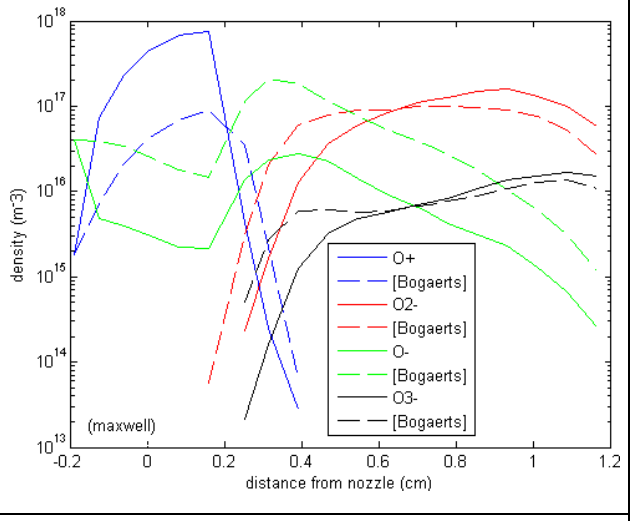

(g2)

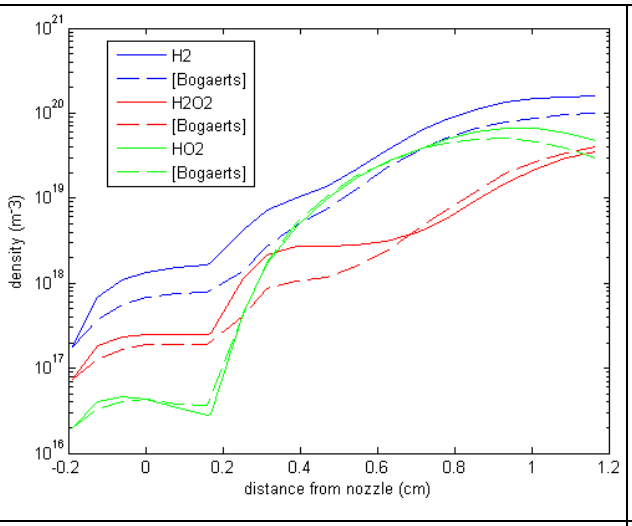

(h1)

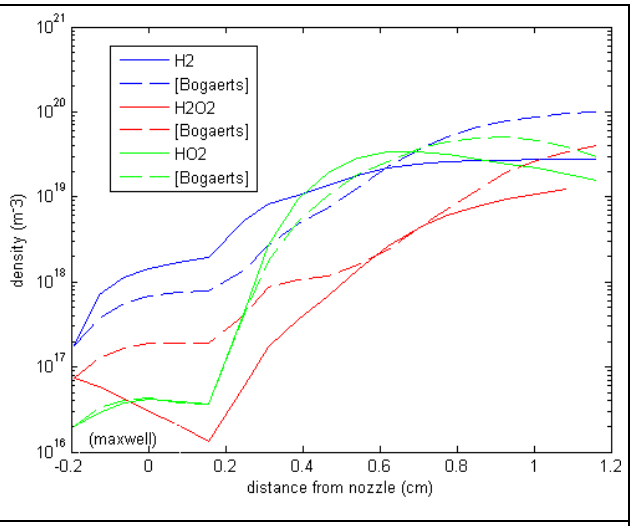

(h2)

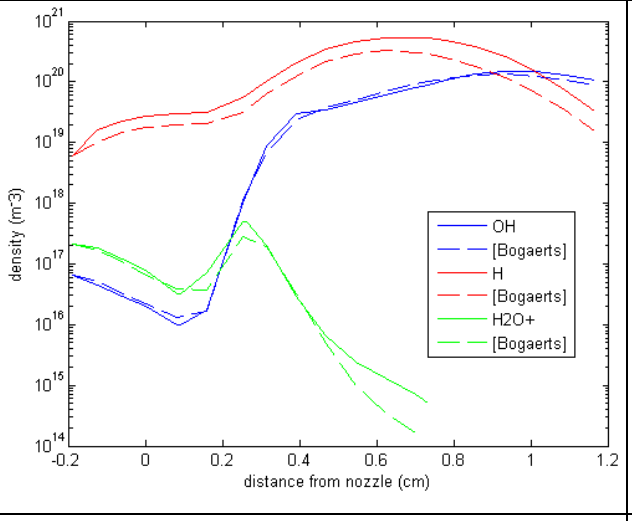

(i1)

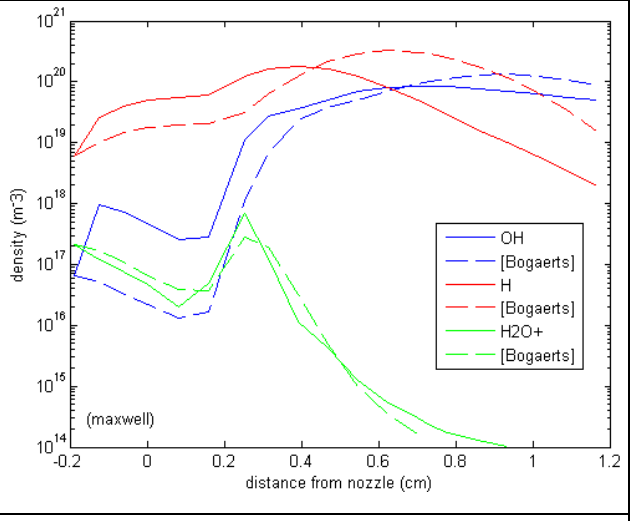

(i2)

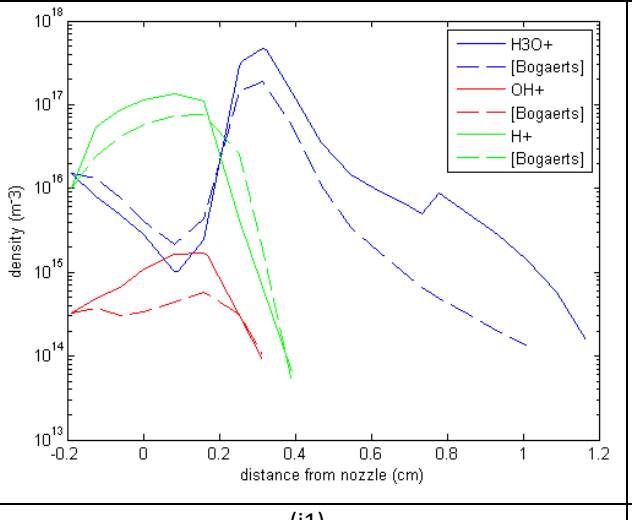

(j1)

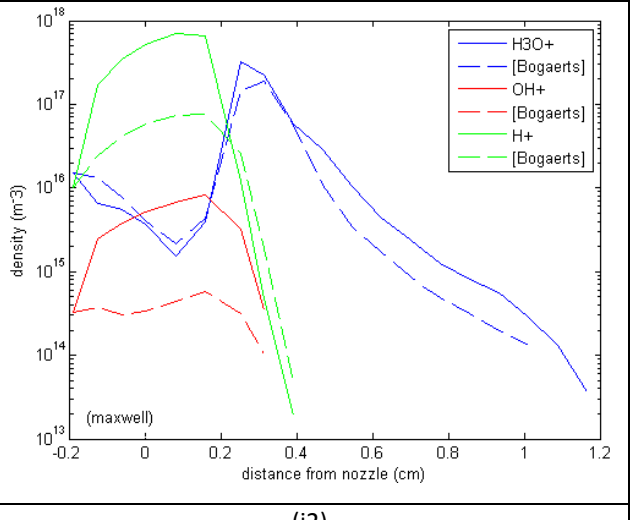

(j2)

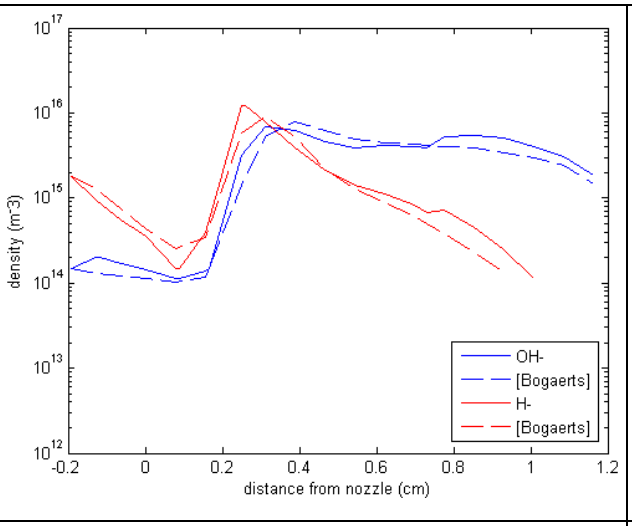

(k1)

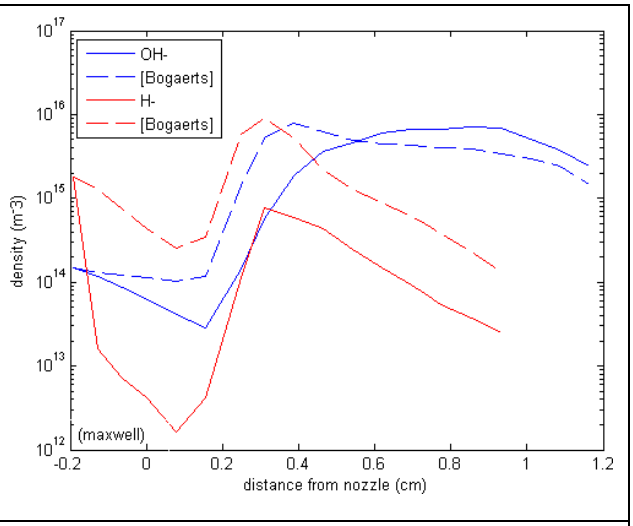

(k2)

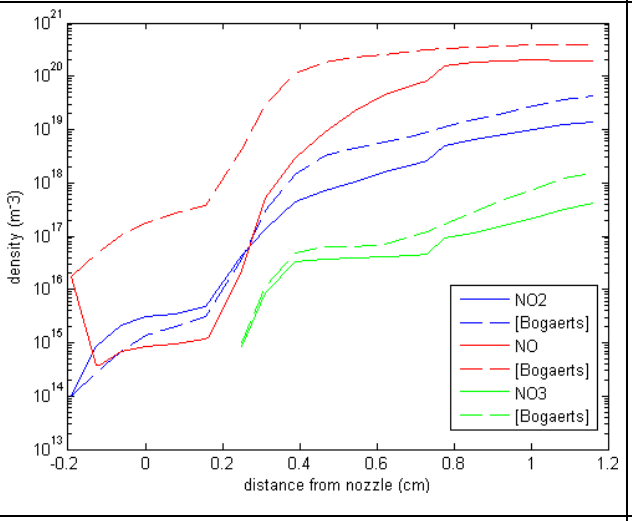

(l1)

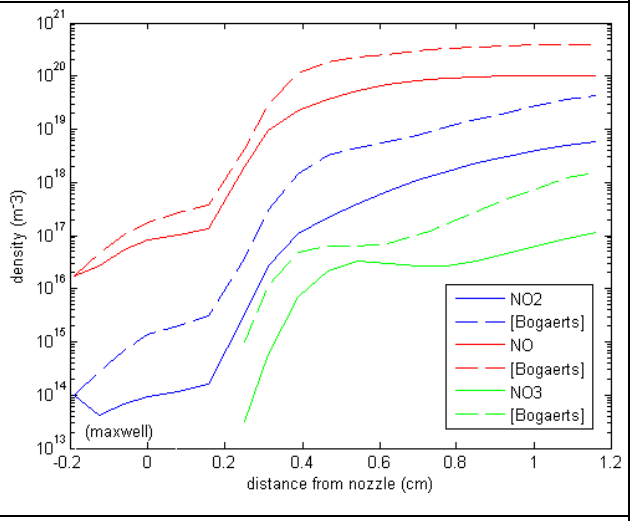

(l2)

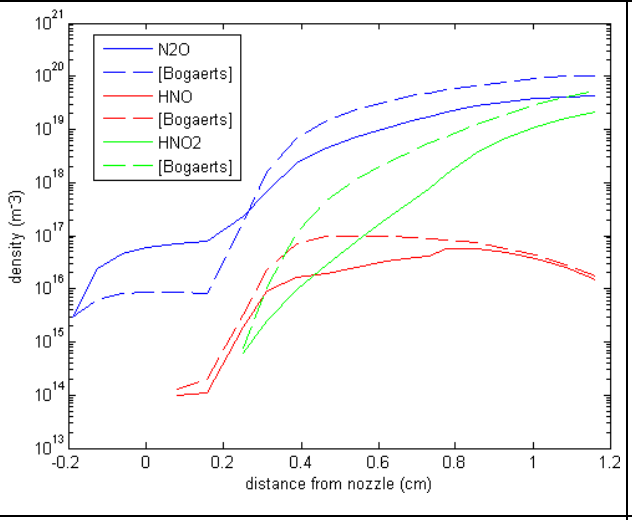

(m1)

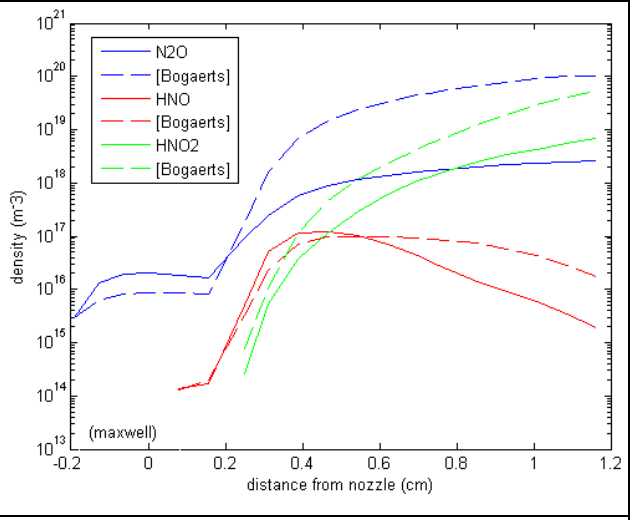

(m2)

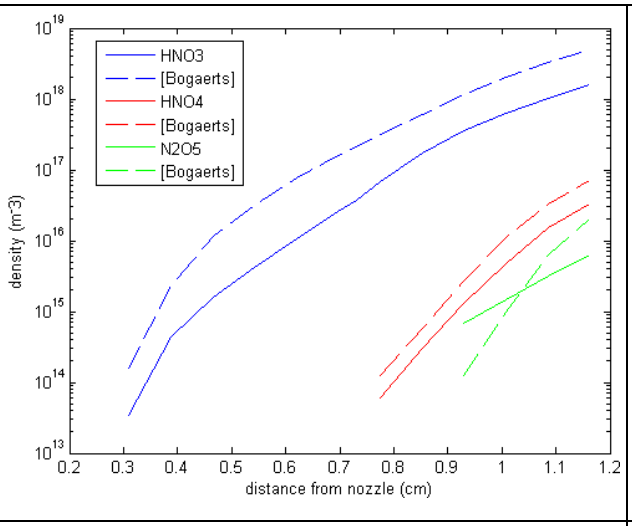

(n1)

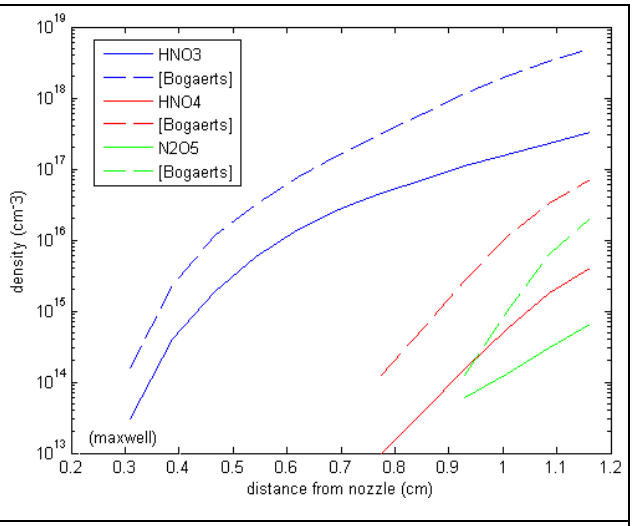

(n2)

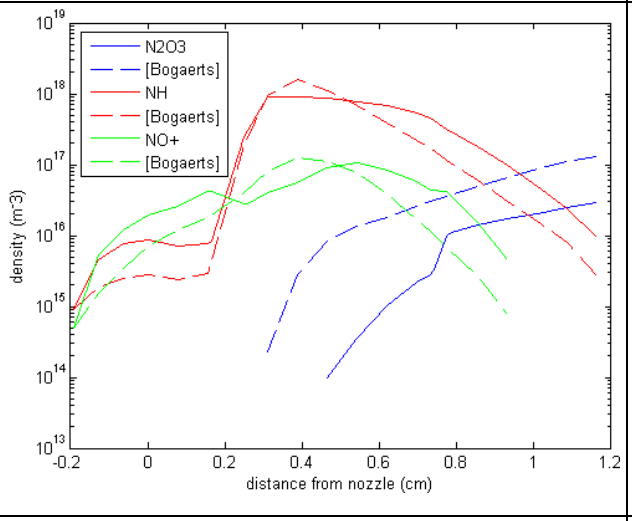

(o1)

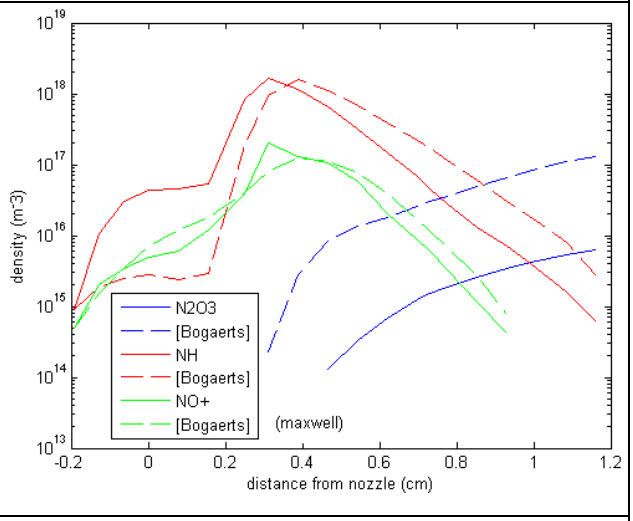

(o2)

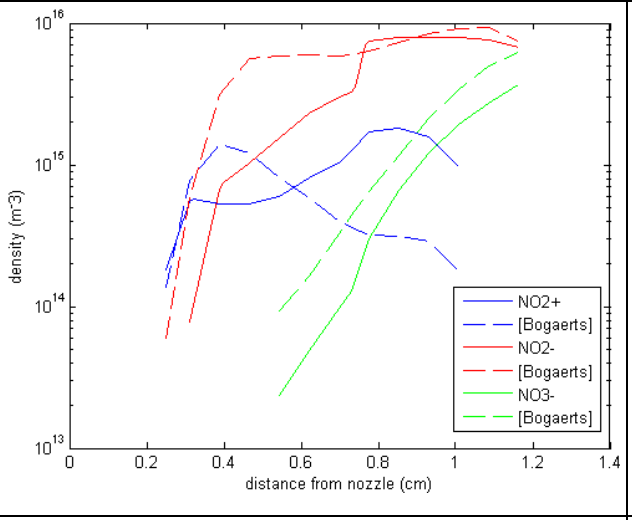

(p1)

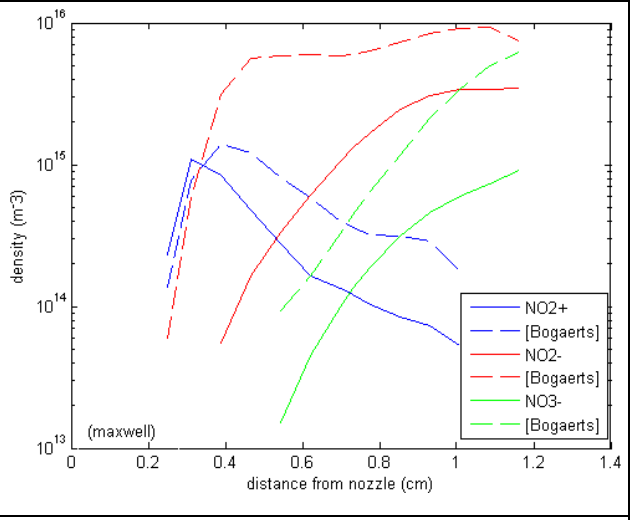

(p2)

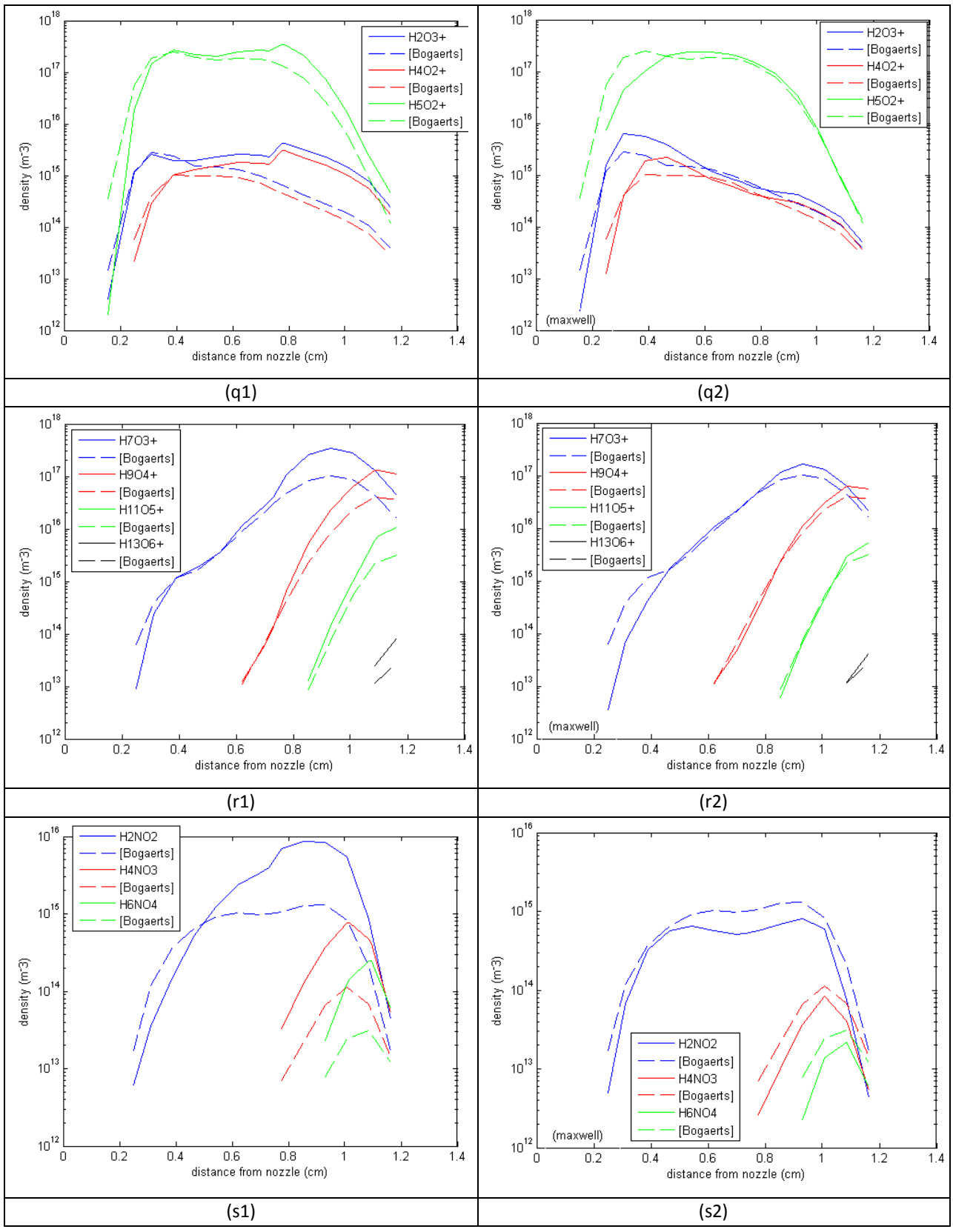

Figure 3.9: Species densities vs distance from nozzle, comparison with the results of Gaens&Bogaerts [30].

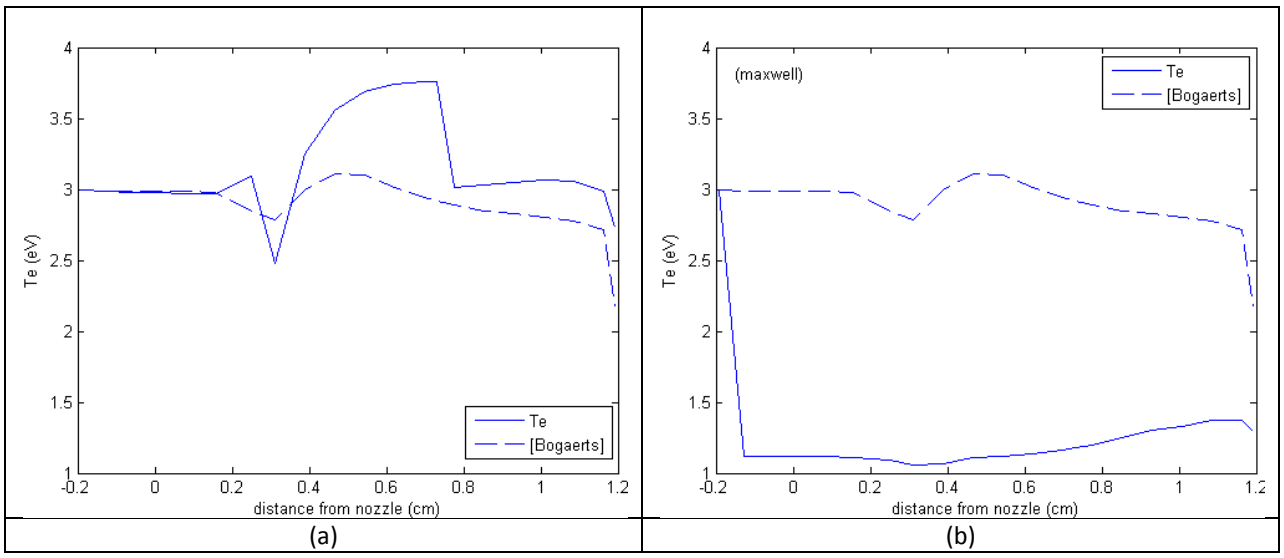

Figure 3.10: Electron temperature vs distance from nozzle.

The comments for the left columns of Figures 3.9 and 3.10, i.e., for the comparison of results of Gaens&Bogaerts with the simulation results coming from the first scenario for rate coefficients are summarized below:

The densities obtained from the extended global model (πlasma-R) are close to those presented by Gaens&Bogaerts [30] for the great majority of the species. Nevertheless, there are some deviations that for few species can exceed one order of magnitude (e.g. N_2(A), NO). The main reasons behind these differences are:

A) The Boltzmann solver does not update the reaction coefficients frequently enough: It runs roughly every 15 ms as opposed to every 10 μs in the work of Gaens&Bogaerts. This has an impact on the results due to the fact that the conditions of the experiment (gas composition, temperature) change rapidly with time.

B) The sources employed for the cross sections of some electron impact reactions are different from those used by Gaens&Bogaerts. In addition, for those reactions that it was very difficult to find sources for the cross sections, reaction coefficients derived from a Maxwellian EEDF were used. Finally, some calculations for the cross sections were necessary for some reactions (through detailed balancing, threshold reduction and scaling etc., see Table B1, Appendix B) while Gaens&Bogaerts used different methods and/or sources.

C) For some reactions (mainly ionization) the coefficients derived from Bolsig+ presented moderate oscillations (signs of difficulties with convergence). Some approximations were used for those regions of energies where the oscillations were quite strong.

D) The reaction set for this simulation is a reduced reaction set from the one employed by Gaens&Bogaerts which includes 1880 reactions. Although it is mentioned [30] that the reduced reaction set does not affect the results to a large extent, some deviations are expected.

E) From Figures 3.9 and 3.10, one can notice steep changes and derivative discontinuities of the curves, regarding the results produced by πlasma-R. The source of these artifacts is the fact that the electron reaction coefficients are updated abruptly,

only at the time instances of 0.3 and 0.58 ms and after the passage of a great amount of time (during which major changes of the gas composition occur), and not gradually by using the calculations of the Boltzmann solver much more frequently. This is the reason that these steep changes occur around 0.24 and 0.74 cm from the nozzle exit (which correspond to 0.3 and 0.58 ms).

The comments for the right columns of Figs. 3.9 and 3.10, i.e., for the comparison of results of Gaens&Bogaerts with the simulation results coming from the second scenario for rate coefficients are summarized below:

The results obtained from πlasma-R are quite close to those presented by Gaens&Bogaerts [30] for some species, although, for other species, the deviations are strongly pronounced (e.g. Ar(4s3p0), N_2(a)). The most noticeable deviation is related to the electron temperature calculated by πlasma-R which is almost three times lower than the one computed by Gaens&Bogaerts [30]. The main reasons behind these differences in this second scenario are the assumption of a Maxwell distribution, different methods and/or sources for the determination of the cross sections of some reactions and the employment of a reduced reaction set.

Regarding the comparison between the two scenarios, the results obtained from the calculated EEDFs were generally closer to the ones produced by Gaens&Bogaerts [30] than those obtained with the Maxwell distribution (right column of Figures 3.9 and 3.10), as expected, although there were few exceptions (Figure 3.9s1,s2) attributed to the reasons mentioned above (A-E). The electron temperature obtained from the calculated EEDFs was a lot closer to the result of Gaens&Bogaerts than the one obtained assuming a Maxwell distribution. Although the differences in the electron temperature between the two scenarios are very prominent, the differences in the calculated species densities are more subtle. This can be explained by the fact that at lower electron temperatures (calculated by the second scenario) the Maxwell distribution becomes less extended to higher energies (the 'tail' is restricted) and approaches the EEDFs computed by Bolsig+ at the higher electron temperatures (calculated by the first scenario). Figure 3.11 shows the Maxwell EEDF with 2 eV mean electron energy and the Bolsig+ calculated EEDF for the conditions at x=0.98 cm (4.5 eV mean electron energy). The steep changes with the Maxwell distribution resemble the ones produced by Gaens&Bogaerts.

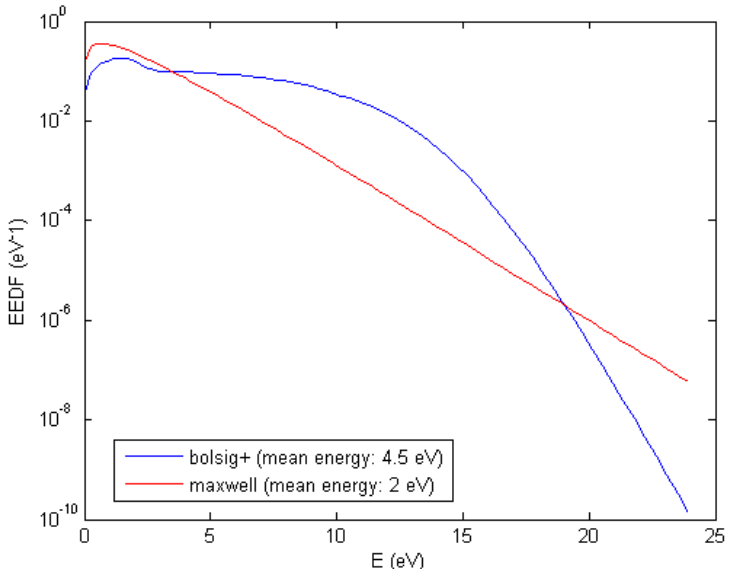

Figure 3.11: Maxwell EEDF (4.5 eV mean electron energy) and Bolsig+ calculated EEDF (2 eV mean electron energy) for the conditions at x=0.98 cm.

4. Fluid simulations of plasma jet

4.1 Introduction

As discussed in the previous chapters (see section 2.3), the gas velocity profile and the densities of the feed gas, N_2, O_2 and H_2O as a function of distance from the nozzle are used as inputs to the global model. The source of such information can be either experimental data or data computed by fluid simulations. In this chapter, the second option is explored in an attempt to develop a self-consistent model for atmospheric pressure plasma jets and eliminate the need for many inputs from experimental measurements.

Firstly, some general information about turbulence are presented and then, the turbulence over flat plates, inside channels and in free shear flow is discussed with a focus on the turbulent jet flow. Finally, before the results of the fluid simulations for the specific device [30] are presented, some aspects of turbulence modeling are preceded.

4.2 Turbulent flow [57]

Turbulence is a property of the flow and not a property of the fluid itself. In flows that are originally laminar, the turbulent regime arises from instabilities that develop as the Reynolds number increases. There is no precise definition of turbulence in fluids, nor does there exist any general theory of turbulence. Turbulence is thus characterized by several observable properties. If we accept the usually retained hypothesis that the detailed motion of the turbulent fluid is governed by the Navier-Stokes equations, then the fundamental equations of turbulence can be considered as known and thus they can form the basis of any tentative statistical theory to describe the turbulence field.

The chaotic character of turbulent fluctuations appears as a direct consequence of non-linear terms present in the Navier-Stokes equations. These non-linearities are apparent through several important consequences which, considering the absence of any precise definition of turbulence, serve as characteristic properties:

1) Physical quantities such as velocity and pressure vary in an apparently random way.

2) The presence of countless swirling eddies conveys the fact that a turbulent flow is highly rotational (Figure 4.1). The turbulent motion thus presents strong fluctuations in the curl of velocity. The non-linearities control the interactions between these eddies of differing size. An acoustic field, even random, is not turbulent at all because it is irrotational.

3) A turbulent field diffuses any transportable quantity, such as temperature or a dye, but also momentum, rapidly. In reality, turbulent diffusion is due to convective terms at the fluctuating level. A traced fluid particle marked by a dye is then distorting, branching out and progressively fraying (Figure 4.2).

4) Fluctuating turbulent motions are always three-dimensional and unsteady.

5) The detailed properties of a turbulent flow present an extreme sensitivity to initial and boundary conditions. This behavior is apparent if we consider a tiny deviation in the initial conditions, we then observe that the two flows become rapidly very different from each other if we look at its instantaneous detailed description. This unpredictable character of the detailed fluid particle trajectories on sufficiently long time intervals

corresponds to a loss of the memory of initial conditions. This is the unpredictability phenomenon. Some properties of turbulence however remain reproducible, such as statistical properties, mean values and spectral distributions.

6) The progressive loss of memory of a turbulent flow which forgets, after some elapsed time, the detail of fluctuations in the initial conditions some way justifies the statistical approach to turbulence, since, to some extent, the detail of initial conditions can be ignored. In this connection, it is possible to distinguish newly created turbulence which still retain the memory of the conditions in which it was created (much more difficult to study) from fully developed turbulence which has lost the memory of initial conditions (and which can be studied relatively more easily because it is subject to universal laws).

7) There exists a whole cascade of eddies of smaller and smaller scales, created by non-linear processes due to inertial terms in the equations of motion (Figure 4.1).

8) Turbulence cannot be sustained by itself, it needs an energy supply. This source of energy can have various origins, the most usual is shear or strain of the mean flow, but the origin can also come from external forces. If turbulence is deprived of any generation process, it decays progressively. Turbulence is dissipative. The mechanism of viscous dissipation of turbulence is related to the existence of strong gradients of the instantaneous velocity field. The instantaneous strain rates indeed become very high inside the smallest eddies and the degradation of the turbulent kinetic energy into heat is thus very strong (Figure 4.1).

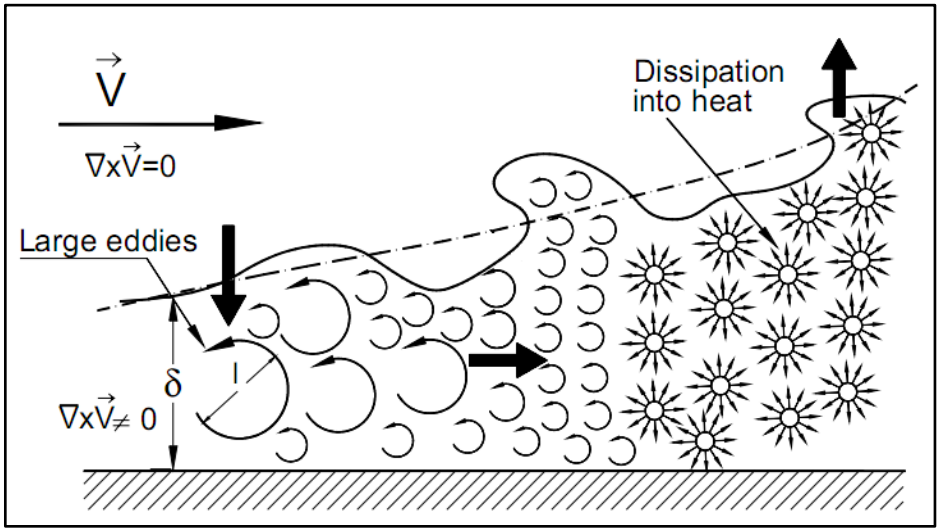

Figure 4.1: Schematics of an instantaneous energy cascade in turbulent flow. The arrows indicate energy extraction, transfer and dissipation [58].

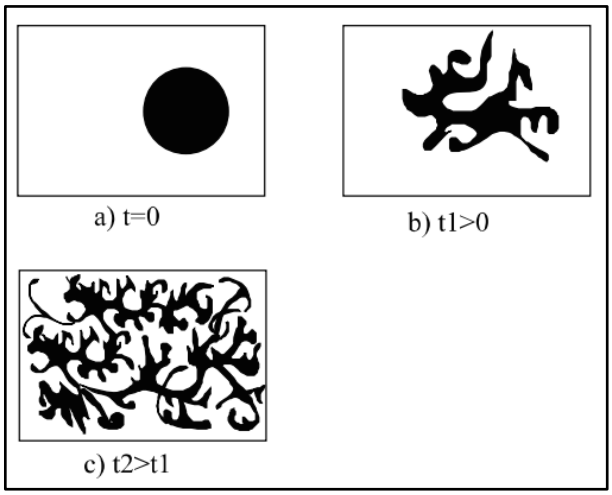

Figure 4.2: Evolution of a volume marked by a dye under the effect of turbulent diffusion [57].

Turbulence is an eddying motion which, at high Reynolds numbers usually reached in practical flows, shows a wide spectrum spreading over a significant range of eddy scales and a corresponding spectrum in frequency. The turbulent motion, always rotational, can be perceived as a muddle of swirling eddies whose rotational curl vectors are directed randomly in space and are strongly unsteady. The largest eddies, which are associated with the low frequency range of the energy spectrum, are determined by the boundary conditions of the flow. Their length scale is comparable to the order of magnitude of the whole domain occupied by the flow itself. The smallest eddies, associated with high frequencies in the spectrum, are determined by viscous forces. The energy spectrum width, i.e. the scale difference between the largest and the smallest eddies, increases with the Reynolds number. Momentum and heat transfer are mainly due to large-scale motions and thus, it is mainly these large eddies that must be considered in turbulence models: the velocity and length scales introduced in the usual turbulence models are basically macroscales. The large eddies interact with the mean flow (because their characteristic scales have the same order of magnitude), they extract kinetic energy from the mean flow and supply this energy to the large-scale agitations. Turbulent structures can be considered as swirling vortex elements that are stretching each other. This vortex stretching is one of the most important aspects of turbulent motion. It produces the transfer of energy on smaller and smaller scales until the viscous forces become active and dissipate this energy, this is the energy cascade (Figure 4.1). The amount of energy coming from the mean flow and injected into the turbulent motion is determined by the large scale motions, it is only this amount of energy which will be able to cascade to smaller scales and then to be dissipated. Thus, the dissipation rate of kinetic energy is determined by the large-scale motions, although the dissipation is a viscous process that occurs mainly at the level of small eddies. The fluid viscosity does not determine the dissipation rate itself but only the length of the scale at which it happens. The higher the Reynolds number, the smaller the dissipative eddies. Owing to their interaction with the mean flow, the large eddies are strongly dependent on the boundary conditions of the problem. The mean flow often presents preferred directions that are then imposed on the large-scale turbulent motions. These big eddies may consequently be highly anisotropic. During the cascade process, this directional dependency is however weakened. When the Reynolds number is sufficiently high, then the range of big eddies and the range of small dissipative eddies become clearly separated in the spectrum and this directional dependency is almost completely lost. This is the tendency of fine scale turbulence to local isotropy. The occurrence of turbulence may have various causes. In turbulent shear flows, it is generally due to an increase in the flow Reynolds number $Re = \rho UL/\mu$, which

represents the ratio of inertial forces to viscous forces. However, the occurrence of turbulence is also influenced by external forces (Archimedean forces, Coriolis forces, etc.). One of the acting mechanisms in the onset of turbulence in shear flows is the Kelvin-Helmholtz instability which is a type of vortex sheet instability which is encountered in particular in mixing layers, boundaries of jets or wakes. This instability gives rise to spiral whorls, a precursor of turbulence. Figure 4.3 shows a visualization of a circular jet which images the convective Kelvin-Helmholtz instabilities at the boundaries of the jet after the nozzle exit. Several diameters downstream, the transition to turbulence rapidly takes place, spiral structures break up and the general appearance becomes apparently random. The transition is all the more fast and sudden as the Reynolds number is high. In a boundary layer, spanwise vortices (perpendicular to the direction of mean flow), resulting from the Kelvin-Helmholtz instability and taking the form of vortex filaments will have the tendency to oscillate away from spanwise direction [57].

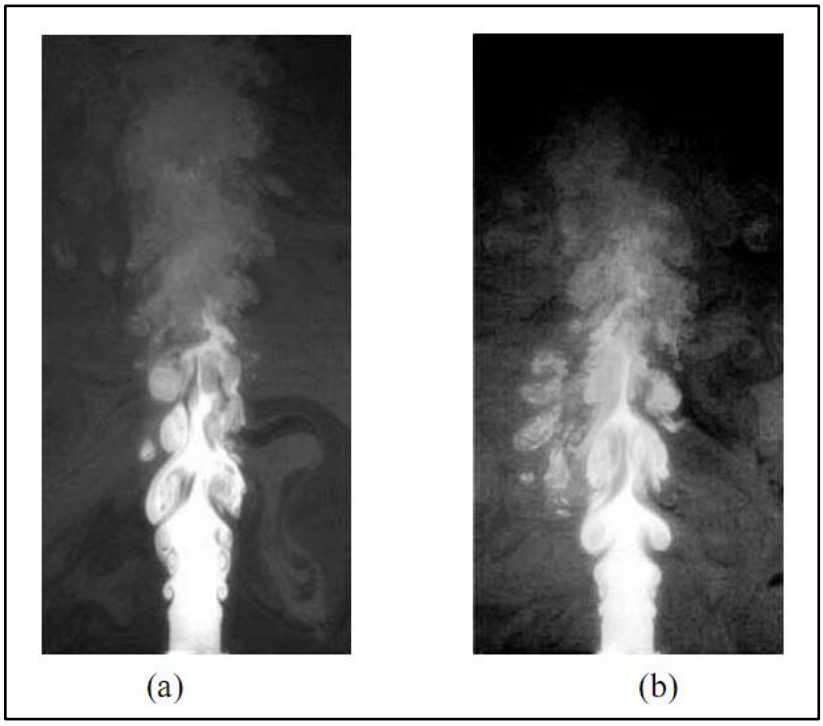

Figure 4.3: Visualization of a circular jet of air developing in still ambient air. Kelvin-Helmholtz instabilities at the boundaries of the jet are visible. The Reynolds number at the nozzle exit is Re=4935 (a), Re=6148 (b) [57].

Turbulent flows exist over flat plates, inside channels and in free shear flows (turbulent flow in jets).

4.2.1 Turbulence over flat plates and inside channels

Considering the flow of a fluid over a flat plate, as shown in Figure 4.4, the uniform velocity fluid hits the leading edge of the flat plate, and a laminar boundary layer begins to develop. The flow in this region is very predictable. After some distance, small chaotic oscillations begin to develop in the fluid field, and the flow begins to transition to turbulence, eventually becoming fully turbulent [59].

The transition between the three regions (laminar-transitional-turbulent, see Figure 4.4) can be defined in terms of the Reynolds number. If the conduit (plate) boundary is rough, the transition to fully turbulent flow can occur at lower Reynolds numbers.

Alternatively, laminar conditions can persist to higher Reynolds numbers if the conduit is smooth and inlet conditions are carefully designed. In the laminar regime, the flow of the fluid can be completely predicted by solving the steady-state Navier-Stokes equations, which predict the velocity and the pressure fields. It can be assumed that the velocity field does not vary with time, and get an accurate prediction of the flow behavior. As the flow begins to transition to turbulence, chaotic oscillations appear in the flow, and it is no longer possible to assume that the flow is invariant with time (Figure 4.5) [59].

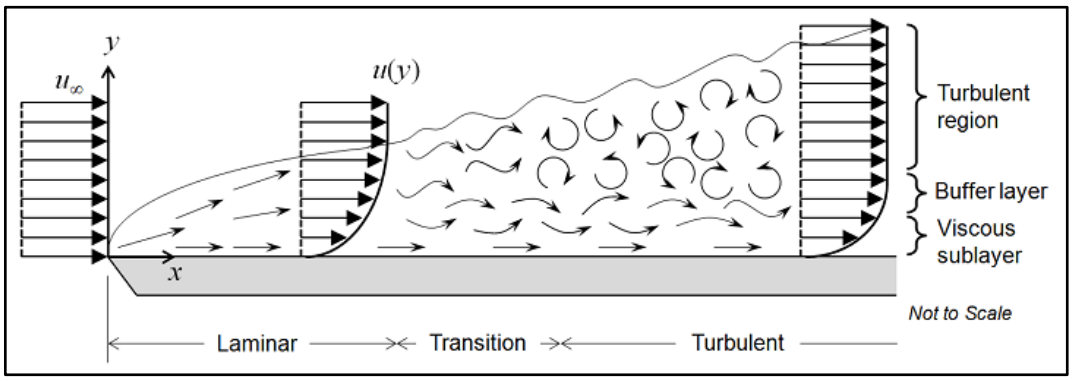

Figure 4.4: Flow of a fluid over a flat plate [59].

In this case, it is necessary to solve the problem in the time domain, and the mesh used must be fine enough to resolve the size of the smallest eddies in the flow. As the Reynolds number increases, the flow field exhibits small eddies, and the timescales of the oscillations become so short that it is computationally unfeasible to solve the Navier-Stokes equations [59].

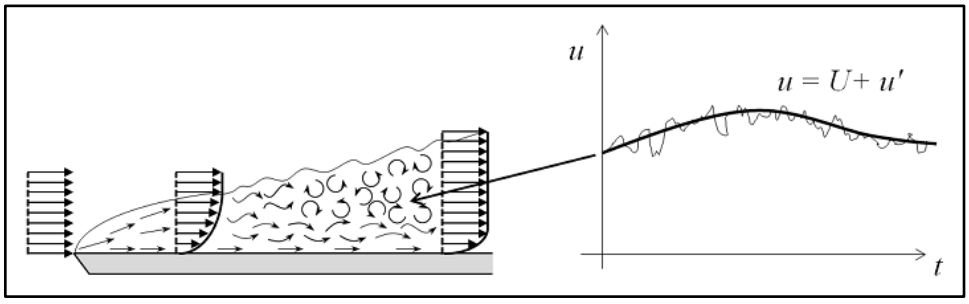

Figure 4.5: Velocity at a point versus time and the time averaged velocity [59].

The turbulent flow near a flat wall can be divided up into four regions (Figure 4.6). At the wall, the fluid velocity is zero, and for a thin layer above this, the flow velocity is linear with distance from the wall. This region is called the viscous sub-layer, or laminar sub-layer. Further away from the wall is a region called the buffer layer. In the buffer region, the flow begins to transition to turbulent, and it eventually transitions to a region where the flow is fully turbulent and the average flow velocity is related to the log of the distance to the wall. This is known as the log-law region. Even further away from the wall, the flow transitions to the free-stream region. The viscous and buffer layers are very thin, and if the distance to the end of the buffer layer is δ, then the log-law region will extend about 100δ away from the wall [59].

In boundary layer flow over a flat plate, experiments confirm that, after a certain length of flow, a laminar boundary layer will become unstable and turbulent. This instability occurs usually when $Re_x = \frac{v_\infty x}{\nu} \approx 5 \times 10^5$, where x is the distance from the leading edge of the flat plate, ν is the kinematic viscosity and v_∞ is the free-stream velocity of the fluid outside the boundary layer [60]. For flow in a pipe of diameter D, experimental

observations show that for “fully developed” flow, laminar flow occurs when $Re_D = \frac{\upsilon D}{\nu} < 2300$ and turbulent flow occurs when $Re_D > 4000$. In the interval between 2300 and 4000, laminar and turbulent flows are possible and are called “transition” flows, depending on other factors, such as pipe roughness and flow uniformity. This result is generalized to non-circular channels using the hydraulic diameter, allowing a transition Reynolds number to be calculated for other shapes of channel [61].

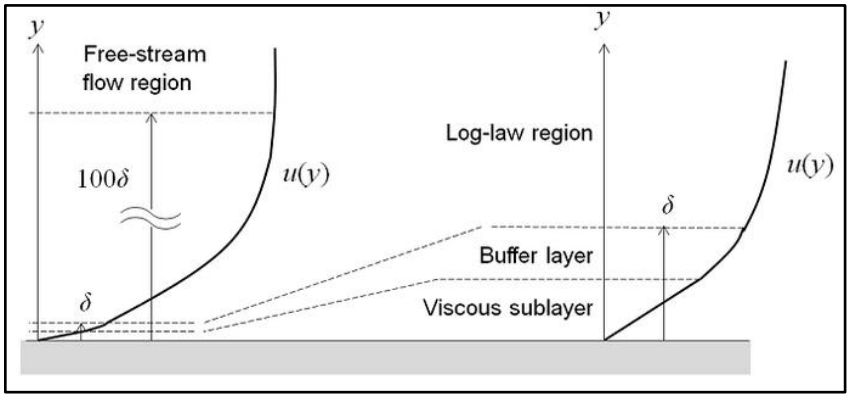

Figure 4.6: Regions of turbulent flow near a flat wall [59].

4.2.2 Free shear flow–turbulent flow in jets

The type of flow which is not confined by solid walls is called free shear flow (or free flow). The three types of free shear flow are the free jets, the free wakes and the mixing layers. Free jets are flows where a fluid flows with no obstacles inside another fluid which is at rest. Free wakes are generated behind any solid body that is exposed to a fluid flow and mixing layers are formed between two streams that move parallel to each other with different velocities [58].

The most common type of turbulent free shear flow is the free jet turbulent flow (turbulent jets). A region of finite thickness with a continuous distribution of velocity, temperature, and species concentration is formed on the boundary between the jet and the surrounding stationary fluid; this region is termed the turbulent jet boundary layer or shear layer. The thickening of the shear layer, which consists of particles of the surrounding medium carried along with the jet and particles of the jet itself that have been slowed down, leads, on the one hand, to an increase in the cross section of the jet and, on the other hand, to a gradual "eating up" of its non-viscous core - the region between the inside boundaries of the shear layers (Figure 4.7).

On the outside, the shear layer comes into contact with the stationary fluid. The outside boundary is the surface where the axial velocity component is equal to zero. On the inside, the shear layer changes to a constant velocity core. Experiments show a continuous broadening of the velocity profile of the jet. The velocity profile becomes “lower” and “wider” with increasing distance from the beginning of the jet [62]. The boundary in Figure 4.7 represents the outer ‘‘edge” of the shear layer between the jet flow and the stagnant surrounding fluid. There are three different regions that can be defined in the round jet: the near-field, the intermediate-field and the far-field. The near-field region is where the flow characteristics match those of the nozzle-exit, and is usually found within $0 < x/d < 6$ (d is the nozzle exit diameter). The far-field region, located at approximately $x/d > 30$, is the fully-developed or self-similar region (the jet becomes similar in appearance to a flow of fluid from a point source for an axially symmetric case [62]). The intermediate-field region lies between the near- and far-fields of the jet. The near- and intermediate-fields together comprise the development portion

of the jet, where it often dominates practical applications of jets for which upstream conditions can significantly influence heat, mass, and momentum transfer. Therefore, the ability to control the flow development in this region would have a vital impact on many of those engineering applications. In the shear layer vortex cores will form, resulting from the Kelvin-Helmholtz instability (see Figure 4.3), evolve and pair-up to form large eddies because of the large velocity gradient in the radial direction. These large eddies break down and form smaller and smaller eddies, and the turbulence structures decrease in scale. Throughout this process, energy is transferred from the large-scale structures to the smaller scales in the outer layer. It is noteworthy that the regular vortex formation and pairing processes are important for the mixing and entrainment of the surrounding medium, where it should be emphasized that the thicker the initial shear layer, the weaker the vortex formation it gets.

Research work on the jet flow may be mainly categorized into two streams; one stream is directed to the study of the jet flow structure, particularly in the far, self-similar region. The other stream is directed to the study of the influence of the flow at the jet origin, often termed initial conditions, on the jet flow; particularly in the near and intermediate regions. The initial conditions of a jet are conventionally defined to be the exit Reynolds number, nozzle-exit profiles of mean velocity and the turbulence intensity, nozzle-exit geometric profiles, and aspect ratio (noncircular jets). The downstream development of a jet is also dependent on the boundary conditions, e.g., the presence or absence of a screen enclosure around the jet flow and/or a wall setting flush at the nozzle exit plane and the conditions of the surrounding environment such as: background turbulence and large-scale motions (draughts) that may exist in the laboratory environment [63].

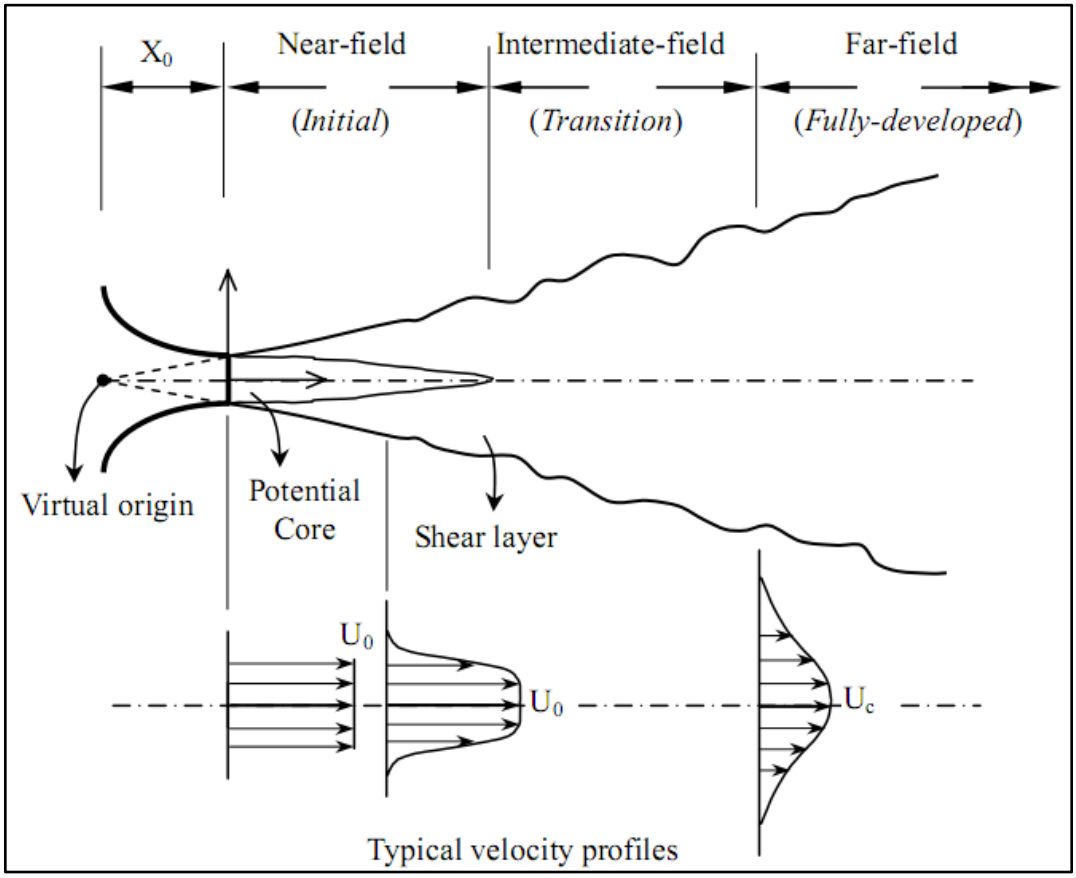

Figure 4.7: Schematic of the free turbulent round jet [63].

If the Reynolds number at the jet exit is greater than a few thousands, the radial spread of the mean velocity field and the decay of the mean centerline velocity in the

downstream direction are independent of Reynolds number. Further, if the Reynolds number is less than 30, the jet is laminar, normally called "dissipated laminar jet". For Reynolds number greater than 500, the jet has a laminar length after which it becomes turbulent. This laminar length decreases with increasing Reynolds number. However, for Reynolds numbers greater than about 2000, the jet becomes turbulent very close to the exit as, for example, shown in Figure 4.8 with the spread rate of the jet becoming constant [63].

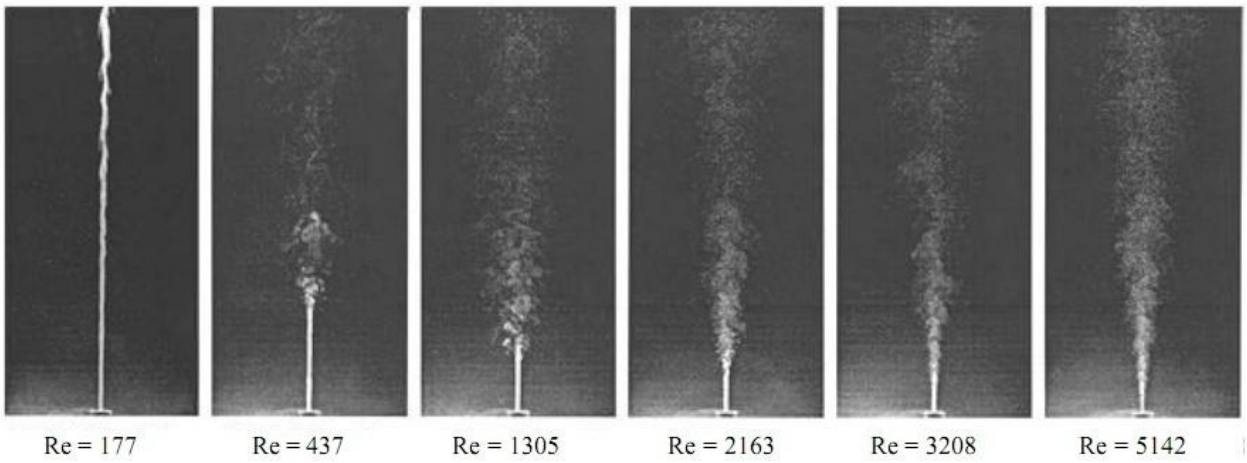

Figure 4.8: Schematic of free turbulent jets with different Reynolds numbers [63].

4.3 Turbulence modeling

It is accepted that Navier-Stokes equations, used to describe the behavior of viscous fluids, can describe properly the turbulent phenomena [64]. Unfortunately, with the current capacity of computing power, the attempts of direct numerical simulation (DNS) of Navier-Stokes equations have been limited to low Reynolds numbers (Re) or/and simple geometries. Despite the current advance of the computation the possibility of using DNS for flows with high Reynolds numbers in practical applications is still surely distant [64].

From its beginnings the attempts of simulating turbulence have been focused on models based on the average in time or in space of magnitudes involved in the problem (velocity, pressure) originating the models of turbulence associated with the Reynolds Averaged Navier-Stokes (RANS) equations [64]. A RANS formulation is based on the observation that the flow field (u) over time contains small, local oscillations (u') that can be treated in a time-averaged sense (U) (Figure 4.5) [59]. Turbulent flows contain many unsteady eddies covering a range of sizes and time scales. RANS equations are developed from the time-dependent three-dimensional Navier-Stokes equations that are averaged in such manner, that unsteady structures of small sizes in space and time are eliminated and become expressed by the mean effects on the flow through the so-called Reynolds or turbulent stresses. These stresses have to be interpreted in terms of averaged variables to close the system of equations. This requires the construction of a mathematical model known as a turbulence model. Figure 4.9 shows a solution obtained from DNS (at a specific time instance) and a solution obtained from a turbulent model (time-averaged). Turbulence models introduce additional information to obtain physically coherent solutions [64].

Considering the velocity as $U_i = \overline{U}_i + u_i$, with $i = x, y, z$ and the pressure as $P = \overline{P} + p$, which allows us to distinguish the mean flow from the fluctuating flow, and by averaging

the Navier-Stokes and the continuity equations the RANS formalism can be obtained (gravitational forces are omitted for simplicity):

$$\frac{\partial \overline{U}_x}{\partial x} + \frac{\partial \overline{U}_y}{\partial y} + \frac{\partial \overline{U}_z}{\partial z} = 0 \ (Eq. 4.1)$$

$$\rho\left(\frac{\partial \overline{U}_x}{\partial t} + \overline{U}_x \frac{\partial \overline{U}_x}{\partial x} + \overline{U}_y \frac{\partial \overline{U}_x}{\partial y} + \overline{U}_z \frac{\partial \overline{U}_x}{\partial z}\right) = -\frac{\partial \overline{P}}{\partial x} + \mu \frac{\partial^2 \overline{U}_x}{\partial x^2} + \mu \frac{\partial^2 \overline{U}_x}{\partial y^2} + \mu \frac{\partial^2 \overline{U}_x}{\partial z^2} - \rho \frac{\partial \overline{u_x u_x}}{\partial x} - \rho \frac{\partial \overline{u_x u_y}}{\partial y} - \rho \frac{\partial \overline{u_x u_z}}{\partial z} \ (Eq. 4.2)$$

$$\rho\left(\frac{\partial \overline{U}_y}{\partial t} + \overline{U}_x \frac{\partial \overline{U}_y}{\partial x} + \overline{U}_y \frac{\partial \overline{U}_y}{\partial y} + \overline{U}_z \frac{\partial \overline{U}_y}{\partial z}\right) = -\frac{\partial \overline{P}}{\partial y} + \mu \frac{\partial^2 \overline{U}_y}{\partial x^2} + \mu \frac{\partial^2 \overline{U}_y}{\partial y^2} + \mu \frac{\partial^2 \overline{U}_y}{\partial z^2} - \rho \frac{\partial \overline{u_y u_x}}{\partial x} - \rho \frac{\partial \overline{u_y u_y}}{\partial y} - \rho \frac{\partial \overline{u_y u_z}}{\partial z} (Eq. 4.3)$$

$$\rho\left(\frac{\partial \overline{U}_z}{\partial t} + \overline{U}_x \frac{\partial \overline{U}_z}{\partial x} + \overline{U}_y \frac{\partial \overline{U}_z}{\partial y} + \overline{U}_z \frac{\partial \overline{U}_z}{\partial z}\right) = -\frac{\partial \overline{P}}{\partial z} + \mu \frac{\partial^2 \overline{U}_z}{\partial x^2} + \mu \frac{\partial^2 \overline{U}_z}{\partial y^2} + \mu \frac{\partial^2 \overline{U}_z}{\partial z^2} - \rho \frac{\partial \overline{u_z u_x}}{\partial x} - \rho \frac{\partial \overline{u_z u_y}}{\partial y} - \rho \frac{\partial \overline{u_z u_z}}{\partial z} \ (Eq. 4.4)$$

The terms $\overline{u_i u_j}$ give rise to the Reynolds stresses, which come from the non-linearities of the Navier-Stokes equations and govern the interaction between the mean flow and the fluctuating motion. The system of Eqs. 4.1-4.4 consists of 10 unknowns: 3 velocity components, pressure, 6 Reynolds stresses (there are 9 but only 6 are independent unknowns since $\overline{u_i u_j} = \overline{u_j u_i}$). But the system consists of only 4 equations and so, it is an open system. Taking the mean value of an instantaneous equation implies a loss of information that has to be reintroduced in the form of physical hypotheses: this is the closure problem. Introducing closure hypotheses that express the behavior of the turbulent medium allows us to obtain a number of equations equal to the number of unknowns and thus these equations can be solved numerically. Very schematically, the central problem is thus the problem of connection between the Reynolds stresses $R_{i,j} = \overline{u_i u_j}$ and the mean field [57].

The simplest two equation models (in addition to RANS equations) generally make use of the concept of isotropic turbulence viscosity. The Reynolds stresses are then obtained from:

$$R_{i,j} = \frac{2}{3} k \delta_{i,j} - \nu_t \left(\frac{\partial \overline{U}_i}{\partial j} + \frac{\partial \overline{U}_j}{\partial i}\right) \ (Eq. 4.5)$$

($i = x, y, z$ and $j = x, y, z$) where ν_t is the turbulence viscosity and $\delta_{i,j}$ the Kronecker delta [57].

The k-ε model is the most widely tested and used two equation transport model (two transport equations for k and ε). It consists of solving two additional equations for the transport of turbulent kinetic energy k and turbulent dissipation ε. The turbulence viscosity is given by $\nu_t = C_\mu \frac{k^2}{\varepsilon}$. The additional equations for the k-ε model are [57]:

$$\frac{dk}{dt} = P + \frac{\partial}{\partial x}\left(\frac{\nu_t}{h_k}\frac{\partial k}{\partial x}\right) + \frac{\partial}{\partial y}\left(\frac{\nu_t}{h_k}\frac{\partial k}{\partial y}\right) + \frac{\partial}{\partial z}\left(\frac{\nu_t}{h_k}\frac{\partial k}{\partial z}\right) - \varepsilon (Eq. 4.6)$$

$$\frac{d\varepsilon}{dt} = C_{\varepsilon 1}\frac{P\varepsilon}{k} + \frac{\partial}{\partial x}\left(\frac{\nu_t}{h_k}\frac{\partial \varepsilon}{\partial x}\right) + \frac{\partial}{\partial y}\left(\frac{\nu_t}{h_k}\frac{\partial \varepsilon}{\partial y}\right) + \frac{\partial}{\partial z}\left(\frac{\nu_t}{h_k}\frac{\partial \varepsilon}{\partial z}\right) - C_{\varepsilon 2}\frac{\varepsilon^2}{k} \ (Eq. 4.7)$$

with $P = \nu_t \frac{\partial \overline{U}_i}{\partial j}\left(\frac{\partial \overline{U}_i}{\partial j} + \frac{\partial \overline{U}_j}{\partial i}\right)$ (Einstein notation).

The recommended constants are [57]:

$c_\mu = 0.09$, $h_k = 1.0$, $h_\varepsilon = 1.3$, $C_{\varepsilon 1} = 1.44$, $C_{\varepsilon 2} = 1.92$

The number of equations are increased to 10 (Eq. 4.5) and because two more independent unknowns are added to the system (k,ε), Eqs. 4.6-4.7 are added as well. The system is now closed and can be solved numerically (k-ε model).

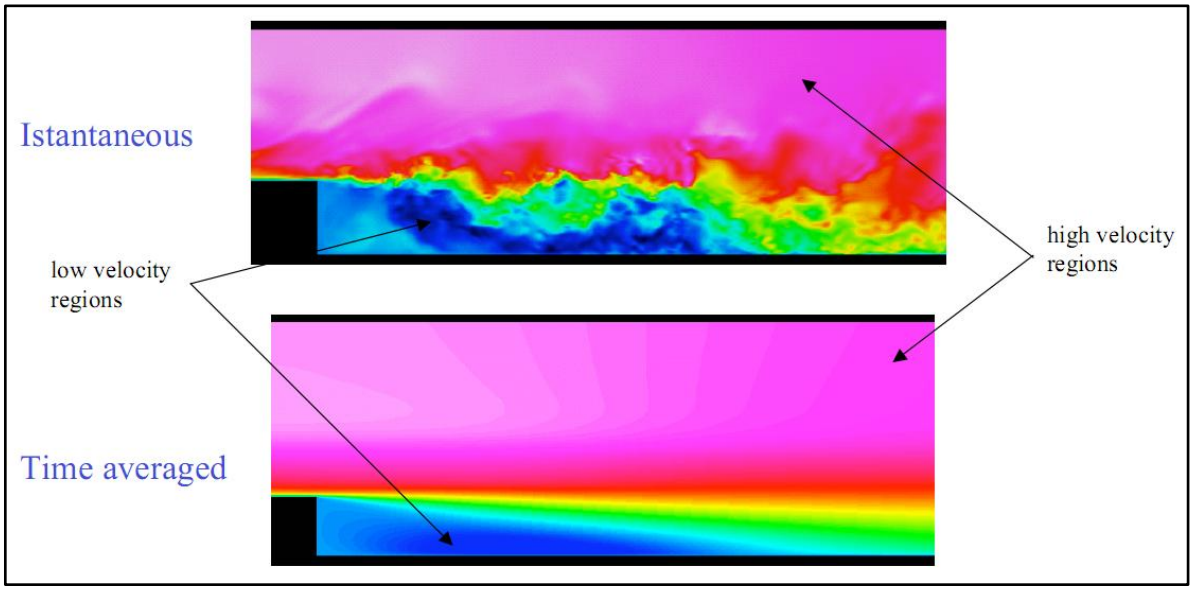

Figure 4.9: DNS solution and modeled solution [65].

It is possible to use a RANS model to compute the flow field in all four regimes of Figure 4.6. However, since the thickness of the buffer layer is so small, it can be advantageous to use an approximation in this region. Wall functions ignore the flow field in the buffer region and analytically compute a nonzero fluid velocity at the wall. By using a wall function formulation, an analytic solution for the flow in the viscous layer is assumed, and the resultant models will have significantly lower computational requirements. This is a very useful approach for many practical engineering applications. If one needs a level of accuracy beyond what the wall function formulations provide, then a turbulence model that solves the entire flow regime should be considered [59].

Turbulence models have been widely used in engineering as an alternative to the impossibility to overcome the difficulties of DNS. Most of the current methods for the simulation of this phenomenon are based on heuristic or empirical hypotheses [64].The

various models (about 200) are classified in terms of number of transport equations solved in addition to the RANS equations [65]. The most widely used models are the two equations models (good balance between computational time and accuracy). The most popular version of two equation models is the k-ε model [57], where ε is the rate at which turbulent energy is dissipated to smaller eddies (the so-called turbulent dissipation) and k is the kinetic energy per unit mass of fluid arising from the turbulent fluctuations in velocity around the averaged velocity. Still today, this model remains the workhorse of the industrial computation. k-ε is valid for the turbulent flow region, but fail in the viscous sub-layer close to the wall. Therefore k-ε should be used in combination with a wall function [64]. The k-ε model is good for free-shear layer flows with small pressure gradients. It has low memory requirements and shows good convergence [66]. On the other hand, it is inaccurate for adverse pressure gradients and strong curvature, the far-field spreading rates of round jets are predicted incorrectly and is valid only for fully turbulent flow [64, 67]. The realizable k-ε model [57] is a variant of the standard k–ε model. Its “realizability” stems from changes that allow certain mathematical constraints to be obeyed which ultimately improve the performance of this model [68]. Compared to the standard k–ε model, it is better for rotation, strong adverse pressure gradients, recirculation, mixing, channel and boundary layer flows. It also predicts spreading rate around planar and round jets [66]. The k-ω model [69] is an alternative to k-ε. The model solves for ω, which is the specific dissipation rate (ε/k), instead of ε. In contrast with k-ε, the k-ω model does not need wall functions for the flow near walls and can be very accurate in these regions. Compared to the standard k–ε model, it has superior performance for wall-bounded boundary layer, free shear, and low Reynolds number flows. It is also suitable for complex boundary layer flows under adverse pressure gradient and separation. It can also be used for transitional flows (though tends to predict early transition). Separation is typically predicted to be excessive and early. It is also oversensitive to inlet free-stream turbulence properties and sensitive to the initial guess [64, 66, 68].

The low Reynolds number k-ε model [64] is another variant of the k-ε model that uses the k-ε model only away from the wall in the fully turbulent region, and in the near-wall layer, where the viscosity effects are important, the turbulence is resolved with a one-equation model involving a length-scale prescription (no wall functions). This model improves the flow prediction in the boundary layer, but requires a very fine mesh in that area to accurately solve the boundary layer [64].

4.4 Fluid simulation of the atmospheric pressure plasma jet

The velocity field and the species (feed gas, N_2, O_2 and H_2O) densities versus the distance from the nozzle exit of the plasma jet device are calculated by a 2d axisymmetric fluid model using a commercial code, namely Comsol (v4.3b); no electric fields are considered. The geometry of the computational domain is given in Figure 4.10 and includes the internal geometry of the device producing the jet and the space outside the device where the jet flow takes place.

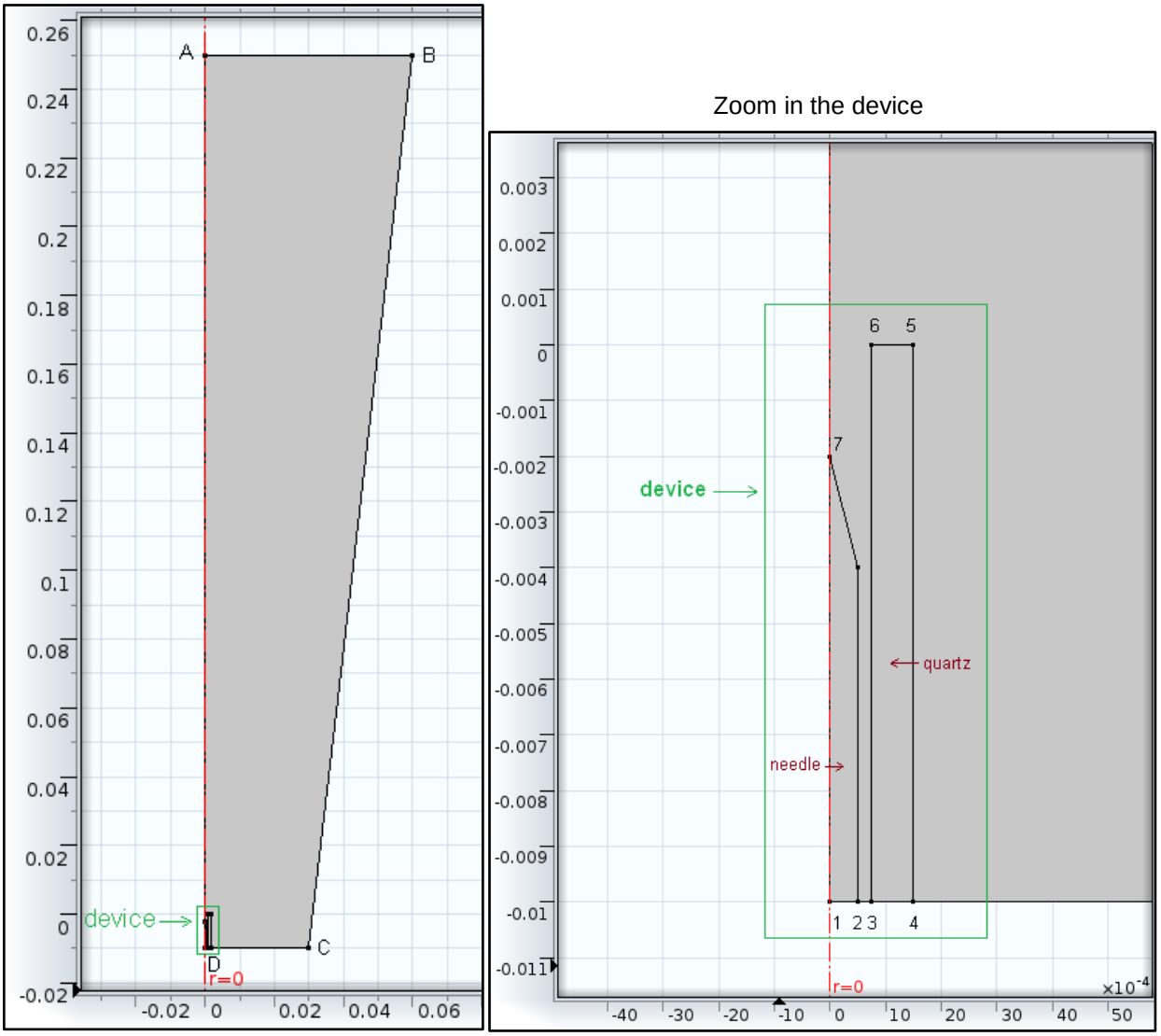

(a) (b)

Figure 4.10: Geometry of the domain (a) and zoom in the device (b).

Argon gas is supplied through boundary 2-3 (Figure 4.10b) inside the device with 2 slm rate causing a gas velocity of about 36 m/s. The fact that the jet is issuing into an ambient, but similar, fluid renders the flow unstable and transition to turbulence occurs at very low Reynolds numbers (see 4.2.2). The gas temperature is an input to the model and can be seen in Figure 4.11. The temperature used is taken from [70] (experimental data) and is approximated in this model by the analytic function

$$T(z,r) = (T_{max}(z) - 293)e^{-1000r} + 293 \ [K] \ (Eq. 4.8)$$

which is very close to the distribution of [70], with T_{max} the on-axis temperature [70]. z is the vertical coordinate and r is the horizontal coordinate. The Reynolds number inside the annulus is given by

$$Re = \rho v D_H/\mu \ (Eq. 4.9)$$

with $D_H = D_2 - D_1 = 0.0015 - 0.001 = 0.0005$ (m) the hydraulic diameter of the annulus, ρ the gas density, μ the gas viscosity and v the gas velocity ($\rho = 1.65$ kg/m^3, $v = 36$ m/s, $\mu = 2.23 * 10^{-5}$ Pa.s and $Re = 1330$). Although the Reynolds number inside the device is below the pipe critical value for turbulence (2300), it is still quite high.

Three different fluid models are examined. **The first model** uses the k-ε turbulence model everywhere in the domain (easy convergence, good initial estimate), the **second** solves with the k-ω model everywhere in the domain (better for transitional flow) and the **third** solves with the laminar model inside the device (since Reynolds number is below the critical value for turbulence) and k-ε outside the device.

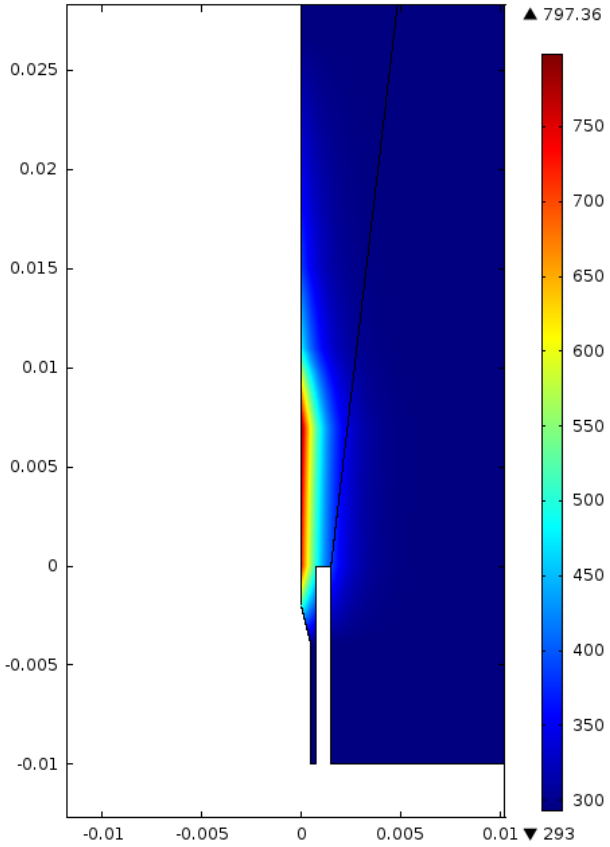

Figure 4.11: The gas temperature distribution used as input to the model.

For the k-ε model (first model), the boundary conditions are, for the boundary 2-3 (Figure 4.10b), 2 slm (3.333e-5 m^3/s) mass flow, turbulence length scale $L_T = 1.9 * 10^{-5}$ (m) and turbulent intesity $I_T = 0.07$. The turbulence intensity, I_T, is defined as the ratio of the root-mean-square of the velocity fluctuations, u', to the mean flow velocity, u_{avg}. The turbulence length scale, L_T, is a physical quantity related to the size of the large eddies that contain the energy in turbulent flows. These values are determined according to [71], $L_T = 0.038 * D_H$ and $I_T = 0.16 * Re_{D_H}^{-1/8}$ [71] and are valid for fully developed pipe flows, where Re_{D_H} is the Reynolds number based on the pipe hydraulic diameter. Boundary AB (Figure 4.10a) is outlet with normal stress 101300 N/m^2. The normal stress condition is a more relaxed constraint than no viscous stress which is an

over-constraint for the flow. This boundary condition implicitly sets a constraint on the pressure that for 2d flows is $p = 2\mu\frac{\partial u_n}{\partial n} + f_0$ and if $\partial u_n/\partial n$ is small, it states that $p \approx f_0$ [59]. Boundaries BC and CD (Figure 4.10a) are open boundaries with normal stress 101300 N/m^2 and zero turbulent kinetic energy and turbulent dissipation rate. Wall functions have been used for the walls of the device.

For the calculation of the species *i* (Ar (feed gas), O_2, N_2, and H_2O) densities a mass balance for each species should be formulated,

$$\rho(\boldsymbol{u}\cdot\nabla)\omega_i = \nabla\cdot\left(\rho D_i\nabla\omega_i + \rho\omega_i D_i\frac{\nabla M_n}{M_n}\right) \ (Eq.\ 4.10)$$

$$M_n = \left(\sum_i \frac{\omega_i}{M_i}\right)^{-1} \ (Eq.\ 4.11)$$

where ρ denotes the mixture density, $\boldsymbol{u}$ the mass average velocity of the mixture, ω_i is the mass fraction of species i, M_n is the mean molar mass, M_i is the molar mass and D_i are the diffusion coefficients of species i. The latter is calculated by the mixture-averaged diffusion model, i.e.

$$D_i = \frac{1-\omega_i}{\sum_{j\neq i}\frac{x_j}{D_{ij}}} \ (Eq.\ 4.12)$$

where D_{ij} are the binary diffusion coefficients for the species pairs present and x_j are the molar fractions.

This mixture-averaged diffusion model requires the binary diffusion coefficients of the species which are calculated with the Chapman–Enskog theory [72]. The relation for the binary diffusion coefficients of a species i in species j is:

$$D_{ij} = 0.0018583\sqrt{T^3\left(\frac{1}{M_i}+\frac{1}{M_j}\right)}\frac{1}{p\sigma_{ij}^2\Omega_{D,ij}}\ [\mathrm{cm}^2/\mathrm{s}] \ (Eq.\ 4.13)$$

where T is the temperature (K), p is the pressure (atm), M_i is the molecular weight of species i (g/mol), σ_{ij} (Å) is the binary collision diameter, which is estimated from collision diameter parameters σ_i (Å) using the mixing rule:

$$\sigma_{ij} = \frac{1}{2}\left(\sigma_i + \sigma_j\right) \ (Eq.\ 4.14)$$

The quantity $\Omega_{D,ij}$ is called the collision integral for diffusion and is a function of the reduced temperature T_R, defined as $T_R = k_B T/\varepsilon_{ij}$ where k_B is the Boltzmann constant and ε_{ij} is the characteristic energy appearing in the Lennard–Jones potential for the binary pair estimated using the mixing rule $\varepsilon_{ij} = \sqrt{\varepsilon_i\varepsilon_j}$. The molecular parameters for the individual species are shown in Table 4.1 and are coming from [72]. The function $\Omega_{D,ij}$ comes from [72], and is constructed in this model as an interpolated function versus temperature (so as to cover the wide range of temperatures present in the model). The calculated diffusion coefficients are shown in Table 4.2.

Table 4.1: Molecular parameters for the individual species.

$Substance$	$Molecular\ weight$	$\sigma\ [\dot{A}]$	$\varepsilon/k_B\ [K]$
Ar	39.948	3.432	122.4
N_2	28.013	3.667	99.8
O_2	31.999	3.433	113.0
H_2O	18.015	2.641	809.1

Table 4.2: The calculated diffusion coefficients.

D_{Ar-N2}	$(3.636 * 10^{-9} * T^{1.5})/\left(p * 9.87 * 10^{-6} * \Omega(0.00905 * T)\right)(\mathrm{cm}^2/\mathrm{s})$
D_{Ar-O2}	$(3.741 * 10^{-9} * T^{1.5})/\left(p * 9.87 * 10^{-6} * \Omega(0.0085 * T)\right)(\mathrm{cm}^2/\mathrm{s})$
D_{Ar-H2O}	$(5.721 * 10^{-9} * T^{1.5})/\left(p * 9.87 * 10^{-6} * \Omega(0.003178 * T)\right)(\mathrm{cm}^2/\mathrm{s})$
D_{N2-O2}	$(3.815 * 10^{-9} * T^{1.5})/\left(p * 9.87 * 10^{-6} * \Omega(0.00942 * T)\right)(\mathrm{cm}^2/\mathrm{s})$
D_{N2-H2O}	$(5.641 * 10^{-9} * T^{1.5})/\left(p * 9.87 * 10^{-6} * \Omega(0.00352 * T)\right)(\mathrm{cm}^2/\mathrm{s})$
D_{N2-H2O}	$(5.936 * 10^{-9} * T^{1.5})/\left(p * 9.87 * 10^{-6} * \Omega(0.00331 * T)\right)(\mathrm{cm}^2/\mathrm{s})$

Boundaries AB, BC and CD (Figure 4.10a) are open boundaries with mole fractions for N_2, O_2 and H_2O equal to 0.78084, 0.20947, and 0.00035; this is the composition of atmospheric air. For the walls of the device the no flux boundary condition applies.

The k-ω turbulent model uses wall functions as well, since we are not interested in the details of the flow at the walls. Furthermore, the same problem is also solved with a laminar flow model inside the device and a k-ε model outside the device. The velocity field at the nozzle exit from the laminar model is used as the inlet boundary condition for the k-ε model.

The results for the three different models are shown in Figures 4.12-4.16. In particular, the surface averaged values (left) and the on-axis (right) values of the axial velocity and the species densities are shown. The 'average' quantities are averaged inside a cylinder element of radius $r = 0.00075$ (m), i.e. equal to the radius of the nozzle exit. As far as the average (Figure 4.12, left) and the on-axis (Figure 4.12, right) velocities are concerned, both k-ε and k-ω models calculate slightly higher velocities than the laminar & k-ε model. The k-ε and k-ω velocities are very close at distances less than 1 cm from the nozzle but then start to deviate for longer distances (k-ω computes higher velocities). The on-axis velocity computed by the laminar & k-ε model has a different profile close to the nozzle than the other two models (k-ε and k-ω compute an almost flat velocity profile near the nozzle exit of the device).

Computers from the computer cluster Nessie [73] of the Institute of Nanoscience and Nanotechnology of NCSR "Demokritos" were utilized for these 2d fluid simulations.

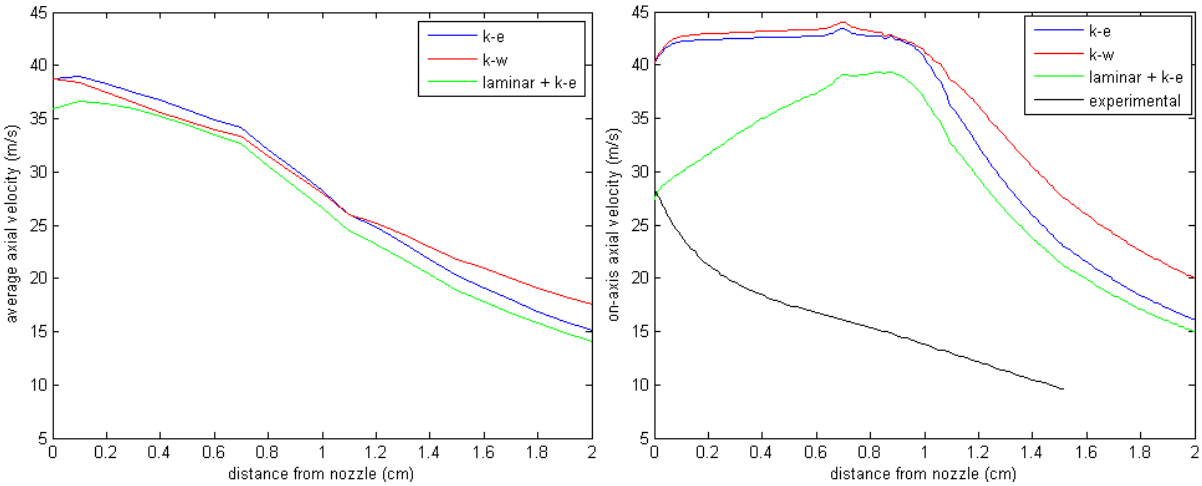

Figure 4.12: Average axial velocity (left) and on-axis axial velocity (right) for the three models (experimental data are also included for the on-axis velocity [41]).

Experimental data are also included in Figures 4.12-4.16 for the on-axis quantities [41]. There are no significant differences among the models regarding the species densities (Figures 4.13-4.16) except for H2O, which has a significantly lower density when computed with the laminar & k-ε model at distances less than 0.5 cm from the nozzle, compared with the other two models.

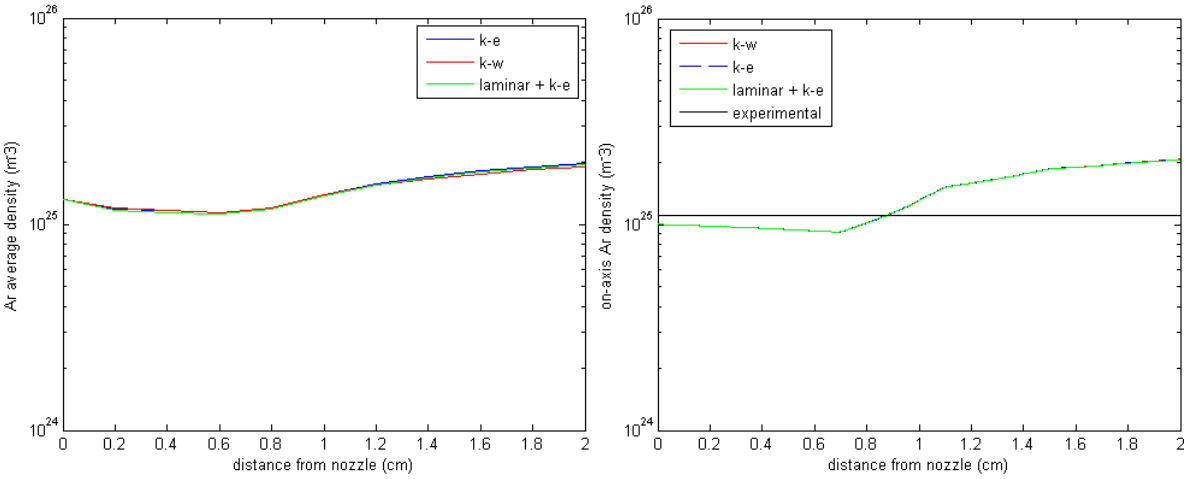

Figure 4.13: Average Argon density (left) and on-axis Argon density (right) for the three models (experimental data are also included for the on-axis Ar density [41]).

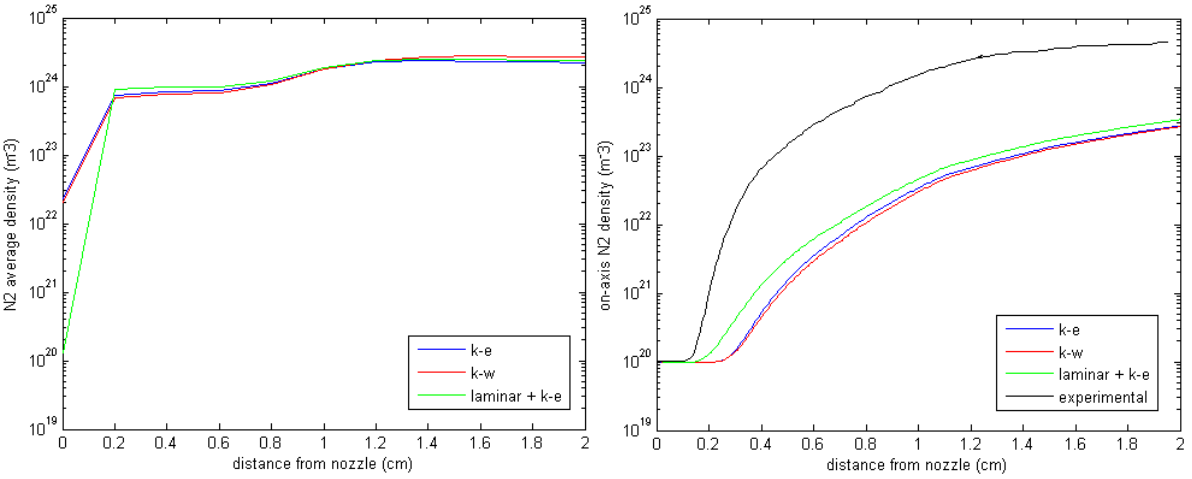

Figure 4.14: Average Nitrogen density (left) and on-axis Nitrogen density (right) for the three models (experimental data are also included for the on-axis N_2 density [41]).

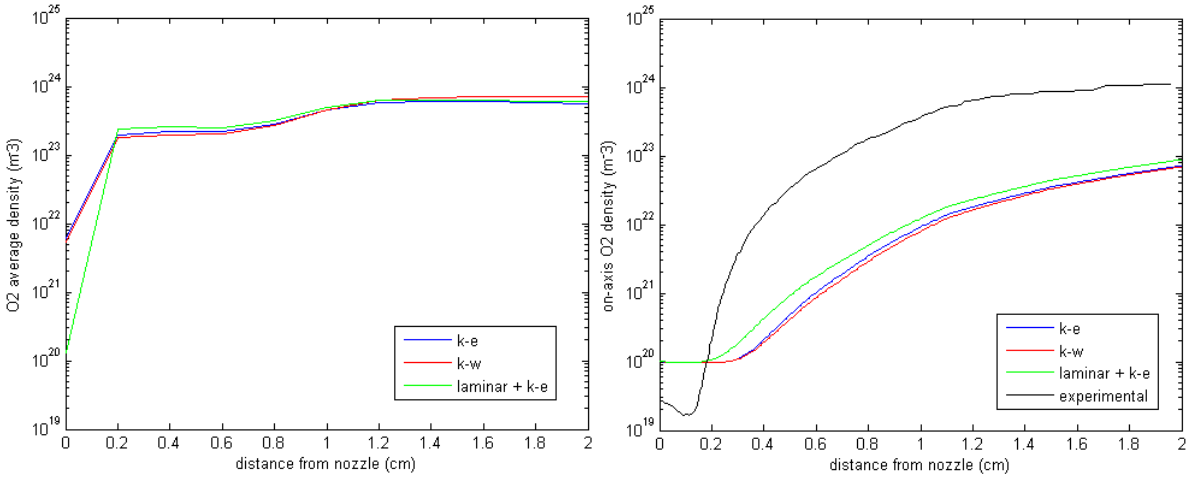

Figure 4.15: Average Oxygen density (left) and on-axis Oxygen density (right) for the three models (experimental data are also included for the on-axis O_2 density [41]).

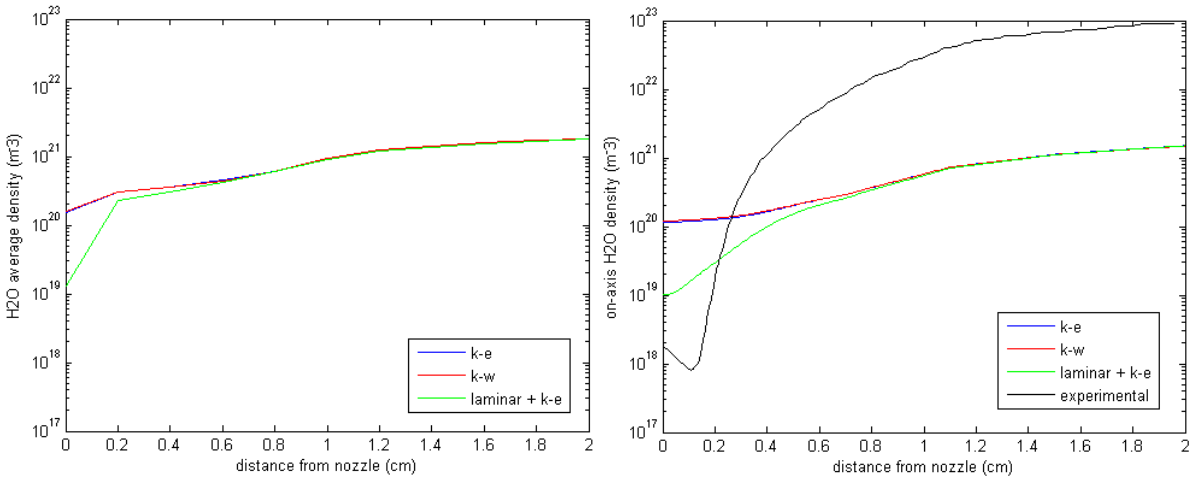

Figure 4.16: Average water vapor density (left) and on-axis water vapor density (right) for the three models (experimental data are also included for the on-axis H_2O density [41]).

Finally, a fully laminar 2d model does not compute correctly the average and on-axis flow velocities (Figure 4.17) since they remain almost constant as the distance from the nozzle increases. The fact that a fully laminar 2d model (Navier-Stokes equations without turbulence modeling) does not predict correctly the turbulent flow is more than expected because turbulence is a three dimensional phenomenon and the turbulent eddies cannot be captured by a 2d model (see section 4.2). As a result, if one wishes to solve directly the Navier-Stokes equations, i.e. to perform DNS, a 3d geometry should be utilized. An attempt for DNS was made but this required an extremely fine mesh that had a very high computational cost. When the mesh was not fine enough there was no convergence. So, in this work, no results were obtained by 3d DNS.

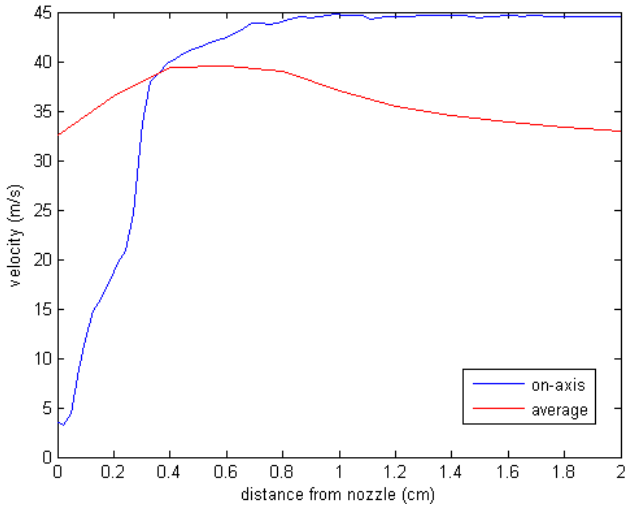

Figure 4.17: On-axis and average velocity for the fully laminar model.

A direct comparison of the results presented in this chapter with the experimental data of [30] is not possible since there are many aspects of the conditions of the experiment that are not fully clarified (e.g. exact geometry of the device, temperature distribution inside the device) and as a result, some assumptions were made in order to produce the results presented in this chapter. This is the reason why the experimental profiles of the velocity and the density (of Ar, N_2, O_2, and H_2O) were used as inputs in the global plasma model instead of the computed (by the turbulent models) profiles. However, this methodology can serve as a starting step in an effort to evaluate the velocity and density profiles which are required as inputs to the global model, without the need for experimental data information. Provided that the conditions of the experiment are fully available, one can improve these 2d simulations in order to accurately predict the gas velocity and Ar, N_2, O_2 and H_2O density profiles.

5. CONCLUSIONS

The first set of conclusions refers to the EEDF of Ar atmospheric pressure plasmas and the effects of composition and temperature on the EEDF:

a) There are discrepancies between the calculated EEDFs with a Boltzmann equation solver and the Maxwell or Druyvesteyn distribution (for the same mean electron energies).

b) The calculated EEDFs (with the Boltzmann equation solver) are more consistent with the Maxwell and Druyvesteyn distributions for lower electron energies.

c) For higher mean electron energies, the EEDF becomes less sensitive to the gas composition and tends to move away from the Maxwell distribution.

d) The gas temperature at the range of 400-600 K does not affect the calculated EEDFs except for very low mean electron energies with a higher Ar mole fraction.

The second set of conclusions refers to the comparison of results of the extended global model (πlasma-R) with the simulation results of Gaens & Bogaerts [30].

a) The results of the extended model, i.e. species densities and electron temperature, were close to those presented by Gaens&Bogaerts.

b) The frequent calculation of the EEDF with a Boltzmann equation solver can give more accurate results.

c) The results obtained from the calculated EEDFs were generally closer to the ones produced by Gaens&Bogaerts than those obtained by utilizing a Maxwell distribution.

d) The calculated electron temperature with a Maxwell EEDF deviated significantly from the one with calculated EEDFs.

e) The differences in the calculated species densities between the two methods (Maxwell distribution and calculated EEDFs) were more subtle.

The third set of conclusions refers to the fluid simulations of the atmospheric pressure plasma jet:

a) A direct numerical simulation (DNS) of a turbulent fluid flow has an increased computational cost, even at low Reynolds numbers.

b) The k-ε and k-ω models calculate slightly higher velocities than the combined laminar&k-ε model (laminar inside the device, k-εmodel outside the device).

c) The velocity profile along the jet coming from k-ε and k-ω turbulent models are very close at distances less than 1 cm from the nozzle exit but then start to deviate for longer distances (k-ω computes higher velocities).

d) The on-axis velocity computed by the combined laminar&k-ε model has a different profile close to the nozzle exit than the other two models (k-ε and k-ω compute an almost flat velocity profile near the nozzle exit of the device).

e) There are no significant differences among the models regarding the species densities except for H_2O, which has a significantly lower density when computed with the laminar&k-ε model at distances less than 0.5 cm from the nozzle, compared with the other two models.

f) A fully laminar 2d model did not compute correctly the average and on-axis flow velocities: The velocities remain almost constant as the distance from the nozzle increases.

g) The velocity profile coming from the turbulent flow models is not close to the measurement [41] of the flow velocity. This deviation can be attributed to differences in the geometry and the conditions between the experiment and the simulation, as well as to the use of specific turbulent models: It is possible that the use of other turbulent models will yield into improved results.

The proposed future works are summarized below:

a) Integration of a Boltzmann equation solver in the extended global model (πlasma-R). This will allow the frequent calculation of the EEDF and will improve the results.

b) Development of a self-consistent model for atmospheric pressure plasma jets which will decouple the plasma and fluid calculations. The extended global model will be used for the calculation of species densities and a turbulent flow model will be used for the calculation of the velocity field; mass balances will be solved for the dominant species (feed gas, N_2, O_2, and H_2O). Finally, an energy balance is required for the calculation of the gas temperature which is critical not only for the flow and plasma calculations but also for the practical applications of plasma jets.

c) The extended model can be also utilized for the simulation of low pressure plasma reactors in the transient state and facilitates studies in pulsed plasmas.

d) Full adaptation of πlasma-R interface to problems of atmospheric pressure plasma jets (it is now user friendly only for low pressure plasmas). Even if it is not self-consistent for the moment, due to its low computational cost compared to detailed multidimensional plasma models (a run with πlasma-R lasts for few seconds), and the user-friendly interface, πlasma-R can become an invaluable tool for rough but fast predictions of the species generated by atmospheric plasma jet devices. It is quite easy to study the effect of the power, the feed composition, the ambient air humidity, and the distance from the nozzle on the species densities, and optimize the conditions to deliver the desired density for the critical species either for agriculture or for medical and surface activation applications.

ABBREVIATIONS

APPJ	Atmospheric Pressure Plasma Jet
EEDF	Electron Energy Distribution Function
ΠΤΤΑΠ	Πλάσμα Τύπου Τζετ σε Ατμοσφαιρική Πίεση
ΚΕΗ	Κατανομή Ενέργειας Ηλεκτρονίων
DNS	Direct Numerical Simulation

APPENDIX A

Any ODE of order N can be represented as a first-order ODE. This is possible with the introduction of additional auxiliary variables $z_1(t) = y(t), z_2(t) = y^{'}, z_N(t) = y^{(N-1)}(t)$ as follows:

$$y^{(N)}(t) = f\left(t, y(t), y^{'}(t), \dots, y^{(N-1)}(t)\right) \ (Eq.A2.1)$$

$$z^{'}(t) = \begin{pmatrix} z_1^{'}(t) \\ . \\ . \\ z_{N-1}^{'}(t) \\ z_N^{'}(t) \end{pmatrix} = \begin{pmatrix} y^{'}(t) \\ . \\ . \\ y^{(N-1)}(t) \\ y^{(N)}(t) \end{pmatrix} = \begin{pmatrix} z_2(t) \\ . \\ . \\ z_N(t) \\ f\left(t, z_1(t), \dots, z_N(t)\right) \end{pmatrix} \ (Eq.A2.2)$$

which is a first order ODE system in the varible $z(t)$ [43, 44].

The family of explicit Runge–Kutta methods is a generalization of the RK4 method [46]. It is given by:

$$y_{n+1} = y_n + \sum_{i=1}^{s} h b_i k_i \ (Eq.A2.3)$$

where,

$$k_1 = f(t_n, y_n)$$

$$k_2 = f\left(t_n + c_2 h, y_n + h(a_{21} k_1)\right)$$

$$k_3 = f\left(t_n + c_3 h, y_n + h(a_{31} k_1 + a_{32} k_2)\right) \ (Eqs.A2.4)$$

.

$$k_s = f\left(t_n + c_s h, y_n + h\left(a_{s1} k_1 + a_{s2} k_2 + \cdots + a_{s,s-1} k_{s-1}\right)\right)$$

An implicit Runge–Kutta method has the form [47, 55]:

$$y_{n+1} = y_n + \sum_{i=1}^{s} b_i k_i \ (Eq.A2.5)$$

$$k_i = hf\left(t_n + c_i h, y_n + \sum_{j=1}^{s} a_{ij} k_j\right) \ (Eq.A2.6)$$

$$i = 1, \dots, s$$

The Lagrange formula for polynomial interpolation yields:

$$p(t) = \sum_{j=0}^{s-1} \frac{(-1)^{s-j-1} f\left(t_{n+j}, y_{n+j}\right)}{j!\,(s-j-1)!\,h^{s-1}} \prod_{\substack{i=0 \\ i \neq j}}^{s-1} (t - t_{n+i}) \ (Eq.A2.7)$$

The polynomial p is locally a good approximation of the right-hand side of the differential equation $y' = f(t, y)$ that is to be solved, so the equation $y' = p(t)$ is considered instead. This equation can be solved exactly; the solution is simply the integral of p [43, 44, 55]. This suggests taking

$$y_{n+s} = y_{n+s-1} + \int_{t_{n+s-1}}^{t_{n+s}} p(t)dt \ \ (Eq. A2.8)$$

The Adams–Bashforth method arises when the formula for p is substituted. The coefficients b_j turn out to be given by:

$$b_{s-j-1} = \frac{(-1)^j}{j!\,(s-j-1)!} \int_0^1 \prod_{\substack{i=0 \\ i \neq j}}^{s-1} (u+i)du \ \ (Eq. A2.9)$$

$$j = 0, \ldots, s-1$$

Replacing $f(t, y)$ by its interpolant p incurs an error of order h^s, and it follows that the s-step Adams–Bashforth method has indeed order s [43, 44, 55].

The derivation of the Adams–Moulton methods is similar to that of the Adams–Bashforth method; however, the interpolating polynomial uses not only the points $t_{n-1}, \ldots, t_{n-s}$, as above, but also t_n. The coefficients are given by [44, 50]:

$$b_{s-j} = \frac{(-1)^j}{j!\,(s-j)!} \int_0^1 \prod_{\substack{i=0 \\ i \neq j}}^{s} (u+i-1)du \ (Eq. A2.10)$$

$$j = 0, \ldots, s$$

Consider the linear constant coefficient inhomogeneous system $\boldsymbol{y}' = \boldsymbol{A}\boldsymbol{y} + \boldsymbol{f}(x)$, where $\boldsymbol{y}, \boldsymbol{f} \epsilon R^n$ and $\boldsymbol{A}$ is a constant nxn matrix with eigenvalues $\lambda_t \, \epsilon C, \ t = 1,2, \ldots, n$ and corresponding eigenvectors $c_t \, \epsilon C^n, \ t = 1,2, \ldots, n$. The general solution of this system takes the form:

$$\boldsymbol{y}(x) = \sum_{t=1}^{n} k_t exp(\lambda_t x)\boldsymbol{c}_t + \boldsymbol{g}(x) \ \ (Eq. A2.11)$$

where the k_t are arbitrary constants and $g(x)$ is a particular integral. If $Re(\lambda_t) < 0, t = 1,2, \ldots, n$ which implies that each of the terms $exp(\lambda_t x)\boldsymbol{c}_t \to 0$ as $x \to \infty$, so that the solution $y(x)$ approaches $g(x)$ asymptotically as $x \to \infty$. The term $exp(\lambda_t x)\boldsymbol{c}_t$ will decay monotonically if λ_t is real and sinusoidally if λ_t is complex. Interpreting x to be time (as it often is the case in physical problems) it is appropriate to call $\sum_{t=1}^{n} k_t exp(\lambda_t x)\boldsymbol{c}_t$ the transient solution and $g(x)$ the steady-state solution. If $|Re(\lambda_t)|$ is large, then the corresponding term $k_t exp(\lambda_t x)\boldsymbol{c}_t$ will decay quickly as x increases and is thus called a fast transient; if $|Re(\lambda_t)|$ is small, the corresponding term $k_t exp(\lambda_t x)\boldsymbol{c}_t$ decays slowly and is called a slow transient. Let $\overline{\lambda}, \underline{\lambda}$ be defined by $\left|Re\left(\overline{\lambda}\right)\right| \geq |Re(\lambda_t)| \geq \left|Re\left(\underline{\lambda}\right)\right|$ so that $k_t exp\left(\overline{\lambda} x\right)\boldsymbol{c}_t$ is the fastest transient and $k_t exp\left(\underline{\lambda} x\right)\boldsymbol{c}_t$ the slowest. The stiffness ratio is defined as $\left|Re\left(\overline{\lambda}\right)\right| / \left|Re\left(\underline{\lambda}\right)\right|$ [52].

A Runge–Kutta method applied to the test equation $y' = \lambda y$ reduces to the iteration $y_{n+1} = r(hk)y_n$, with r given by

$$r(z) = 1 + zb^T(I - zA)^{-1}e = \frac{det(I - zA + zeb^T)}{det(I - zA)} \ (Eq. A2.12)$$

where e stands for the vector of ones. The function r is called the stability function [74]. It follows from the formula that r is the quotient of two polynomials of degree s if the method has s stages. Explicit methods have a strictly lower triangular matrix $\boldsymbol{A}$, which implies that $det(\boldsymbol{I} - z\boldsymbol{A}) = 1$ and that the stability function is a polynomial. The numerical solution to the linear test equation decays to zero if $|r(z)| < 1$ with $z = h\lambda$. The method is said to be A-stable if all z with $Re(z) < 0$ are in the domain of absolute stability and since the stability function of an explicit Runge–Kutta method is a polynomial, explicit Runge–Kutta methods can never be A-stable [55].

Linear multistep methods have the form:

$$y_{n+1} = \sum_{i=0}^{s} a_i y_{n-1} + h \sum_{j=-1}^{s} b_j f\left(t_{n-j}, y_{n-j}\right) \ (Eq. A2.13)$$

and applied to the test equation, they become:

$$y_{n+1} = \sum_{i=0}^{s} a_i y_{n-1} + hk \sum_{j=-1}^{s} b_j y_{n-j} \ (Eq. A2.14)$$

which can be simplified to:

$$(1 - b_{-1}z)y_{n+1} - \sum_{j=0}^{s}\left(a_j + b_j z\right)y_{n-j} = 0 \ (Eq. A2.15)$$

where $z = h\lambda$. This is a linear recurrence relation. The method is A-stable if all solutions $\{y_n\}$ of the recurrence relation converge to zero when $Re(z) < 0$. The characteristic polynomial is:

$$\Phi(z, w) = w^{s+1} - \sum_{i=0}^{s} a_i w^{s-i} - z \sum_{j=-1}^{s} b_j w^{s-j} \ (Eq. A2.16)$$

All solutions converge to zero for a given value of z if all solutions w of $\Phi(z, w) = 0$ lie in the unit circle. The region of absolute stability for a multistep method of the above form is then the set of all $z \epsilon C$ for which all w such that $\Phi(z, w) = 0$ satisfy $|w| < 1$. Again, if this set contains the left-half plane, the multi-step method is said to be A-stable. Determining the region of absolute stability for the two-step Adams–Bashforth method [54]:

$$y_{n+1} = y_n + h\left(\frac{3}{2}f(t_n, y_n) - \frac{1}{2}f(t_{n-1}, y_{n-1})\right) \ (Eq. A2.17)$$

The characteristic polynomial is:

$$\Phi(w,z) = w^2 - \left(1+\frac{3}{2}z\right)w + \frac{1}{2}z = 0 \quad (Eq.A2.18)$$

which has roots:

$$w = \frac{1}{2}\left(1+\frac{3}{2}z \pm \sqrt{1+z+\frac{9}{4}z^2}\right) \ (Eq.A2.19)$$

thus the region of absolute stability is:

$$\left\{z \in \mathbb{C}: \left|\frac{1}{2}\left(1+\frac{3}{2}z \pm \sqrt{1+z+\frac{9}{4}z^2}\right)\right| < 1\right\} \ (Eq.A2.20)$$

APPENDIX B

Table B1: Set of electron impact reactions and reactions between heavy species. The reaction coefficients are taken from Gaens&Bogaerts [30] unless stated otherwise in the "Comments" column. M denotes third body (external sources: [75-79]).

	Electron impact collisions	Comments
1	e + Ar --> Ar + e	
2	e + Ar --> Ar(3p2) + e	
3	e + Ar --> Ar(3p1) + e	
4	e + Ar --> Ar(3p0) + e	
5	e + Ar --> Ar(1p1) + e	
6	e + Ar --> Ar(4p) + e	
7	e + Ar --> Ar(4p) + e	
8	e + Ar --> Ar(4p) + e	
9	e + Ar --> Ar(4p) + e	
10	e + Ar --> Ar+ + 2e	
11	e + Ar(3p2) --> Ar(3p1) + e	
12	e + Ar(3p2) --> Ar(4p) + e	[threshold reduced and scaled]
13	e + Ar(3p2) -->Ar(4p) + e	[threshold reduced and scaled]
14	e + Ar(3p2) --> Ar(4p) + e	[threshold reduced and scaled]
15	e + Ar(3p2) --> Ar(4p) + e	[threshold reduced and scaled]
16	e + Ar(3p2) --> Ar+ + 2e	
17	e + Ar(3p1) --> Ar(3p2) + e	
18	e + Ar(3p1) --> Ar+ + 2e	
19	e + Ar(3p0) -->Ar(1p1) + e	
20	e + Ar(3p0) --> Ar(4p) + e	[threshold reduced and scaled]
21	e + Ar(3p0) --> Ar(4p) + e	[threshold reduced and scaled]
22	e + Ar(3p0) --> Ar(4p) + e	[threshold reduced and scaled]
23	e + Ar(3p0) --> Ar(4p) + e	[threshold reduced and scaled]
24	e + Ar(3p0) --> Ar+ + 2e	
25	e + Ar(4p) --> Ar(3p0) + e	[detailed balancing]
26	e + Ar(4p) --> Ar(3p0) + e	[detailed balancing]
27	e + Ar(4p) --> Ar(3p0) + e	[detailed balancing]
28	e + Ar(4p) --> Ar(3p0) + e	[detailed balancing]
29	e + Ar(4p) --> Ar+ + 2e	
30	e + Ar(4p) --> Ar+ + 2e	
31	e + Ar(4p) --> Ar+ + 2e	
32	e + Ar2(ex) --> Ar2+ + 2e	
33	e + Ar2+ --> Ar(4p) + Ar	
34	e + O --> O(1d) + e	
35	e + O --> O+ + 2e	
36	e + O- --> O + 2e	
37	e + O2 --> O2 + e	
38	e + O2 --> O2(r) + e	
39	e + O2 --> O2(v) + e	
40	e + O2 --> O2(v) + e	
41	e + O2 --> O2(v) + e	

42	e + O2 --> O2(v) + e	
43	e + O2 --> O2(v) + e	
44	e + O2 --> O2(v) + e	
45	e + O2 --> O2(a) + e	
46	e + O2 --> O2(b) + e	
47	e + O2 --> O2+ + 2e	
48	e + O2 --> O + O + e	
49	e + O2 --> O + O + e	
50	e + O2 --> O+ + O + 2e	
51	e + O2 --> O- + O	
52	e + O2 + O2 --> O2- + O2	
53	e + O2 + N2 --> O2- + N2	
54	e + O2 + Ar --> O2- + Ar	
55	e + O2(a) --> O + O + e	
56	e + O2(a) --> O + O + e	
57	e + O2(a) --> O- + O	
58	e + O2(a) --> O2 + e	
59	e + O2(a) --> O2(b) + e	
60	e + O2(a) --> O2+ + 2e	
61	e + O2(a) --> O2-	
62	e + O2(b) --> O + O + e	[threshold reduced]
63	e + O2(b) --> O + O + e	[threshold reduced]
64	e + O2(b) --> O- + O	[threshold reduced from O2(a)]
65	e + O2(b) --> O2(a) + e	
66	e + O2+ --> O + O	
67	e + O3 --> O + O2 + e	
68	e + O3 --> O- + O2	
69	e + O3 --> O + O2-	
70	e + N --> e + N(2d)	[56]
71	e + N(2d) --> e + N	
72	e + N2 --> N2 + e	
73	e + N2 --> e + N2(r)	
74	e + N2 --> e + N2(v)	
75	e + N2 --> e + N2(v)	
76	e + N2 --> e + N2(v)	
77	e + N2 --> e + N2(v)	
78	e + N2 --> e + N2(v)	
79	e + N2 --> e + N2(v)	
80	e + N2 --> e + N2(v)	
81	e + N2 --> e + N2(v)	
82	e + N2 --> e + N2(ac)	
83	e + N2 --> e + N2(aa)	
84	e + N2 --> e + N + N	
85	e + N2 --> N+ + N + 2e	
86	e + N2 --> N2+ + 2e	
87	e + N2(v) --> N2(ac) + e	[threshold reduced and scaled]
88	e + N2(v) --> N2(ac) + e	[threshold reduced and scaled]
89	e + N2(v) --> N2(ac) + e	[threshold reduced and scaled]

90	e + N2(v) --> N2(ac) + e	[threshold reduced and scaled]
91	e + N2(v) --> N2(ac) + e	[threshold reduced and scaled]
92	e + N2(v) --> N2(ac) + e	[threshold reduced and scaled]
93	e + N2(v) --> N2(ac) + e	[threshold reduced and scaled]
94	e + N2(v) --> N2(ac) + e	[threshold reduced and scaled]
95	e + N2(ac) --> N2 + e	
96	e + N2(ac) --> N2(v) + e	
97	e + N2(ac) --> N2(v) + e	
98	e + N2(ac) --> N2(v) + e	
99	e + N2(ac) --> N2(v) + e	
100	e + N2(ac) --> N2(v) + e	
101	e + N2(ac) --> N2(v) + e	
102	e + N2(ac) --> N2(v) + e	
103	e + N2(ac) --> N2(v) + e	
104	e + N2(ac) --> N2+ + 2e	[57]
105	e + N2(aa) --> N2 + e	
106	e + N2+ --> N + N	
107	e + NO --> N + O + e	[58]
108	e + NO --> N + O-	
109	e + NO --> NO+ + 2e	
110	e + NO+ --> N + O	
111	e + NO+ --> N(2d) + O	
112	e + NO2 --> NO2+ + 2e	
113	e + NO2 --> NO + O + e	
114	e + NO2+ --> NO + O	
115	e + NO2+ --> NO + O(1d)	
116	e + N2O --> N2O(v) + e	[59]
117	e + N2O --> N2O(v) + e	[59]
118	e + N2O --> N2O(v) + e	[59]
119	e + H --> H(ex) + e	[60]
120	e + H --> H(ex) + e	[60]
121	e + H --> H(ex) + e	[60]
122	e + H --> H+ + 2e	[60]
123	e + H(ex) --> H + e	
124	e + H(ex) --> H + e	
125	e + H(ex) --> H + e	
126	e + H(ex) --> H+ + 2e	
127	e + H(ex) --> H+ + 2e	
128	e + H(ex) --> H+ + 2e	
129	e + H- --> H + 2e	
130	e + H2 --> H2(r) + e	
131	e + H2 --> H2(r) + e	
132	e + H2 --> H2(v) + e	
133	e + H2 --> H2(ex) + e	
134	e + H2 --> H2(ex) + e	
135	e + H2 --> H2+ + 2e	
136	e + H2(ex) --> H2 + e	
137	e + H2(ex) --> H2 + e	

138	e + H2(ex) --> H2+ + 2e	
139	e + H2(ex) --> H2+ + 2e	
140	e + H2+ --> H+ + H + e	[60]
141	e + OH --> O + H + e	
142	e + OH --> OH(ac) + e	
143	e + OH --> OH+ + 2e	
144	e + OH(ac) --> OH+ + 2e	
145	e + OH(ac) --> O + H + e	
146	e + OH+ --> O + H	
147	e + OH- --> OH + 2e	
148	e + H2O --> H2O + e	
149	e + H2O --> H2O(v) + e	
150	e + H2O --> H2O(v) + e	
151	e + H2O --> O- + H2	
152	e + H2O --> OH + H-	
153	e + H2O --> OH- + H	
154	e + H2O --> OH + H + e	
155	e + H2O --> H2O+ + 2e	
156	e + H2O+ --> O + H2	
157	e + H2O+ --> O + H + H	
158	e + H2O+ --> OH + H	
159	e + H3O+ --> OH + H + H	
160	e + H3O+ --> H2O + H	
161	e + H3O+ --> OH + H2	
162	e + H2O2 --> H2O + O-	
163	e + H2O2 --> OH + OH-	
	Argon heavy particle collisions	
164	Ar(3p2) + Ar2(ex) --> Ar+ + Ar + Ar +	
165	Ar(3p2) + Ar + M --> Ar2(ex) + M	
166	Ar(3p1) + Ar + M --> Ar2(ex) + M	
167	Ar(3p0) + Ar + M --> Ar2(ex) + M	
168	Ar(1p1) + Ar + M --> Ar2(ex) + M	
169	Ar(4p) + Ar + M --> Ar2(ex) + M	
170	Ar+ + Ar + M --> Ar2+ + M	
171	Ar2(ex) +Ar2(ex) --> Ar2+ + Ar + Ar +	
172	Ar2(ex) + Ar --> Ar + Ar + Ar	
173	Ar2(ex) + O2 --> Ar + Ar + O2	
174	Ar2(ex) + N2 --> Ar + Ar + N2	
175	Ar2(ex) + H2O --> Ar + Ar + H2O	
176	Ar2(ex) + H2 --> Ar + Ar + H2	
177	Ar2(ex) + O3 --> Ar + Ar + O3	
178	Ar2(ex) + Ar --> Ar(3p2) + Ar + Ar	
179	Ar2(ex) + O2 --> Ar(3p2) + Ar + O2	
180	Ar2(ex) + N2 --> Ar(3p2) + Ar + N2	
181	Ar2(ex) + H2O --> Ar(3p2) + Ar + H2O	
182	Ar2(ex) + H2 --> Ar(3p2) + Ar + H2	
183	Ar2(ex) + O3 --> Ar(3p2) + Ar + O3	
184	Ar2(ex) + Ar --> Ar(3p1) + Ar + Ar	

185	Ar2(ex) + O2 --> Ar(3p1) + Ar + O2	
186	Ar2(ex) + N2 --> Ar(3p1) + Ar + N2	
187	Ar2(ex) + H2O --> Ar(3p1) + Ar +	
188	Ar2(ex) + H2 --> Ar(3p1) + Ar + H2	
189	Ar2(ex) + O3 --> Ar(3p1) + Ar + O3	
190	Ar2(ex) + Ar --> Ar(3p0) + Ar + Ar	
191	Ar2(ex) + O2 --> Ar(3p0) + Ar + O2	
192	Ar2(ex) + N2 --> Ar(3p0) + Ar + N2	
193	Ar2(ex) + H2O --> Ar(3p0) + Ar +	
194	Ar2(ex) + H2 --> Ar(3p0) + Ar + H2	
195	Ar2(ex) + O3 --> Ar(3p0) + Ar + O3	
196	Ar2(ex) + Ar --> Ar(1p1) + Ar + Ar	
197	Ar2(ex) + O2 --> Ar(1p1) + Ar + O2	
198	Ar2(ex) + N2 --> Ar(1p1) + Ar + N2	
199	Ar2(ex) + H2O --> Ar(1p1) + Ar +	
200	Ar2(ex) + H2 --> Ar(1p1) + Ar + H2	
201	Ar2(ex) + O3 --> Ar(1p1) + Ar + O3	
	Argon-dry air heavy particle	
202	Ar(3p2) + O2 --> Ar + O + O	
203	Ar(3p2) + O2(a) --> Ar + O + O	
204	Ar(3p2) + N(2d) --> Ar + N+ + e	
205	Ar(3p2) + N2 --> Ar + N2(ac)	
206	Ar(3p2) + N2 --> Ar + N + N	
207	Ar(3p2) + N2(ac) --> Ar + N2+ + e	
208	Ar(3p1) + O2 --> Ar + O + O	
209	Ar(3p1) + N2 --> Ar + N2(ac)	
210	Ar(3p1) + N2 --> Ar + N + N	
211	Ar(3p1) + N2(ac) --> Ar + N2+ + e	
212	Ar(3p0) + O2 --> Ar + O + O	
213	Ar(3p0) + N2 --> Ar + N2(ac)	
214	Ar(3p0) + N2 --> Ar + N + N	
215	Ar(3p0) + N2(ac) --> Ar + N2+ + e	
216	Ar(1p1) + O2 --> Ar + O + O	
217	Ar(1p1) + N2 --> Ar + N2(ac)	
218	Ar(1p1) + N2 --> Ar + N + N	
219	Ar(4p) + O2 --> Ar + O + O	
220	Ar(4p) + O2(a) --> Ar + O + O	
221	Ar(4p) + N2 --> Ar + N2(ac)	
222	Ar(4p) + N2 --> Ar + N + N	
223	Ar(4p) + N2(ac) --> Ar + N2+ + e	
224	Ar(4p) + NO --> Ar + N + O	
225	Ar(4p) + N2O --> Ar + NO + N	
226	Ar(4p) + N2O --> Ar + N2(ac) + O	
227	Ar+ + O --> Ar + O+	
228	Ar+ + O2 --> Ar + O2+ :	
229	Ar+ + N2 --> Ar + N2+	
230	Ar+ + N2 --> Ar + N+ + N	
231	Ar2(ex) + O2 --> Ar + Ar + O + O	

232	Ar2(ex) + O3 --> Ar + Ar + O2 + O	
233	Ar2(ex) + N2 --> Ar + Ar + N2(ac)	
234	Ar2(ex) + NO --> Ar + Ar + N + O	
235	Ar2(ex) +NO2 --> Ar + Ar + NO + O	
236	Ar2(ex) + N2O --> Ar + Ar + N2 + O	
237	Ar2+ + O- --> Ar + Ar + O	
238	Ar2+ + O2 --> Ar +Ar + O2+	
239	Ar2+ + O2- --> Ar + Ar + O2	
240	Ar2+ + O2- --> Ar + Ar + O + O	
241	Ar2+ + O3 --> Ar + Ar + O2+ + O	
242	Ar2+ + NO --> Ar + Ar + NO+	
243	Ar2+ + NO2 --> Ar + Ar + NO+ + O	
244	Ar2+ + NO2 --> Ar + Ar + NO2+	
245	Ar2+ + NO2- --> Ar + Ar + NO2	
	Oxygen heavy particle collisions	
249	O + O + Ar --> O2 + Ar	
250	O + O + M --> O2(a) + M	
251	O + O + M --> O2(b) + M	
252	O + O+ + M --> O2+ + M	
253	O + O- --> O2 + e	
254	O + O2 + Ar --> O3 + Ar	
255	O + O2 + O2 --> O3 + O2	
256	O + O2 + N2 --> O3 + N2	
257	O + O2- --> O2 + O-	
258	O + O2- --> O3 + e	
259	O + O3 --> O2 + O2	
260	O + O3- --> O2- + O2	
261	O + O3- --> O2 + O2 + e	
262	O(1d) + O2 --> O2(a) + O	
263	O(1d) + O2 --> O2(b) + O	
264	O(1d) + O3 --> O2(a) + O2	
265	O(1d) + Ar --> Ar + O	
266	O(1d) + O2 --> O2 + O	
267	O(1d) + N2 --> N2 + O	
268	O(1d) + H2O --> H2O + O	
269	O(1d) + H2 --> H2 + O	
270	O(1d) + O3 --> O3 + O	
271	O+ + O- --> O + O	
272	O+ + O- + M --> O + O + M	
273	O+ + O2 --> O + O2+	
274	O+ + O3- + M --> O3 + O + M	
275	O- + O2 --> O2- + O	
276	O- + O2 + M --> O3- + M	
277	O- + O2(a) --> O3 + e	
278	O- + O2(a) --> O2- + O	
279	O- + O2+ --> O + O2	
280	O- + O2+ --> O + O + O	
281	O- + O2+ + M --> O + O2 + M	

282	O2 + O2+ + M --> O4+ + M	
283	O2(v) + N2 --> O2 + N2	
284	O2(v) + O2 --> O2 + O2	
285	O2(v) + Ar --> O2 + Ar	
286	O2(r) + N2 --> O2 + N2	
287	O2(r) + O2 --> O2 + O2	
288	O2(r) + Ar --> O2 + Ar	
289	O2(a) + O2(a) --> O2(b) + O2	
290	O2(a) + O2- --> O2 + O2 + e	
291	O2(a) + O3 --> O2 + O2 + O	
292	O2(a) + Ar --> O2 + Ar	
293	O2(a) + N2 --> O2 + N2	
294	O2(b) + H2O --> O2 + H2O	
295	O2(b) + O3 --> O2 + O3	
296	O2(b) + Ar --> O2 + Ar	
297	O2(b) + H2O --> O2(a) + H2O	
298	O2(b) + O3 --> O2(a) + O3	
299	O2(b) + Ar --> O2(a) + Ar	
300	O2+ + O2- + M --> O2 + O2 + M	
301	O2+ + O3- --> O3 + O2	
302	O2+ + O3- --> O2 + O + O2	
303	O2+ + O3- --> O2 + O + O + O	
304	O2+ + O3- + M --> O3 + O2 + M	
305	O2- + O3 --> O2 + O3-	
306	O2- + Ar --> O2 + e + Ar	
307	O2- + O2 --> O2 + e + O2	
308	O2- + N2 --> O2 + e + N2	
309	O2- + H2O --> O2 + e + H2O	
310	O2- + H2 --> O2 + e + H2	
311	O2- + O3 --> O2 + e + O3	
312	O3 + Ar --> O + O2 + Ar	
313	O3 + N2 --> O + O2 + N2	
314	O3 + O2 --> O + O2 + O2	
315	O4+ + Ar --> O2+ + O2 + Ar	
316	O4+ + O2 --> O2+ + O2 + O2	
317	O4+ + N2 --> O2+ + O2 + N2	
318	O4+ + H2O --> O2+ + O2 + H2O	
319	O4+ + H2 --> O2+ + O2 + H2	
320	O4+ + O3 --> O2+ + O2 + O3	
	Nitrogen heavy particle collisions	
321	N + N2+ + M --> N3+ + M	
322	N(2d) + Ar --> N + Ar	
323	N(2d) + O2 --> N + O2	
324	N(2d) + N2 --> N + N2	
325	N(2d) + H2O --> N + H2O	
326	N(2d) + H2 --> N + H2	
327	N(2d) + O3 --> N + O3	
328	N+ + N2 --> N + N2+	

329	N+ + N2 + M --> N3+ + M	
330	N2 + N2+ + M --> N4+ + M	
331	N2(r) + N2 --> N2 + N2	
332	N2(r) + O2 --> N2 + O2	
333	N2(r) + Ar --> N2 + Ar	
334	N2(v) + N2 --> N2 + N2	
335	N2(v) + O2 --> N2 + O2	
336	N2(v) + Ar --> N2 + Ar	
337	N2(ac) + N2(aa) --> N4+ + e	
338	N2(ac) + O2 --> N2 + O2	
339	N2(ac) + O --> N2 + O	
340	N2(ac) + NO --> N2 +NO	
341	N2(ac) + H --> N2 + H	
342	N2(ac) + H2O --> N2 +H2O	
343	N2(aa) + O --> N2 + O	
344	N2(aa) + H --> N2 + H	
345	N2(aa) + H2O --> N2 + H2O	
345	N2(aa) + H2O --> N2 + H2O	
346	N3+ + Ar --> Ar + N + N2+	
347	N3+ + O2 --> O2 + N + N2+	
348	N3+ + N2 --> N2 + N + N2+	
349	N3+ + H2O --> H2O + N + N2+	
350	N3+ + H2 --> H2 + N + N2+	
351	N3+ + O3 --> O3 + N + N2+	
352	N4+ + Ar --> Ar+ + N2 + N2	
	Dry air heavy particle collisions	
353	O + N + Ar --> NO + Ar	
354	O + N+ + M --> NO+ + M	
355	O + N2(ac) --> NO + N	
356	O + N2(ac) --> NO + N(2d)	
357	O + N2(aa) --> NO + N(2d)	
358	O + N2+ --> N + NO+	
359	O + N2+ --> N2 + O+	
360	O + N4+ --> N2 + N2 + O+	
361	O + NO + Ar --> NO2 + Ar	
362	O + NO + N2 --> NO2 + N2	
363	O + NO2 --> NO + O2	
364	O + NO2 + Ar --> NO3 + Ar	
365	O + NO2 + N2 --> NO3 + N2	
366	O + NO2 + O2 --> NO3 + O2	
367	O + NO2+ --> NO+ + O2	
368	O + NO2- --> NO3 + e	
369	O + NO3 --> NO2 + O2	
370	O + NO3- --> NO2 + O2-	
371	O + NO3- -->NO2- + O2	
372	O + NO3- --> NO2 + O2 + e	
373	O(1d) + NO --> O2 + N	
374	O+ + N(2d) --> N+ + O	

375	O+ + N2 + M --> NO+ + N + M	
376	O+ + NO2 --> NO2+ + O	
377	O+ + NO2- + M --> NO3 + M	
378	O- + N+ + M --> NO + M	
379	O- + N+ + M --> N + O + M	
380	O- + N2 --> N2O + e	
381	O- + N2(ac) --> N2 + O + e	
382	O- + N2+ + M --> N2 + O + M	
383	O- + N2+ + M --> N2O + M	
384	O- + NO --> NO2 + e	
385	O- + NO + M --> NO2- + M	
386	O- + NO+ --> O + NO	
387	O- + NO+ + M --> O + NO + M	
388	O- + NO+ + M --> NO2 + M	
389	O- + NO2 --> NO2- + O	
390	O- + NO2+ + M --> O + NO2 + M	
391	O- + NO2+ + M --> NO3 + M	
392	O2 + N --> NO + O	
393	O2 + N(2d) --> NO + O	
394	O2 + N(2d) --> NO + O(1d)	
395	O2 + N+ --> N + O2+	
396	O2 + N+ --> NO+ + O	
397	O2 + N+ --> NO + O+	
398	O2 + N2(ac) --> N2 + O + O	
399	O2 + N2(ac) --> N2 + O2(a)	
400	O2 + N2(ac) --> N2 + O2(b)	
401	O2 + N2(ac) --> N2O + O	
402	O2 + N2(ac) --> N2O + O(1d)	
403	O2 + N2(aa) --> N2 + O + O	
404	O2 + N2+ --> N2 + O2+	
405	O2 + N3+ --> NO+ + N2O	
406	O2 + N3+ --> NO2+ + N2	
407	O2 + N4+ --> N2 + N2 + O2+	
408	O2 + NO3 --> NO2 + O3	
409	O2(a) + N2(ac) --> N2 + O + O	
410	O2(b) + N2(ac) --> N2 + O + O	
411	O2+ + N --> NO+ + O	
412	O2+ + NO --> NO+ + O2	
413	O2+ + NO2 --> NO2+ + O2	
414	O2+ + NO2- --> NO2 + O2	
415	O2+ + NO2- --> NO2 + O + O	
416	O2+ + NO2- --> NO + O + O2	
417	O2+ + NO2- --> NO + O + O + O	
418	O2+ + NO2- + M --> NO2 + O2 + M	
419	O2+ + NO3- --> NO3 + O2	
420	O2+ + NO3- --> NO3 + O + O	
421	O2+ + NO3- --> NO2 + O + O2	
422	O2+ + NO3- --> NO2 + O + O + O	

423	O2+ + NO3- + M --> NO3 + O2 + M	
424	O2+ + N2O5 --> NO2+ + NO3 + O2	
425	O2- + N --> NO2 + e	
426	O2- + N2(ac) --> O2 + N2 +e	
427	O2- + NO+ + M --> NO3 + M	
428	O2- + NO+ + M --> O2 + NO + M	
429	O2- + NO2 --> NO2- + O2	
430	O2- + NO2+ --> NO2 + O2	
431	O2- + NO2+ + M --> O2 + NO2 + M	
432	O2- + NO3 --> NO3- + O2	
433	O3 + N2(ac) --> N2 + O2 + O	
434	O3 + N2(ac) --> NO + NO + O	
435	O3 + NO --> NO2 + O2	
436	O3 + NO2 --> NO3 + O2	
437	O3 + NO2 --> NO + O2 + O2	
438	O3 + NO2- --> NO3- + O2	
439	O3 + NO3- --> NO2- + O2 + O2	
440	O3- + N2+ + M --> O3 + N2 + M	
441	O3- + NO --> NO3- + O	
442	O3- + NO+ + M --> O3 + NO + M	
443	O3- + NO2 --> NO2- + O3	
444	O3- + NO2+ + M --> O3 + NO2 + M	
445	O3- + NO3 -->NO3- + O3	
446	N + NO --> N2 + O	
447	N + NO2 --> NO + NO	
448	N + NO2 --> N2O + O	
449	N + NO3 --> NO2 + NO	
450	N + NO3- --> NO2- + NO	
451	N(2d) + NO --> N2O	
452	N2(ac) + NO2 --> N2 + NO + O	
453	N2(ac) + N2O --> N2 + N2 + O	
454	N2(ac) + N2O --> N2 + N + NO	
455	N2(aa) + NO --> N2 + N + O	
456	NO + NO2 --> N2O3	
457	NO + NO2+ --> NO2 + NO+	
458	NO + NO3 --> NO2 + NO2	
459	NO+ + NO2- + M --> NO + NO2 + M	
460	NO+ + NO3- --> NO3 + N + O	
461	NO+ + NO3- --> NO2 + N + O + O	
462	NO+ + NO3- + M --> NO + NO3 + M	
463	NO+ + N2O5 --> NO2 + NO2 + NO2+	
464	NO2 + NO2 + Ar --> N2O4 + Ar	
465	NO2 + NO2 + N2 --> N2O4 + N2	
466	NO2 + NO2 + O2 --> N2O4 + O2	
467	NO2 + NO3 + Ar --> N2O5 + Ar	
468	NO2 + NO3 + N2 --> N2O5 + N2	
469	NO2 + NO3 + O2 --> N2O5 + O2	
470	NO2+ + NO3- + M --> N2O5 + M	

471	NO2+ + NO3- + M --> NO2 + NO3 + M	
472	NO2- + N2O --> NO3- + N2	
473	NO2- + NO3 --> NO3- + NO2	
474	NO2- + N2O5 --> NO3- + NO3 + NO	
475	N2O(v) + N2 --> N2O + N2	
476	N2O(v) + O2 --> N2O + O2	
477	N2O(v) + Ar --> N2O + Ar	
478	N2O3 + Ar --> NO + NO2 + Ar	
479	N2O3 + O2 --> NO + NO2 + O2	
480	N2O3 + N2 --> NO + NO2 + N2	
481	N2O3 + H2O --> NO + NO2 + H2O	
482	N2O3 + H2 --> NO + NO2 + H2	
483	N2O3 + O3 --> NO + NO2 + O3	
484	N2O4 + Ar --> NO2 + NO2 + Ar	
485	N2O4 + O2 --> NO2 + NO2 + O2	
486	N2O4 + N2 --> NO2 + NO2 + N2	
487	N2O4 + H2O --> NO2 + NO2 + H2O	
488	N2O4 + H2 --> NO2 + NO2 + H2	
489	N2O4 + O3 --> NO2 + NO2 + O3	
490	N2O5 + Ar --> NO2 + NO3 + Ar	
491	N2O5 + O2 --> NO2 + NO3 + O2	
492	N2O5 + N2 --> NO2 + NO3 + N2	
493	N2O5 + H2O --> NO2 + NO3 + H2O	
494	N2O5 + H2 --> NO2 + NO3 + H2	
495	N2O5 + O3 --> NO2 + NO3 + O3	
	Argon-humid air heavy particle collisions	
496	Ar(3p2) + OH --> Ar + OH(ac)	
497	Ar(3p2) + H2O --> Ar + OH + H	
498	Ar(3p1) + H2O --> Ar + OH + H	
499	Ar(3p0) + H2O --> Ar + OH + H	
500	Ar(4p) + H2 --> Ar + H + H	
501	Ar(4p) + H2O --> Ar + OH + H	
502	Ar+ + H --> Ar + H+	
503	Ar+ + H2 --> ArH+ + H	
504	Ar+ + H2 --> Ar + H2+	
505	Ar+ + H2O --> Ar + H2O+	
506	Ar+ + H2O --> ArH+ + OH	
507	Ar2(ex) + H2O --> Ar + Ar + OH +H	
508	Ar2+ + H --> Ar + Ar + H+	
509	Ar2+ + H- --> Ar + Ar + H	
510	Ar2+ + H2O --> Ar + Ar + H2O+	
511	Ar2+ + H2O --> ArH+ + Ar + OH	
512	Ar2+ + OH- --> Ar + Ar + OH	
513	Ar2+ + OH- --> Ar + Ar + O + H	
	Humid air heavy particle collisions	
514	H + O + Ar --> OH + Ar	
515	H + O+ --> H+ + O	
516	H + O- --> OH + e	

517	H + O2 + Ar --> HO2 + Ar	
518	H + O2 + N2 --> HO2 + N2	
519	H + O2 + O2 --> HO2 + O2	
520	H + O2- --> H- + O2	
521	H + O2- --> HO2 + e	
522	H + O3 --> OH + O2	
523	H + N + Ar --> NH + Ar	
524	H + N + N2 --> NH + N2	
525	H + N+ --> N + H+	
526	H + NO + Ar --> HNO + Ar	
527	H + NO + N2 --> HNO + N2	
528	H + NO2 --> OH + NO	
529	H + NO2+ --> OH + NO+	
530	H + NO2- --> HNO2 + e	
531	H + NO2- --> OH- + NO	
532	H + NO3 --> OH + NO2	
533	H + NO3- --> OH- + NO2	
534	H + NO3- --> HNO3 + e	
535	H + NO3- --> NO2- + OH	
536	H + H + Ar --> H2 + Ar	
537	H + H2+ --> H2 + H+	
538	H + OH + Ar --> H2O + Ar	
539	H +OH- --> H2O + e	
540	H + HO2 --> H2 + O2	
541	H + HO2 --> OH + OH	
542	H + HO2 --> H2O + O	
543	H + HO2 -->H2O + O(1d)	
544	H + H2O2 --> HO2 + H2	
545	H + H2O2 --> H2O + OH	
546	H + NH --> H2 + N	
547	H + HNO --> H2 + NO	
548	H + HNO2 --> H2 + NO2	
549	H + HNO2 --> HNO + OH	
550	H + HNO3 --> HNO2 + OH	
551	H + HNO4 --> HNO2 + HO2	
552	H + ArH+ --> H2+ + Ar	
553	H(ex) + N2 --> H + N2	
554	H(ex) + O2 --> H + O2	
555	H(ex) + Ar --> H + Ar	
556	H+ + O --> H + O+	
557	H+ + O- + M --> H + O + M	
558	H+ + O- + M --> OH + M	
559	H+ + O2 --> H + O2+	
560	H+ + O3- + M --> H + O3 + M	
561	H+ + N --> N+ + H	
562	H+ + NO --> NO+ + H	
563	H+ + NO3- + M --> HNO3 + M	
564	H+ + H2 + M --> H3+ + M	

565	H+ + OH --> H + OH+	
566	H+ + H2O --> H + H2O+	
567	H- + O --> OH + e	
568	H- + O2 --> HO2 + e	
569	H- + O2+ + M --> H + O2 + M	
570	H- + O2+ + M --> HO2 + M	
571	H- + NO+ + M --> HNO + M	
572	H- + NO2 --> NO2- + H	
573	H- + NO2+ + M --> HNO2 + M	
574	H- + H2O --> OH- + H2	
575	H- + H2O+ + M --> H + H2O + M	
576	H- + Ar --> H + e +Ar	
577	H- + O2 --> H + e +O2	
578	H- + N2 --> H + e +N2	
579	H- + H2O --> H + e +H2O	
580	H- + H2 --> H + e + H2	
581	H- + O3 --> H + e + O3	
582	H- + ArH+ --> H2 + Ar	
583	H2 + O --> OH + H	
584	H2 + O+ --> OH+ + H	
585	H2 + O- --> H2O + e	
586	H2 + O- --> OH- + H	
587	H2 + O2- --> H- + HO2	
588	H2 + N(2d) --> NH + H	
589	H2 + NO2+ --> NO+ + H2O	
590	H2 + OH --> H2O + H	
591	H2 + OH- --> H2O + H-	
592	H2 + H2O+ --> H3O+ + H	
593	H2 + H3O+ --> H2O + H3+	
594	H2 + ArH+ --> H3+ + Ar	
595	H2(v) + N2 --> H2 + N2	
596	H2(v) + O2 --> H2 + O2	
597	H2(v) + Ar --> H2 + Ar	
598	H2(r) + N2 --> H2 + N2	
599	H2(r) + O2 --> H2 + O2	
600	H2(r) + Ar --> H2 + Ar	
601	H2(ex) + N2 --> H2 + N2	
602	H2(ex) + O2 --> H2 + O2	
603	H2(ex) + Ar --> H2 + Ar	
604	H2+ + O2 --> H2 + O2+	
605	H2+ + H2O --> H2 + H2O+	
606	H2+ + H2O --> H + H3O+	
607	H2+ + Ar -->ArH+ + H	
608	H2+ + Ar --> Ar+ + H2	
609	H3+ + O --> H2O+ + H	
610	H3+ + O --> OH+ + H2	
611	H3+ + NO2 --> NO+ + OH + H2	
612	H3+ + OH --> H2O+ + H2	

613	H3+ + H2O --> H3O+ + H2	
614	H3+ + Ar --> ArH+ + H2	
615	OH + O --> H + O2	
616	OH + O+ --> OH+ + O	
617	OH + O2- --> OH- + O2	
618	OH + O3 --> HO2 + O2	
619	OH + N --> H + NO	
620	OH + N2(ac) --> OH(ac) + N2	
621	OH + N2(aa) --> OH(ac) + N2	
622	OH + N2+ --> OH+ + N2	
623	OH + NO + Ar --> HNO2 + Ar	
624	OH + NO + N2 --> HNO2 + N2	
625	OH + NO + O2 --> HNO2 + O2	
626	OH + NO2 + Ar --> HNO3 + Ar	
627	OH + NO2 + N2 --> HNO3 + N2	
628	OH + NO2 + O2 --> HNO3 + O2	
629	OH + N2O --> HNO + NO	
630	OH + N2O --> HO2 + N2	
631	OH + NO3 --> HO2 + NO2	
632	OH + OH --> H2O + O	
633	OH + OH + Ar --> H2O2 + Ar	
634	OH + OH + N2 --> H2O2 + N2	
635	OH + OH + O2 --> H2O2 + O2	
636	OH + HO2 --> H2O + O2	
637	OH + H2O2 --> H2O + HO2	
638	OH + NH --> N + H2O	
639	OH + NH --> H2 + NO	
640	OH + NH --> H + HNO	
641	OH + HNO --> H2O + NO	
642	OH + HNO2 --> H2O + NO2	
643	OH + HNO3 --> H2O + NO3	
644	OH + HNO4 --> H2O2 + NO3	
645	OH + HNO4 --> H2O + NO2 + O2	
646	OH(ac) + H2O2 --> HO2 + H2O	
647	OH(ac) + O2 --> O2 + OH	
648	OH(ac) + N2 --> N2 + OH	
649	OH(ac) + H2O --> H2O + OH	
650	OH+ + O --> O2+ + H	
651	OH+ + O- + M --> OH + O + M	
652	OH+ + O- + M --> HO2 + M	
653	OH+ + O2 --> OH + O2+	
654	OH+ + N --> NO+ + H	
655	OH+ + NO2- + M --> HNO3 + M	
656	OH+ + NO3- + M --> HNO4 + M	
657	OH+ + OH- + M --> H2O2 + M	
658	OH+ + H2O --> H2O+ + OH	
659	OH+ + H2O --> H3O+ + O	
660	OH- + O --> HO2 + e	

661	O+ + OH- + M --> HO2 + M	
662	OH- + O2+ --> OH + O2	
663	O2+ + OH- + M --> OH + O2 + M	
664	OH- + O3 --> O2- + HO2	
665	OH- + N --> HNO + e	
666	NO+ + OH- + M --> OH + NO + M	
667	NO+ + OH- + M --> HNO2 + M	
668	OH- + NO2 --> NO2- + OH	
669	NO2+ + OH- + M --> OH + NO2 + M	
670	NO2+ + OH- + M --> HNO3 + M	
671	H2O+ + OH- + M --> OH + H2O + M	
672	HO2 + O --> OH + O2	
673	HO2 + O2(a) --> OH + O2 + O	
674	HO2 + O3 --> OH + O2 + O2	
675	HO2 + N --> OH + NO	
676	HO2 + N --> NH + O2	
677	HO2 + NO --> HNO + O2	
678	HO2 + NO + Ar --> HNO3 + Ar	
679	HO2 + NO + N2 --> HNO3 + N2	
680	HO2 + NO2 + N2 --> HNO2 + O2 + N2	
681	HO2 + NO2 + O2 --> HNO2 + O2 + O2	
682	HO2 + NO2 + Ar --> HNO4 + Ar	
683	HO2 + NO2 + N2 --> HNO4 + N2	
684	HO2 + NO2 + O2 --> HNO4 + O2	
685	H2O + O(1d) --> H2 + O2	
686	H2O + O+ --> H2O+ + O	
687	H2O + O- --> H2O2 + e	
688	H2O + O2- --> H2O + O2 + e	
689	H2O + N(2d) --> OH + NH	
690	H2O + N+ --> H2O+ + N	
691	H2O + N+ --> NO+ + H2	
692	H2O + N2+ --> N2 + H2O+	
693	H2O + N4+ --> N2 + N2 + H2O+	
694	H2O + N2O3 --> HNO2 + HNO2	
695	H2O + N2O5 --> HNO3 + HNO3	
696	H2O + H2O+ -->H3O+ + OH	
697	H2O + ArH+ --> H3O+ + Ar	
698	H2O(v) + N2 --> H2O + N2	
699	H2O(v) + O2 --> H2O + O2	
700	H2O(v) + Ar --> H2O + Ar	
701	H2O+ + O- + M --> O + H2O + M	
702	H2O+ + O- + M --> H2O2 + M	
703	H2O+ + O2 --> H2O + O2+	
704	H2O+ + O2- + M --> H2O + O2 + M	
705	H2O+ + O3- --> H2O + O3	
706	H2O+ + O3- + M --> H2O + O3 + M	
707	H2O+ + N --> NO+ + H2	
708	H2O+ + NO2 --> NO2+ + H2O	

709	H2O+ + NO2- + M --> H2O + NO2 + M	
710	H2O+ + NO3- + M --> H2O + NO3 + M	
711	H3O+ + O- --> H2O + H + O	
712	H3O+ + O2- --> H2O + H + O2	
713	H3O+ + O2- --> H2O + H + O + O	
714	H3O+ + NO --> H2O + H + NO+	
715	H2O2 + O --> HO2 + OH	
716	H2O2 + O --> H2O + O2	
717	H2O2 + N2(aa) --> OH + OH + N2	
718	H2O2 + NO3 --> HO2 + HNO3	
719	NH + O --> H + NO	
720	NH + O --> OH + N	
721	NH + O2 --> HNO + O	
722	NH + O2+ --> H + NO2+	
723	NH + N --> H + N2	
724	NH + NO --> H + N2O	
725	NH + NO --> H + N2 + O	
726	NH + NH --> H + N2 + H	
727	HNO + O --> OH + NO	
728	HNO + O --> O2 + NH	
729	HNO + O2 --> HO2 + NO	
730	HNO + N --> NH + NO	
731	HNO2 + O --> OH + NO2	
732	HNO2 + NO3 --> HNO3 + NO2	
733	HNO3 + O --> OH + NO3	
734	HNO3 + O- --> HNO4 + e	
735	HNO3 + O- --> HNO2 + O2-	
736	HNO3 + O2- --> NO3- + HO2	
737	HNO3 + NO2- --> NO3- + HNO2	
738	HNO4 + O --> HO2 + NO3	
739	HNO4 + M --> HO2 + NO2 + M	
740	ArH+ + O- --> Ar + O + H	
741	ArH+ + O- + M --> Ar + O + H + M	
742	ArH+ + O- + M --> Ar + O + H + M	
743	ArH+ + O2- --> Ar + O2 + H	
744	ArH+ + O2- --> Ar + O + O + H	
745	ArH+ + O2- + M --> Ar + O2 + H + M	
746	ArH+ + O3- + M --> Ar + O3 + H + M	
747	ArH+ + NO2- + M --> Ar + NO2 + H + M	
748	ArH+ + NO3- + M --> Ar + NO3 + H + M	
	Radiation	
749	Ar(4p) --> Ar(3p2)	
750	Ar(4p) --> Ar(3p1)	
751	Ar(4p) --> Ar(3p0)	
752	Ar(4p) --> Ar(1p1)	
753	Ar(3p1) --> Ar	
754	Ar(1p1) --> Ar	
755	Ar2(ex) --> Ar	

756	OH(ac) --> OH	
757	H2NO2+ + e --> H2O + NO	
758	H4NO3+ + e --> 2H2O + NO	
759	H6NO4+ + e --> 3H2O + NO	
760	NO+ + H2O --> H2NO2+	
761	H2NO2+ --> NO+ + H2O	
762	H2NO2+ + H2O --> H4NO3+	
763	H2NO2+ + O --> NO2+ + H2O	
764	H2NO2+ + OH --> NO2 + H3O+	
765	H4NO3+ --> H2O + H2NO2+	
766	H4NO3+ + H2O --> H6NO4+	
767	H6NO4+ --> H2O + H4NO3+	
768	H6NO4+ + H2O --> H7O3+ + HNO2	
769	H2NO2+ + O- + M --> NO2 + H2O + M	
770	H2NO2+ + O2- + M --> NO3 + H2O + M	
771	H2NO2+ + NO3- + M --> NO2 + NO2 + H2O +	
772	H2NO2+ + H- + M --> HNO + H2O + M	
773	H2NO2+ + OH- + M --> HNO2 + H2O + M	
774	H4NO3+ + O- + M --> NO2 + 2H2O + M	
775	H4NO3+ + H- + M --> HNO + 2H2O + M	
776	H4NO3+ + OH- + M --> HNO2 + 2H2O + M	
777	H6NO4+ + O- + M --> NO2 + 3H2O + M	
778	H6NO4+ + H- + M --> HNO + 3H2O + M	
	Water cluster ion collisions	
779	H4O2+ + e --> H2O + H + OH	
780	H2O3+ + e --> O2 + H + OH	
781	H5O2+ + e --> H2O + H + H + OH	
782	H7O3+ + e --> 2H2O + H + H + OH	
783	H9O4+ + e --> 3H2O + H + H + OH	
784	H11O5+ + e --> 4H2O + H + H + OH	
785	H15O7+ + e --> 6H2O + H + H + OH	
786	O2+ + H2O --> H2O3+	
787	H2O3+ --> O2+ + H2O	
788	H2O3+ + H2O --> H3O+ + OH + O2	
789	H2O3+ + H2O --> H4O2+ + O2	
790	H2O3+ + NO --> NO+ + H2O + O2	
791	H4O2+ + H2O --> H5O2+ + OH	
792	H3O+ + H2O --> H5O2+	
793	H5O2+ --> H3O+ + H2O	
794	H5O2+ + H2O --> H7O3	
795	H7O3+ --> H5O2+ + H2O	
796	H7O3+ + H2O --> H9O4+	
797	H9O4+ --> H7O3+ + H2O	
798	H9O4+ + H2O --> H11O5+	
799	H11O5+ --> H9O4+ + H2O	
800	H11O5+ + H2O --> H13O6+	
801	H13O6+ --> H11O5+ + H2O	
802	H13O6+ + H2O --> H15O7+	

803	H15O7+ --> H13O6+ + H2O	
804	H2O3+ + O- + M --> O2 + O + H2O + M	
805	H4O2+ + O- + M --> O + 2H2O + M	
806	H4O2+ + O2- + M --> O2 + 2H2O + M	
807	H4O2+ + O3- + M --> O3 + 2H2O + M	
808	H4O2+ + NO2- + M --> NO2 + 2H2O + M	
809	H4O2+ + NO3- + M --> NO3 + 2H2O + M	
810	H5O2+ + O- + M --> O + H + 2H2O + M	
811	H5O2+ + O2- --> H + 2H2O + O2	
812	H5O2+ + O2- --> H + 2H2O + O + O	
813	H5O2+ + O2- + M --> O2 + H + 2H2O + M	
814	H5O2+ + O3- --> H + 2H2O + O3	
815	H5O2+ + O3- + M --> O3 + H + 2H2O + M	
816	H5O2+ + NO2- + M --> NO2 + H + 2H2O + M	
817	H5O2+ + NO3- --> H + 2H2O + NO3	
818	H5O2+ + NO3- + M --> NO3 + H + 2H2O + M	
819	H5O2+ + OH- --> H + 2H2O + O + H	
820	H5O2+ + OH- + M --> OH + H + 2H2O + M	
821	H7O3+ + O- + M --> O + H + 3H2O + M	
822	H7O3+ + O2- + M --> O2 + H + 3H2O + M	
823	H7O3+ + O3- + M --> O3 + H + 3H2O + M	
824	H7O3+ + NO2- + M --> NO2 + H + 3H2O + M	
825	H7O3+ + NO3- + M --> NO3 + H + 3H2O + M	
826	H7O3+ + OH- + M --> OH + H + 3H2O + M	
827	H9O4+ + O- + M --> O + H + 4H2O + M	
828	H9O4+ + O2- + M --> O2 + H + 4H2O + M	
829	H9O4+ + O3- + M --> O3 + H + 4H2O + M	
830	H9O4+ + NO2- + M --> NO2 + H + 4H2O + M	
831	H9O4+ + NO3- + M --> NO3 + H + 4H2O + M	
832	H9O4+ + OH- + M --> OH + H + 4H2O + M	
833	H11O5+ + O- + M --> O + H + 5H2O + M	
834	H11O5+ + O2- + M --> O2 + H + 5H2O + M	
835	H11O5+ + O3- + M --> O3 + H + 5H2O + M	
836	H11O5+ + NO2- + M --> NO2 + H + 5H2O + M	
837	H11O5+ + NO3- + M --> NO3 + H + 5H2O + M	
838	H11O5+ + OH- + M --> OH + H + 5H2O + M	
839	H13O6+ + O3- + M --> O3 + H + 6H2O + M	
840	H13O6+ + NO2- +M --> NO2 + H + 6H2O + M	
841	H13O6+ + NO3- + M --> NO3 + H + 6H2O + M	
842	H13O6+ + OH- + M --> OH + H + 6H2O + M	
843	H15O7+ + O3- + M --> O3 + H + 7H2O + M	
844	H15O7+ + NO2- +M --> NO2 + H + 7H2O + M	
845	H15O7+ + NO3- + M --> NO3 + H + 7H2O + M	
846	H15O7+ + OH- + M --> OH + H + 7H2O + M	

Species containing carbon—created out of atmospheric CO2—are not taken into account. Several electronically, rotationally and vibrationally excited states are included

in the model. Electronically excited states are important to consider because they often play a crucial role in the plasma chemistry, for example in stepwise electron-impact or Penning ionization. Note that, at atmospheric pressure, due to a high collision frequency, it is unlikely that high electronic energy levels become populated and therefore these are not included. Rotational and vibrational excitations, on the other hand, are important processes since electrons lose energy in this way. As a consequence, this influences the average electron temperature significantly. In the reaction set, rotationally and vibrationally excited states only participate in electron-impact excitation and de-excitation reactions, as well as in physical quenching by the background gas. The reason is that the rotational and vibrational energy is usually too low to induce a fast chemical change in its collision partner. Three factors for the selection of excited states in the model are considered: metastability, high cross sections and low energy threshold for excitation from the ground state, or states that have been reported to be important in this type of plasmas. For example, for the hydrogen molecules, the magnitude of the vibrational excitation cross sections roughly drops with one order of magnitude for each next vibrational quantum number. Therefore, although the excitations to more energetic states still show a threshold value within the typical electron energy range of the simulations, these collisions are not included. The possibility of positive water ion clustering is included in the reaction set. Negative ion clustering is not included in the model [30].

REFERENCES

[1] M. A. Lieberman, A. J. Lichtenberg, *Principles of plasma discharges and materials processing*, 2nd ed. Hoboken, N.J.: Wiley-Interscience, 2005.
[2] http://www.balticnet-plasmatec.org.
[3] J. Winter, R. Brandenburg, K. D. Weltmann, "*Atmospheric pressure plasma jets: An overview of devices and new directions*", *Plasma Sources Science and Technology*, 2015, *24*, 064001.
[4] X. Lu, M. Laroussi, V. Puech, "*On atmospheric-pressure non-equilibrium plasma jets and plasma bullets*", *Plasma Sources Science and Technology*, 2012, *21*, 034005.
[5] M. Teschke, J. Kedzierski, E. G. Finantu-Dinu, D. Korzec, J. Engemann, "*High-speed photographs of a dielectric barrier atmospheric pressure plasma jet*", *IEEE Transactions on Plasma Science*, 2005, *33*, 310.
[6] Q. Li, J.-T. Li, W.-C. Zhu, X.-M. Zhu, Y.-K. Pu, "*Effects of gas flow rate on the length of atmospheric pressure nonequilibrium plasma jets*", *Applied Physics Letters*, 2009, *95*, 141502.
[7] X. Lu, Z. Jiang, Q. Xiong, Z. Tang, X. Hu, Y. Pan, "*An 11cm long atmospheric pressure cold plasma plume for applications of plasma medicine*", *Applied Physics Letters*, 2008, *92*, 081502.
[8] J. L. Walsh, M. G. Kong, "*Contrasting characteristics of linear-field and cross-field atmospheric plasma jets*", *Applied Physics Letters*, 2008, *93*, 111501.
[9] X. Lu, Z. Jiang, Q. Xiong, Z. Tang, Y. Pan, "*A single electrode room-temperature plasma jet device for biomedical applications*", *Applied Physics Letters*, 2008, *92*, 151504.
[10] M. Laroussi, X. Lu, "*Room-temperature atmospheric pressure plasma plume for biomedical applications*", *Applied Physics Letters*, 2005, *87*, 113902.
[11] V. Léveillé, S. Coulombe, "*Design and preliminary characterization of a miniature pulsed RF APGD torch with downstream injection of the source of reactive species*", *Plasma Sources Science and Technology*, 2005, *14*, 467.
[12] A. Shashurin, M. N. Shneider, A. Dogariu, R. B. Miles, M. Keidar, "*Temporal behavior of cold atmospheric plasma jet*", *Applied Physics Letters*, 2009, *94*, 231504.
[13] S. E. Babayan, J. Y. Jeong, V. J. Tu, J. Park, G. S. Selwyn, R. F. Hicks, "*Deposition of silicon dioxide films with an atmospheric-pressure plasma jet*", *Plasma Sources Science and Technology*, 1998, *7*, 286.
[14] E. Stoffels, I. E. Kieft, R. E. J. Sladek, "*Superficial treatment of mammalian cells using plasma needle*", *Journal of Physics D: Applied Physics*, 2003, *36*, 2908.
[15] X. Lu, Y. Cao, P. Yang, Q. Xiong, Z. Xiong, Y. Xian, Y. Pan, "*An RC plasma device for sterilization of root canal of teeth*", *IEEE Transactions on Plasma Science*, 2009, *37*, 668.
[16] Y. C. Hong, H. S. Uhm, "*Microplasma jet at atmospheric pressure*", *Applied Physics Letters*, 2006, *89*, 221504.
[17] T. L. Ni, F. Ding, X. D. Zhu, X. H. Wen, H. Y. Zhou, "*Cold microplasma plume produced by a compact and flexible generator at atmospheric pressure*", *Applied Physics Letters*, 2008, *92*, 241503.
[18] A.-A. H. Mohamed, F. J. Kolb, H. K. Schoenbach, "*Low temperature, atmospheric pressure, direct current microplasma jet operated in air, nitrogen and oxygen*", *The European Physical Journal D*, 2010, *60*, 517.
[19] Y. C. Hong, W. S. Kang, Y. B. Hong, W. J. Yi, H. S. Uhm, "*Atmospheric pressure air-plasma jet evolved from microdischarges: Eradication of E. coli with the jet*", *Physics of Plasmas*, 2009, *16*, 123502.
[20] G. Fridman, M. Peddinghaus, M. Balasubramanian, H. Ayan, A. Fridman, A. Gutsol, A. Brooks, "*Blood Coagulation and Living Tissue Sterilization by Floating-Electrode Dielectric Barrier Discharge in Air*", *Plasma Chemistry and Plasma Processing*, 2006, *26*, 425.
[21] S. Wu, X. Lu, Z. Xiong, Y. Pan, "*A touchable pulsed air plasma plume driven by DC power supply*", *IEEE Transactions on Plasma Science*, 2010, *38*, 3404.
[22] X. Lu, Z. Xiong, F. Zhao, Y. Xian, Q. Xiong, W. Gong, C. Zou, Z. Jiang, Y. Pan, "*A simple atmospheric pressure room-temperature air plasma needle device for biomedical applications*", *Applied Physics Letters*, 2009, *95*, 181501.
[23] W. V. Gaens, S. Iseni, A. Schmidt-Bleker, K. D. Weltmann, S. Reuter, A. Bogaerts, "*Numerical analysis of the effect of nitrogen and oxygen admixtures on the chemistry of an argon plasma jet operating at atmospheric pressure*", *New Journal of Physics*, 2015, *17*, 033003.
[24] A. F. H. Van Gessel, K. M. J. Alards, P. J. Bruggeman, "*NO production in an RF plasma jet at atmospheric pressure*", *Journal of Physics D: Applied Physics*, 2013, *46*, 265202.
[25] E. R. Ionita, M. D. Ionita, E. C. Stancu, M. Teodorescu, G. Dinescu, "*Small size plasma tools for material processing at atmospheric pressure*", *Applied Surface Science*, 2009, *255*, 5448.
[26] B. Niermann, T. Hemke, N. Y. Babaeva, M. Böke, M. J. Kushner, T. Mussenbrock, J. Winter, "*Spatial dynamics of helium metastables in sheath or bulk dominated rf micro-plasma jets*", *Journal of Physics D: Applied Physics*, 2011, *44*, 485204.

[27] D. Ellerweg, A. Von Keudell, J. Benedikt, "*Unexpected O and O 3 production in the effluent of He/O 2 microplasma jets emanating into ambient air*", *Plasma Sources Science and Technology*, 2012, *21*, 034019.
[28] D. X. Liu, P. Bruggeman, F. Iza, M. Z. Rong, M. G. Kong, "*Global model of low-temperature atmospheric-pressure He + H2O plasmas*", *Plasma Sources Science and Technology*, 2010, *19*, 025018.
[29] K. Niemi, J. Waskoenig, N. Sadeghi, T. Gans, D. O'Connell, "*The role of helium metastable states in radio-frequency driven helium-oxygen atmospheric pressure plasma jets: Measurement and numerical simulation*", *Plasma Sources Science and Technology*, 2011, *20*, 055005.
[30] W. Van Gaens, A. Bogaerts, "*Erratum: Kinetic modelling for an atmospheric pressure argon plasma jet in humid air (J. Phys. D: Appl. Phys. 46 (2013) 275201))*", *Journal of Physics D: Applied Physics*, 2014, *47*, 079502.
[31] J. Waskoenig, K. Niemi, N. Knake, L. M. Graham, S. Reuter, V. S.-v. d. Gathen, T. Gans, "*Atomic oxygen formation in a radio-frequency driven micro-atmospheric pressure plasma jet*", *Plasma Sources Science and Technology*, 2010, *19*, 045018.
[32] M. J. Kushner, "*Modeling of microdischarge devices: Pyramidal structures*", *Journal of Applied Physics*, 2004, *95*, 846.
[33] R. Dorai, M. J. Kushner, "*A model for plasma modification of polypropylene using atmospheric pressure discharges*", *Journal of Physics D: Applied Physics*, 2003, *36*, 666.
[34] www.plasma-r.com.
[35] S. Hofmann, A. F. H. Van Gessel, T. Verreycken, P. Bruggeman, "*Power dissipation, gas temperatures and electron densities of cold atmospheric pressure helium and argon RF plasma jets*", *Plasma Sources Science and Technology*, 2011, *20*, 065010.
[36] http://www.bolsig.laplace.univ-tlse.fr.
[37] C. Lee, M. A. Lieberman, "*Global model of Ar, O2, Cl2, and Ar/O2 high-density plasma discharges*", *Journal of Vacuum Science & Technology A*, 1995, *13*, 368.
[38] G. Kokkoris, A. Goodyear, M. Cooke, E. Gogolides, "*A global model for C4F8 plasmas coupling gas phase and wall surface reaction kinetics*", *Journal of Physics D: Applied Physics*, 2008, *41*, 195211.
[39] G. Kokkoris, A. Panagiotopoulos, A. Goodyear, M. Cooke, E. Gogolides, "*A global model for SF6 plasmas coupling reaction kinetics in the gas phase and on the surface of the reactor walls*", *Journal of Physics D: Applied Physics*, 2009, *42*, 055209.
[40] N. Škoro, N. Puač, S. Lazović, U. Cvelbar, G. Kokkoris, E. Gogolides, "*Characterization and global modelling of low-pressure hydrogen-based RF plasmas suitable for surface cleaning processes*", *Journal of Physics D: Applied Physics*, 2013, *46*, 475206.
[41] W. V. Gaens, A. Bogaerts, "*Reaction pathways of biomedically active species in an Ar plasma jet*", *Plasma Sources Science and Technology*, 2014, *23*, 035015.
[42] A. C. Hindmarsh, "*ODEPACK, a systematized collection of ODE solvers*", *Scientific computing: IMACS transactions on scientific computation*, 1983, *1*, 55.
[43] J. C. Butcher, *Numerical methods for ordinary differential equations*. Chichester, U.K. ; New York: John Wiley & Sons, 2003.
[44] E. Hairer, S. P. Nørsett, G. Wanner, R. L. Graham, J. Stoer, R. Varga, *Solving ordinary differential equations I Nonstiff problems*, 2nd revised edition. ed. Berlin ; New York: Springer-Verlag, 1993.
[45] K. E. Atkinson, *An introduction to numerical analysis*, 2nd ed. New York: Wiley, 1989.
[46] W. H. Press, *Numerical recipes : the art of scientific computing*. New York: Cambridge University Press, 2007.
[47] E. Süli, D. F. Mayers, *An introduction to numerical analysis*. Cambridge ; New York: Cambridge University Press, 2003.
[48] M. Abramowitz, I. A. Stegun, *Handbook of mathematical functions, with formulas, graphs, and mathematical tables*. New York,: Dover Publications, 1965.
[49] W. H. Press, W. T. Vetterling, *Numerical recipes in C : the art of scientific computing*, 2nd ed ed. Cambridge: Cambridge University Press, 1992.
[50] A. Quarteroni, R. Sacco, F. Saleri, P. Gervasio, SpringerLink (Online service). *Matematica Numerica (4a edizione. ed.)*. Available: http://dx.doi.org/10.1007/978-88-470-5644-2
[51] U. M. Ascher, L. R. Petzold, *Computer methods for ordinary differential equations and differential-algebraic equations*. Philadelphia: Society for Industrial and Applied Mathematics, 1998.
[52] J. D. Lambert, *Numerical methods for ordinary differential systems : The initial value problem*: John Wiley and Sons, 1991.
[53] www.wikipedia.com.
[54] G. G. Dahlquist, "*A special stability problem for linear multistep methods*", *BIT*, 1963, *3*, 27.
[55] A. Iserles, *A first course in the numerical analysis of differential equations*. Cambridge ; New York: Cambridge University Press, 1996.
[56] L. Petzold, "*Automatic Selection of Methods for Solving Stiff and Nonstiff Systems of Ordinary Differential Equations*", *SIAM Journal on Scientific and Statistical Computing*, 1983, *4*, 136.

[57] R. Schiestel, Wiley InterScience (Online service). (2008). *Modeling and simulation of turbulent flows*. Available: http://dx.doi.org/10.1002/9780470610848 Wiley MIT Access Only
[58] M. Schobeiri, SpringerLink (Online service). (2010). *Fluid mechanics for engineers a graduate textbook*. Available: SpringerLink http://dx.doi.org/10.1007/978-3-642-11594-3 MIT Access Only
[59] www.comsol.com.
[60] F. P. Incropera, D. P. DeWitt, *Fundamentals of heat and mass transfer*, 3rd ed. New York: Wiley, 1990.
[61] J. P. Holman, *Heat transfer*, 9th ed. New York: McGraw-Hill, 2002.
[62] G. N. Abramovich, *The theory of turbulent jets*. Cambridge, Mass.,: M.I.T. Press, 1963.
[63] A. Abdel-Rahman, "*A review of effects of initial and boundary conditions on turbulent*", *WSEAS Transactions on Fluid Mechanics*, 2010, *5*, 257.
[64] http://www.compassis.com.
[65] https://web.stanford.edu.
[66] https://uiuc-cse.github.io.
[67] www.bakker.org.
[68] www.fluentusers.com.
[69] S. B. Pope, *Turbulent flows*. Cambridge: Cambridge University Press, 2000.
[70] S. Zhang, W. Van Gaens, B. Van Gessel, S. Hofmann, E. Van Veldhuizen, A. Bogaerts, P. Bruggeman, "*Spatially resolved ozone densities and gas temperatures in a time modulated RF driven atmospheric pressure plasma jet: An analysis of the production and destruction mechanisms*", *Journal of Physics D: Applied Physics*, 2013, *46*, 205202.
[71] http://www.cfd-online.com.
[72] R. B. Bird, W. E. Stewart, E. N. Lightfoot, *Transport phenomena*, 2nd ed. New York: J. Wiley, 2002.
[73] nessie.imel.demokritos.gr.
[74] E. Hairer, G. Wanner, *Solving ordinary differential equations. II, Stiff and differential-algebraic problems*, 2nd rev. ed. Berlin ; London: Springer-Verlag, 1996.
[75] K. A. Berrington, P. G. Burke, W. D. Robb, "*The scattering of electrons by atomic nitrogen*", *Journal of Physics B: Atomic and Molecular Physics*, 1975, *8*, 2500.
[76] J. Bacri, A. Medani, "*Electron diatomic molecule weighted total cross section calculation. III. Main inelastic processes for N2 and N+ 2*", *Physica B+C*, 1982, *112*, 101.
[77] P. Teulet, J. P. Sarrette, A. M. Gomes, "*Calculation of electron impact inelastic cross sections and rate coefficients for diatomic molecules. Application to air molecules*", *Journal of Quantitative Spectroscopy and Radiative Transfer*, 1999, *62*, 549.
[78] S. Dupljanin, J. d. Urquijo, O. Šašić, E. Basurto, A. M. Juárez, J. L. Hernández-Ávila, S. Dujko, Z. L. Petrović, "*Transport coefficients and cross sections for electrons in N 2 O and N 2 O/N 2 mixtures*", *Plasma Sources Science and Technology*, 2010, *19*, 025005.
[79] R. K. Janev, D. Reiter, U. Samm, "*Collision processes in low-temperature hydrogen plasmas*", *INIS*, 2003, *35*, 35040310.